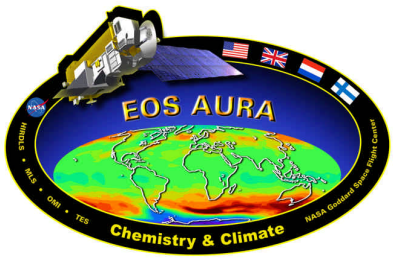

OMI Algorithm Theoretical Basis Document

Volume III

Clouds, Aerosols, and Surface UV Irradiance

P. Stammes (Editor)
R. Noordhoek (Layout)

ATBD-OMI-03, Version 2.0, August 2002

Table of Contents

Preface

Background

The Ozone Monitoring Instrument OMI is a Dutch-Finnish ozone monitoring instrument that will fly on NASA's Aura Mission, part of the Earth Observation System (EOS), scheduled for launch in January 2004. OMI's measurements of ozone columns and profiles, aerosols, clouds, surface UV irradiance, and the trace gases NO_2, SO_2, HCHO, BrO, and OClO fit well into Aura's mission goals to study the Earth's atmosphere. OMI is a wide swath, nadir viewing, near-UV and visible spectrograph which draws heavily on European experience in atmospheric research instruments such as GOME (on ERS-2), SCIAMACHY and GOMOS (both flying on Envisat).

Purpose

The four OMI-EOS Algorithm Theoretical Basis Documents (ATBDs) present a detailed picture of the instrument and the retrieval algorithms used to derive atmospheric information from the instrument's measurements. They will provide a clear understanding of the data-products to the OMI scientists, to the Aura Science Team, and the atmospheric community at large. Each chapter of the four ATBDs is written by the scientists responsible for the development of the algorithms presented.

These ATBDs were presented to a group of expert reviewers recruited mainly from the atmospheric research community outside of Aura. The results of the reviewer's study, critiques and recommendations were presented at the ATBD panel review on February 8th, 2002. Overall, the review was successful. All ATBDs, except the Level 1b ATBD, have been modified based on the recommendations of the written reviews and the panel, which were very helpful in the development of these documents. An updated level 1b ATBD is expected in the near future.

Contents

ATBD 1 contains a general description of the instrument and its measurement modes. In addition, there is a presentation of the Level 0 to 1B algorithms that convert instrument counts to calibrated radiances, ground and in-flight calibration, and the flight operations needed to collect science data. It is critical that this is well understood by the developers of the higher level processing, as they must know exactly what has been accounted for (and how), and what has not been considered in the Level 0 to 1B processing.

ATBD 2 covers several ozone products, which includes total ozone, profile ozone, and tropospheric ozone. The capability to observe a continuous spectrum makes it possible to use a DOAS (Differential Optical Absorption Spectroscopy) technique developed in connection with GOME, flying on ERS-2 to derive total column ozone. At the same time, an improved version of the TOMS total ozone column algorithm, developed and used successfully over 3 decades, will be used on OMI data. Completing the group of four algorithms in this ATBD is a separate, independent estimate of tropospheric column ozone, using an improved version of the Tropospheric Ozone Residual (TOR) and cloud slicing methods developed for TOMS. Following the recommendation of the review team, a chapter has been added which lays out the way ahead towards combining the individual ozone algorithms into fewer, and ultimately a single ozone "super" algorithm.

ATBD 3 presents retrieval algorithms for producing the aerosols, clouds, and surface UV radiation products. Retrieval of aerosol optical thickness and aerosol type is presented. Aerosols are of interest because they play an important role in tropospheric pollution and climate change. The cloud products include cloud top height and effective cloud fraction, both of which are essential, for example, in retrieving the trace gas vertical columns accurately. Effective cloud fraction is obtained by comparing measured reflectance with the expected reflectance from a cloudless pixel and reflectance from a fully cloudy pixel with a Lambertian albedo of 0.8. Two complementary algorithms are presented for cloud-top height (or pressure). One uses a DOAS method, applied to the O_2–O_2 absorption band around 477 nm, while the other uses the filling-in of selected Fraunhofer lines in the range 352-398 nm due to rotational Raman scattering. Surface UV irradiance is important because of its damaging effects on human health, and on terrestrial and aquatic ecosystems. OMI will extend the long, continuous record produced by TOMS, using a refined algorithm based on the TOMS original.

ATBD 4 presents the retrieval algorithms for the "additional" trace gases that OMI will be able to monitor: NO_2, SO_2, HCHO, BrO, and OClO. These gases are of interest because of their respective roles in stratospheric and tropospheric chemistry. Extensive experience with GOME has produced spectral fitting techniques used in these newly developed retrieval algorithms, each adapted to the specific characteristics of OMI and the particular molecule in question.

Summary

The four OMI-EOS ATBDs present in detail how each of OMI's data products are produced. The data products described in the ATBD will make significant steps toward meeting the objectives of the NASA's Earth Science Enterprise. OMI data products will make important contributions in addressing Aura's scientific questions and will strengthen and compliment the atmospheric data products by the TES, MLS and HIRDLS instruments.

P.F. Levelt (KNMI, The Netherlands)	*Principal Investigato*r
G.H.J. van den Oord (KNMI, The Netherlands)	*Deputy PI*
E. Hilsenrath (NASA/GSFC, USA)	*Co-PI*
G.W Leppelmeier (FMI, Finland)	*Co-PI*
P.K. Bhartia (NASA/GSFC, USA)	*US ST Leader*

1. Introduction and algorithm overview

P. Stammes
Royal Netherlands Meteorological Institute (KNMI), De Bilt, The Netherlands

In this volume the retrieval algorithms for the OMI products on clouds, aerosols, and surface UV irradiance are described. These are three different topics, but all related to the Earth's radiation balance. Furthermore, there are several interrelationships between the three products through scattering of sunlight in the troposphere, which are discussed below.

We first give a brief introduction regarding the need and usefulness of these products, and next give an overview of the planned retrieval algorithms. More introductory information can be found in the individual chapters, where the algorithms are described in detail.

1.1. Introduction

The OMI products of this volume relate directly or indirectly to the mission objectives of EOS-Aura: ozone layer monitoring, air quality monitoring, and monitoring of constituents that affect Earth's climate. At longer parts of the UV spectrum (UVA: 320-400 nm) the surface UV irradiance is mainly determined by clouds, surface elevation, and the presence of aerosol and snow. However, at shorter UV wavelengths (UVB: 280-320 nm) the surface UV irradiance will increase with stratospheric ozone layer depletion, all other factors remaining unchanged. Anthropogenic aerosols are part of the tropospheric pollution due to industry, traffic, and biomass burning. Naturally occurring aerosols are, for example, desert dust and volcanic aerosols. Small aerosols (CCN) contribute to cloud formation. Clouds and aerosols both affect the Earth's radiation balance, and have to be measured globally.

OMI has been designed to provide daily global coverage of clouds, aerosols, and surface UV irradiance with a spatial resolution of 13×24 km^2 (OMI ATBD Vol. I). Monitoring and process studies of clouds and aerosols are also planned with other satellite instruments that fly in formation with Aura (within about 15 minutes), in the so-called A-Train, namely: the global imager MODIS on EOS-Aqua, the cloud radar on CLOUDSAT, the aerosol/cloud lidar on CALIPSO, and the polarisation and bidirectionality imager POLDER on PARASOL. Important intercomparisons and synergisms will be possible between these co-located measurements and the OMI cloud and aerosol products.

1.1.1. Clouds

The presence of clouds is an important piece of information needed in the OMI trace gas and aerosol retrieval algorithms. Clouds strongly change the atmospheric radiation field as compared to the situation of a clear sky, and shield tropospheric species from observation [e.g. *Koelemeijer and Stammes*, 1999]. Therefore, cloud information should be generated as input for OMI level 1-2 processing. This information is needed in the form of two main cloud parameters: effective cloud fraction, which is a combination of the "true" cloud fraction and cloud optical thickness, and cloud pressure (or altitude). In principle, this cloud information may also be obtained from meteorological satellites or MODIS on-board Aqua, with higher spatial resolution than OMI. However, by retrieving cloud information from the OMI reflectance data itself, optimal co-location, on-line availability, and independence from other data sources are achieved. Furthermore, the cloud products from OMI may be more consistent with the other OMI algorithms (see below).

Global cloud information is in itself an important climate parameter. OMI's pixel size (13×24 km^2) and daily global coverage are large improvements with respect to other satellite UV-

visible spectrometers, like GOME (40×320 km^2, 3-day global coverage) and SCIAMACHY (30×60 km^2, 6-day global coverage).

1.1.2. Aerosols

Aerosols are an important but complicated factor in climate and atmospheric chemistry. Aerosols cool the climate system by shortwave scattering, but heat it due to shortwave absorption. They play an important role in air pollution, in chemical reactions among gases, and in reduction of surface UV irradiance. Their indirect climate effects, through, e.g., cloud formation and dissipation, are not yet well understood.

The main problem with detection of aerosols is that they have many different physical properties due to different sources and origins: their refractive indices vary strongly, resulting in transparent to opaque and black particles; their sizes vary from nanometers to microns; and their shapes vary from spherical to irregular. Mixtures of several types also regularly occur.

Detection of aerosols is also needed to improve trace gas retrievals of OMI. For example, for stratospheric ozone retrieval the presence of volcanic aerosols should be known. For retrieval of the amount of tropospheric NO_2 and other minor gases the presence of aerosols is also important, because it influences the air mass factor (photon path length) in the troposphere.

1.1.3. Surface UV irradiance

Surface UV irradiance plays an essential role in damaging living organisms on the Earth and in the ocean. Knowledge of the amount and trend in surface UV irradiance is therefore needed in life sciences, such as biology and medicine. Global increases in surface UV irradiance due to decreases in stratospheric ozone [*Madronich*, 1992, *Herman et al.*, 1996, *WMO99*] are important for users of OMI data, including scientists, the general public, and policymakers.

The surface UV irradiance not only depends on the ozone column, but also on the occurrence of clouds, the presence of aerosols, and the albedo of the surface. The surface UV irradiance from OMI will be calculated on the basis of the actually measured ozone column and UV reflectance from OMI, with external information added.

A long-term record of surface UV irradiance has been established using TOMS data (since 1978). It will be possible, by using the same algorithm for OMI as for TOMS, to extend this record with the mission period of Aura.

1.1.4. Requirements

The scientific requirements for the cloud, aerosol and surface UV products of OMI, as taken from the *Scientific Requirements Document for OMI-EOS* [*Levelt et al.*, 2000], are given in Table 1.1, with the exception of the requirement on the accuracy of the aerosol optical thickness (AOT). After the ATBD review in February 2002, the accuracy requirement for the AOT has been set to 30 % instead of the original value of 10 %, because that value was considered to be too strict. The AOT accuracy requirement aerosol is now 30 % or 0.1 at 400 nm, whichever value is largest. This can be translated into 30 % or 0.08 at 500 nm. All products have the highest (A) priority, which means that they should be available at launch.

1.1.5. OMI capabilities

The OMI instrument has by design several capabilities for cloud and aerosol detection (see *OMI ATBD, Vol. I*, for a detailed description of the instrument). The algorithms will make use of OMI's spectral capabilities, which include its complete spectral coverage of the range 306-500 nm (channels UV-2 and VIS) and its spectral resolution of 0.45-0.63 nm. The nominal signal-to-noise ratio of OMI at the cloud and aerosol retrieval wavelengths is about 1000.

Table 1.1 Scientific requirements for cloud, aerosol, and surface UV products from the OMI SRD [Levelt et al., 2000]. OT: optical thickness. SSA: single scattering albedo. The aerosol optical thickness is taken at 400 nm.

Product	Priority	Accuracy	Pixel size (km^2)	Remarks
Cloud fraction	A	< 0.1	20×20	Needed for other OMI algorithms
Cloud pressure	A	< 100 hPa	20×20	Needed for other OMI algorithms
Aerosol OT	A	< 30 % / 0.1	20×20	
Aerosol SSA	A	< 0.1	20×20	
Surface UV	A	< 4 %	20×20	

The standard OMI pixel size of $13 \times 24\ km^2$ in the global mode is an important improvement for cloud and aerosol retrieval as compared to TOMS ($50 \times 50\ km^2$) and GOME ($40 \times 320\ km^2$). Smaller pixels lead to more cloud free scenes, which is essential for aerosol retrieval. On the basis of ATSR-2 measurements of clouds at $1 \times 1\ km^2$ resolution, *Kerridge et al*. [2001] have shown that the percentage of cloud free pixels for OMI-type pixels is about 17 %, whereas it is about 9 % for TOMS-type pixels and only about 4 % for GOME-type pixels. If a 5 % cloud fraction is still allowed for retrieval, these percentages are 27 %, 21 %, and 18 %, respectively.

Furthermore, OMI has the capability at one wavelength per channel to have a five times higher spatial sampling in the flight direction than normal. This capability is called “small pixel data read-out”. It is expected to be useful to obtain more information on spatial inhomogeneity of the scene - especially of clouds. These small pixel data are included in the level-1B data set. The small pixel data read-out uses the non-co-added, 0.4 s integrated, swath data at one wavelength per channel. The normal sampling, which holds for the entire spectrum of each channel, uses co-added data and yields one swath per 2 s. Because OMI's ground-speed is about 6.5 km/s, the normal pixel size is 13 km in the flight direction. However, for the small pixel data (0.4 s) the pixel size is only about 2.6 km in the flight direction. So, the small pixel data yields 5 swaths with 2.6 km sampling distance in one normal swath of 13 km resolution. Because OMI's instantaneous field-of-view in the flight direction is about 10 km, these 5 swaths partly overlap. In the across-track direction the resolution of the small pixel data is the same as for the normal pixel data, namely 24 km in the global mode and 12 km in the zoom modes. The expected signal-to-noise ratio of the small pixel data is reduced by a factor of $\sqrt{5}$ w.r.t. the nominal value, so about 450.

1.2. Overview of algorithms

1.2.1. Cloud retrieval algorithms

The standard techniques for cloud detection in satellite meteorology make use of visible and thermal infrared (IR) imaging [e.g. *Rossow and Garder*, 1993]. The cloud fraction is determined from the contrast between clouds and the underlying surface. The cloud top pressure is usually derived from the thermal IR brightness temperature of the clouds: high clouds are colder than low clouds. Spectral techniques include the CO_2 slicing method [e.g. *Smith and Platt*, 1978] and the O_2 A-band method [e.g. *Fischer and Grassl*, 1991], which make use of absorption lines of the well-mixed gases CO_2 and O_2.

Since OMI observes only UV-visible radiances up to 500 nm, IR methods cannot be used. Instead, we build on the heritage of cloud detection developed for TOMS, SBUV, and

GOME, and improve these techniques. We will use two different techniques for cloud pressure retrieval, namely O_2-O_2 absorption (Chapter 2) and Raman scattering (Chapter 3). The main cloud parameters retrieved from OMI are the (effective) cloud fraction and the cloud pressure, discussed below.

Cloud model assumptions

The main aim of the OMI cloud product is correction for cloud effects in trace gas and aerosol retrievals. From experience with TOMS and GOME, a simple cloud model, namely a Lambertian reflector at some altitude in the atmosphere, suffices for the correction of cloud effects in ozone retrieval [*McPeters et al*., 1996, and references therein; *Koelemeijer and Stammes*, 1999]. Furthermore, it has been shown by P.K. Bhartia using the TOMS reflectance data [*OMI ATBD, Vol. II, Chapter 1*], that the ratios between the TOA reflectances at 340 and 380 nm for a large set of cloudy pixels can be well explained by assuming a Lambertian reflector with albedo of 0.75-0.80 for the clouds, and with varying cloud fraction between 0 and 1. As an illustration of the spectrally flat behaviour of clouds in the spectral range 300-500 nm, Fig. 1.1 shows a GOME measurement of a clear and a cloudy pixel over ocean, and their ratio, as compared to radiative transfer calculations with a Lambertian reflector at the ground having albedos 0.05 and 0.5.

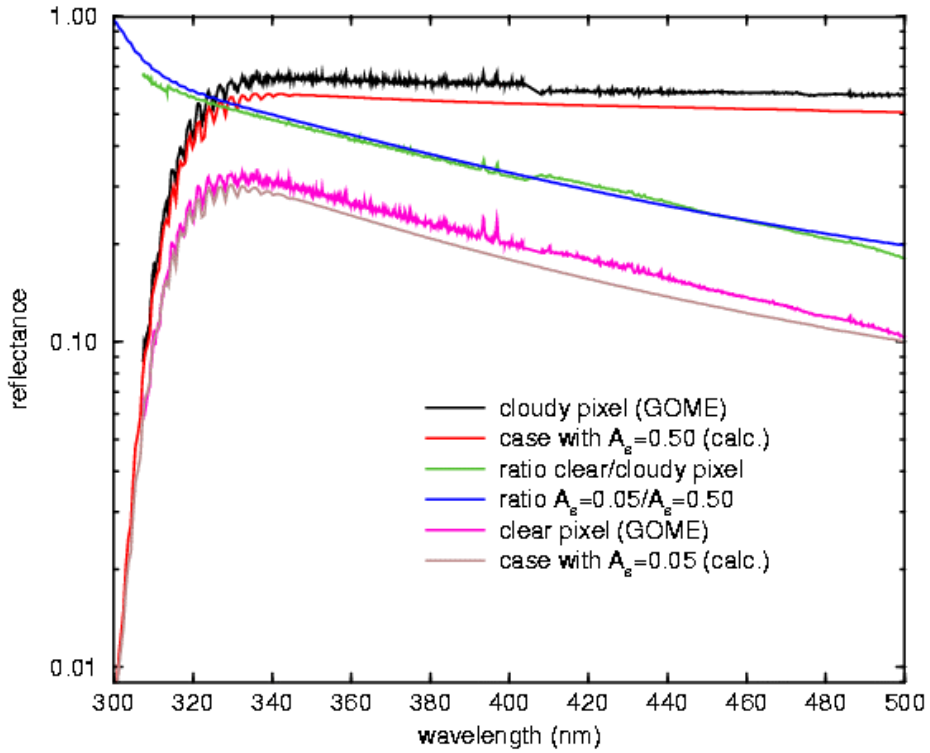

Figure 1.1. Measured and calculated reflectance spectra of a typical cloudy and a clear pixel, and their ratio. The two measured spectra (306-500 nm) are from GOME, orbit 1337 (23 July 1995), over ocean, for nadir view and solar zenith angle 22-25°. The two calculated spectra (300-500 nm) are for a clear atmosphere with Rayleigh scattering and absorption by O_3 and NO_2 (actual column amounts) on top of a Lambertian surface, with albedo 0.5 ("cloudy case") and 0.05 ("clear case").

Please note the logarithmic scale of the reflectance in Fig. 1.1. Apparently, a spectrally gray Lambertian reflector suffices to represent the general shape of realistic cloudy spectra.

Therefore, in the OMI algorithms for e.g. ozone column, ozone profile, and NO_2 column retrieval, clouds are assumed to be Lambertian reflectors with a high albedo (usually 0.8). This means that the cloud retrieval algorithm should also use this cloud model. Of course, the error due to the assumption of this simple cloud model in the retrieval of trace gases and of cloud properties should be evaluated with realistic (water or ice) scattering clouds. But it should be noted that even with the assumption of a Lambertian reflector cloud model, the bi-directional reflectance effect of real clouds is included to first order, because the cloud retrieval is done for the same sun-satellite viewing geometry as holds for the other OMI retrieval algorithms.

Both the O_2-O_2 and Raman algorithms use the independent pixel approximation, which means that the cloudy and clear parts of the pixel can be treated independently. So, in the case of broken clouds, a pixel is assumed to consist of a clear and a cloudy part.

The Lambertian reflector model with high albedo is also called the thick cloud model. It means that all radiance due to clouds in the pixel is assumed to be caused by fractional coverage with a cloud of albedo 0.8. (The cloud optical thickness that belongs to a water droplet cloud with spherical albedo of 0.8 is about 35.). The retrieved cloud fraction is called the effective cloud fraction. From TOMS and GOME experience with pixel areas of a few hundred km^2, we know that a pixel-averaged cloud albedo of 0.8 is about the maximum that occurs. Therefore, the retrieved effective cloud fraction for OMI will lie between 0 and 1.

For most cases, namely clouds over dark surfaces like ocean (dark in the visible) and vegetation and soil (dark in the UV), the thick cloud model works well. For clouds over bright surfaces like snow and ice, some algorithms need another cloud model, in which the cloud fraction is assumed to be one, but the cloud optical thickness is allowed to vary. This is called the thin cloud model, in which a cloud is assumed to consist of scattering particles, and the interaction between light transmitted through the cloud and the highly reflective surface is incorporated. In this model the cloud optical thickness (which can be large, despite the name “thin” cloud model) is retrieved, and should be used in the cloud correction methods of the trace gas algorithms. The OMI surface UV irradiance algorithm consistently uses this cloud model for both low and high reflecting surfaces. The Raman algorithm is designed to produce cloud results for both the thick and thin cloud model (see Chapter 4).

Cloud fraction

We further consider the thick cloud approximation. The retrieval of cloud fraction c is based on the contrast at TOA between a clear sky scene and the cloudy scene:

$$c = (R_{meas} - R_{clear}) / (R_{cloud} - R_{clear}) . \qquad [1\text{-}1]$$

Here R_{meas} is the measured reflectance, R_{clear} is the reflectance for clear sky, and R_{cloud} is the calculated reflectance of a completely cloudy pixel. Here a Lambertian reflecting cloud with albedo 0.8 is assumed. The clear sky reflectance of the pixel should be calculated or determined from a surface albedo database (for example based on a time series of minimum reflectance data).

Cloud pressure

Two new and complementary approaches have been developed to determine the cloud pressure from OMI. One approach is to use the O_2-O_2 absorption band at 477 nm (see Chapter 2). The O_2-O_2 molecule is a collision-complex of oxygen. Its strongest absorption band in the OMI spectral range lies around 477 nm. Since the vertical density profile of O_2-O_2 is known, namely quadratic with pressure, the column density of O_2-O_2 can be derived from the measured O_2-O_2 band, which leads to the cloud pressure. The DOAS technique that has been developed for

weakly absorbing trace gases can also be used for O_2-O_2. This allows a fast retrieval that is relatively insensitive to noise.

Another approach proposed here is to use the Ring effect in the UV as a measure of cloud pressure, as has been done for SBUV [*Joiner and Bhartia*, 1995; *Joiner et al*., 1995] (see Chapter 3). The Ring effect is the filling-in of solar Fraunhofer lines in light scattered from the Earth, due to rotational Raman scattering by N_2 and O_2. The stronger the filling-in of Fraunhofer lines observed in reflected light at TOA, the higher the pressure of the reflecting surface, including clouds. Raman scattering in the ocean is included in the algorithm (Vasilkov et al., 2002).

Validation of the two cloud pressure algorithms can take place using GOME data, which cover the needed spectral ranges of O_2-O_2 absorption and Raman scattering. The cloud top pressure from GOME can also be derived using the O_2 A-band at 760 nm, for which an algorithm has already been developed and validated [*Koelemeijer et al*., 2001, 2002a].

Cloud detection using small pixel data

We propose to use the small pixel data for cloud detection as follows. Our preferred choice for the small pixel wavelength is 342.5 nm in the UV channel and 388.0 nm in the VIS channel. These wavelengths are outside strong atmospheric absorption lines and solar Fraunhofer lines. The small pixel reflectances at these wavelengths can be used for cloud detection by comparison with clear sky reflectances computed using the TOMS or GOME database of UV surface albedos [*Herman and Celarier*, 1997; *Koelemeijer et al.*, 2002b].

Another possibility of using the small pixel data for cloud detection is by looking at the variability of the reflectances. We propose to compute the standard deviation of 9 adjacent small pixel reflectance values as a measure of scene variability per $13 \times 24\ \mathrm{km}^2$ pixel. Of these 9 values, 5 values come from the pixel under consideration, 2 from the previous pixel and 2 from the next pixel. This variability measure will be given in the level-2 product of the cloud algorithm.

Since the small pixel data wavelengths have been chosen to be 342.5 and 388.0 nm, the small pixel reflectances can also be used to derive the UV absorbing aerosol index (see Sect. 1.2.2) at the subpixel scale.

Cloud mask

For the aerosol retrieval algorithm (Chapter 4), a cloud mask is needed. Such a cloud mask is a number indicating whether is pixel is cloud-free or not. Suggested cloud mask numbers are: 0=cloud-free, 1= (partly) cloudy, 2=uncertain, 3=snow/ice.

The cloud mask will be the result of several tests, in order to have the most reliable detection of cloud-free pixels. The following tests can be performed, where thresholds have to be chosen on the basis of experience and OMI's radiometric accuracy (better than 0.01):

1. Reflectance threshold, combined with aerosol absorption index: reject all pixels brighter than some reflectance threshold (depending on the surface albedo) that have a UV aerosol index near or below zero. This condition avoids removing bright pixels due to a high mineral dust or biomass burning aerosol load (see Chapter 4).
2. Cloud fraction threshold: reject all pixels with effective cloud fraction (as given in the level-2 cloud product) larger than some threshold value.
3. Small pixel variability threshold: reject pixels with variability larger than some threshold value.

1.2.2. Aerosol retrieval algorithm

The OMI aerosol algorithm (Chapter 4) has been designed to produce the optical thickness and single scattering albedo of the tropospheric aerosol over ocean and land. The algorithm is based on the interpretation of the continuum reflectance in the range 331-500 nm as measured by OMI, for cloud-free pixels on a daily basis. In the retrieval look-up-tables created with a detailed radiative transfer model are used, with as input a database of surface albedos and a-priori knowledge of aerosol types.

Input data

For cloud-free pixels the reflectance at TOA is influenced by surface reflection, which must be included in aerosol retrieval. To minimize the surface contribution, the algorithm uses the fact that in the UV most land surfaces (vegetation, dry soils) as well as the ocean are dark, whereas in the visible only the ocean is dark. The surface albedo database for aerosol retrieval is essential. The potential sources are, for the UV only, the TOMS database [*Herman and Celarier*, 1997; *Herman et al.*, 2001], and for the UV and visible the GOME database [*Koelemeijer et al.*, 2002b], and, when available, the MODIS surface albedo data product.

Aerosols can have many different optical properties. In the algorithm a look-up-table of aerosol optical properties is used, which follow from Mie calculations using 24 aerosol types (size distributions and refractive indices) from AERONET [*Holben et al*., 1998].

Also Rayleigh scattering significantly contributes to the reflectance in the UV and visible. However, this contribution can be modeled very accurately.

Retrieval

After an initial selection based on geographical location and season, aerosol types are selected using so-called aerosol indices. These are colour indices, which are obtained by comparing the measured reflectance ratio at two wavelengths to the calculated reflectance ratio using a Rayleigh atmosphere only with an assumed surface albedo. Using two pairs of wavelengths (342.5 / 388 nm, and 388 / 494.5 nm), a UV aerosol index and a visible aerosol index, respectively, will be produced. The UV index appears to be relatively insensitive to scattering aerosol layers or clouds, because it is mainly determined by the reduction of Rayleigh multiple scattering due to aerosol absorption (see Chapter 4). Due to its insensitiveness to clouds, the UV index can also be used to monitor the global transport of UV absorbing aerosols (desert dust and biomass-burning aerosols).

The algorithm for retrieval of aerosol optical thickness and single scattering albedo follows two approaches. The first approach is to use the full spectral coverage of OMI, using 17 selected wavelengths between 330 and 500 nm. The multispectral optical thickness is found from a non-linear fit algorithm using the aerosol type database. From the retrieved aerosol type the single scattering albedo is determined. This multi-wavelength algorithm, which is based on GOME experience [*Veefkind et al.*, 2000], will in the first instance be used over ocean, which is dark in the visible. Later, when accurate land surface albedos become available in the visible (e.g. from MODIS), it will also be used over land.

The other approach, called the near-UV method, has already been used successfully for aerosol retrieval from TOMS [*Torres et al*., 1998]. It will extend the TOMS data record of aerosols [*Torres et al.*, 2002] with the OMI mission period. In the near-UV method the reflectances at 342.8 and 388 nm are used to retrieve directly the optical thickness and single scattering albedo.

For the core validation of the OMI aerosol product, detailed aerosol microphysical measurements are needed from ground-based and airborne platforms. For the long-term

validation, the AERONET ground-based measurements [*Holben et al*., 1998] will be the main data set.

1.2.3. Surface UV irradiance algorithm

The irradiance product is the result of a radiative transfer model calculation, using the following input parameters: the OMI total ozone column and the scene reflectances at 340 and 380 nm. Other input parameters, such as extraterrestrial solar irradiance, surface albedo, ozone profiles, etc., are taken from climatologies or external sources. The specific product is the downward spectral irradiance at the ground at 305, 310, 324, and 380 nm (in $W/m^2/nm$) and the erythemally weighted irradiance (in W/m^2).

The surface UV algorithm consists of a calculation for the clear sky case, extended with corrections in case of clouds (or non-absorbing aerosols) and absorbing aerosols. The cloud and absorbing aerosol information is obtained from the reflectances at 331 and 360 nm. In the real atmosphere, in the absence of snow/ice and clouds, the accuracy of the UV product is limited by the imperfect knowledge of aerosol properties and pollutants in the boundary layer.

The heritage of the surface UV algorithm is based on experience with TOMS [*Eck et al.*, 1995; *Krotkov et al.*, 1998; *Krotkov et al.*, 2001]. The surface UV algorithm for OMI will be the same as for TOMS and GOME (FMI products), so that continuity from the TOMS to the OMI data product is guara.nteed for long-term UV trend analysis. Of course, the OMI advantage of the smaller pixel size (13×24 km^2) as compared to TOMS (about 50×50 km^2) will be used.

The current version of the TOMS surface UV algorithm is described by Krotkov et al. [1998, 2001]. An important new addition, included in the present ATBD, is to take the actual snow thickness and albedo obtained from the ECMWF analysis into account [*Arola et al*., 2002]. This will yield better surface UV estimates at high latitudes.

Validation of the surface UV product will be done with existing time series of UV irradiance measurements at the ground. In addition, special field experiments for UV irradiance validation are proposed for polluted (especially absorbing aerosol) and clear atmospheres.

1.3. References

Arola A., J. Kaurola, T. Tikkanen, L. Koskinen, P. Taalas, J. Herman and N. Krotkov, A new approach to estimate the albedo for snow-covered surface in space-borne UV retrieval method, to be submitted to *J. Geophys. Res*., 2002.

Eck, T.F., P.K. Bhartia, and J.B. Kerr, Satellite Estimation of spectral UVB irradiance using TOMS derived ozone and reflectivity, *Geophys. Res. Lett*., *22*, 611-614, 1995.

Fischer, J., and H. Grassl, Detection of cloud-top height from backscattered radiances within the oxygen A-band. Part 1: Theoretical study, *J. Appl. Met., 30*, 1245-1259, 1991

Herman, J.R., P.K. Bhartia, J. Ziemke, Z.Ahmad, and D. Larko, UV-B increases (1979-1992) from decreases on total ozone, *Geophys. Res. Lett*., 23, 2117-2120, 1996.

Herman, J.R., and E. Celarier, Earth surface reflectivity climatology at 340 and 380 nm from TOMS data, *J. Geophys. Res., 102,* 12,059-12,076, 1997

Herman, J. R., E. Celarier, and D. Larko, UV 380 nm reflectivity of the Earth's surface, clouds and aerosols, *J. Geophys. Res*., *106*, 5335-5351, 2001.

Holben, B., et al., AERONET – A federated instrument network and data archive for aerosol characterization, *Remote Sens. Environ., 66*, 1-16, 1998

Joiner, J., and P.K. Bhartia, The determination of cloud pressures from rotational Raman scattering in SBUV measurements, *J. Geophys. Res*, *100*, 23019-23026, 1995

Joiner J., et al., Rotational Raman scattering (Ring effect) in SBUV measurements, *Appl. Opt*. *34*, 4513-4525, 1995

Kerridge, B.J., et al., Definition of mission objectives and observational requirements for an Atmospheric Chemistry Explorer mission, Final Report, ESA Contract 13048/98/NL/GD, ESTEC, Noordwijk, The Netherlands

Koelemeijer, R.B.A., and P. Stammes, Effects of clouds on the ozone column retrieval from GOME UV measurements, *J. Geophys. Res., 104*, 8281-8294, 1999

Koelemeijer, R.B.A., P. Stammes, J.W. Hovenier, and J.F. de Haan, A fast method for retrieval of cloud parameters using oxygen A-band measurements from GOME, *J. Geophys. Res., 106*, 3475-3490, 2001

Koelemeijer, R.B.A., P. Stammes, J.W. Hovenier, and J.F. de Haan, Global distributions of effective cloud fraction and cloud top pressure derived from oxygen A-band spectra measured by the Global Ozone Monitoring Instrument: Comparison to ISCCP data, *J. Geophys. Res., 107*, D12, pp. AAC 5-1 to AAC 5-9, 2002a

Koelemeijer, R.B.A., J.F. de Haan, and P. Stammes, A database of spectral surface reflectivity in the range 335-772 nm derived from 5.5 years of GOME observations, *J. Geophys. Res., accepted*, 2002b

Krotkov, N. A., P.K. Bhartia, J. R. Herman, V. Fioletov and J. Kerr, Satellite estimation of spectral surface UV irradiance in the presence of tropospheric aerosols 1: Cloud-free case, *J. Geophys. Res., 103*, 8779-8793, 1998

Krotkov, N. A., P.K. Bhartia, J. Herman, Z. Ahmad, V. Fioletov, Satellite estimation of spectral surface UV irradiance 2: Effect of horizontally homogeneous clouds and snow, in print, *J. Geophys. Res., 106*, 2001

Levelt, P., and the OMI Science Team, Scientific Requirements Document for OMI-EOS, Report RS-OMIE-KNMI-001, KNMI, De Bilt, The Netherlands, December 2000

Madronich, S., Implications of recent total ozone measurements for biologically active UV radiation on reaching the Earth's surface, *Geophys. Res. Lett., 19*, 37-40 , 1992

McPeters et al., R.D., Nimbus-7 total ozone mapping spectrometer (TOMS) data products user's guide, NASA reference publication 1384, April 1996

Rossow, W.B., and L.C. Garder, Cloud detection using satellite measurements of infrared and visible radiances for ISCCP, *J. Clim., 6*, 2341-2369, 1993

Smith, W.L., and C.M.R. Platt, Comparison of satellite-deduced cloud heights with indications from radiosonde and ground-based laser measurements, *J. Appl. Met., 17*, 1796-1802, 1978

Torres, O., P.K. Bhartia, J.R. Herman, Z. Ahmad and J. Gleason, Derivation of aerosol properties from satellite measurements of backscattered ultraviolet radiation, Theoretical Basis, *J. Geophys. Res.*,103, 17099-17110, 1998

Torres, O., P.K. Bhartia, J.R. Herman, A. Sinyuk, P. Ginoux, and B. Holben, A long term record of aerosol optical depth from TOMS observations and comparison to AERONET measurements, *J. Atm. Sci.*, 59, 398-413, 2002

Vasilkov, A.P., J. Joiner, J.F. Gleason, and P.K. Bhartia, Ocean Raman scattering in satellite backscatter ultraviolet measurements, *Geophys. Res. Lett.*, in press, 2002

Veefkind, J.P., G. de Leeuw, P. Stammes and R.B.A. Koelemeijer, Regional distribution of aerosol over land derived from ATSR-2 and GOME, *Remote Sens. Environ., 74*, 377-386, 2000

WMO99, (Herman, J.R. et al.) Ultraviolet radiation at the Earth's surface, Chapter 9 in: Scientific Assessment of Ozone Depletion, 1998, *World Meteorological Organization, Global Ozone Research and Monitoring Project - Report No. 44*, Geneva, Switzerland, 1999

2. Cloud pressure algorithm based on O_2-O_2 absorption

Juan R. Acarreta and Johan F. de Haan
Royal Netherlands Meteorological Institute (KNMI), De Bilt, The Netherlands

2.1. Introduction

OMI is a wide field-of-view-spectrometer with a spectral resolution of 0.6 nm and sampling of 0.2 nm in the range 350-500 nm (defined as the *visible* channel). Other imaging spectrometers than OMI, e.g. the Global Ozone Monitoring Experiment (GOME) on board ESA's ERS-2 platform, observe a wide spectral interval and use the absorption by the O_2 A-band near 762 nm to derive cloud information. As the O_2 A-band, as well as other O_2 bands, lie outside the spectral range of OMI, other spectral regions and other processes are required to derive cloud information from OMI spectra. In this chapter absorption by O_2-O_2 near 477 nm is used, which is the strongest absorption feature by O_2-O_2 that is detected by OMI.

We are not aware of other algorithms that derive cloud information using the O_2-O_2 absorption 477-nm band. Hence, the algorithm presented here is to be regarded as a first step. Significant improvements might be possible, for instance if the inverse model is changed in order to work with clouds that are more realistic. *Deschamps et al.* [1994] presented a preliminary sensitivity study about the use of the O_2-O_2 477 nm band to retrieve the altitude of clouds in combination with the O_2-A band for GOME. They concluded that the use of the O_2-O_2 band requires a high signal to noise ratio and that the retrieved level is near the midlevel of the cloud. In addition, they found that, due to a lower surface reflectivity at 477nm than at 760 nm, O_2-O_2 could provide a better retrieval over vegetated surfaces than the O_2-A band. However, in the proposed operational retrieval algorithm for GOME, only the O_2-A band was taken into account.

The physical basis of our algorithm may be summarized as follows. Clouds reduce the probability that photons reach the atmosphere below the clouds and are then scattered back to the OMI instrument. Hence, the average atmospheric path length of photons detected by OMI decreases when clouds are located higher in the atmosphere. As shorter path lengths decrease the probability of absorption by O_2-O_2, the depth of the O_2-O_2 absorption feature is a measure for the altitude of the clouds.

However, the determination of cloud level pressure is less straightforward than suggested by the reasoning given above. First, absorption by O_2-O_2 increases with the square of the pressure, so that longer path lengths high in the atmosphere have less effect than longer path lengths low in the atmosphere. Second, two cloud layers or a cloud layer above a snow-covered surface will act as a photon trap. Once inside such a trap, photons can travel large distances, thereby enhancing the O_2-O_2 absorption signature. The absorption signature that is detected in the spectrum of light reflected by a cloudy pixel is therefore a complicated balance between the reduced probability of photons reaching the detector and enhanced absorption signatures due to photon trapping. In the following sections we will show that in most cases the O_2-O_2 absorption feature can indeed be used to derive information on the altitude of clouds. An exception holds for clouds above snow-covered (i.e., high albedo) surfaces, where the retrieved pressure represents the pressure of a level near the ground.

The complications mentioned above make it difficult to predict the relationship between the cloud height and the strength of the O_2-O_2 absorption feature. Our approach resembles the approach used for the O_2 A-band as has been done by *Koelemeijer et al*. [2001]. In our inverse model (retrieval model) we replace a cloud by an opaque Lambertian reflector. This is a crude approximation, because it ignores the photon trapping mentioned above. However, it has the

advantage that the altitude of the Lambertian reflector is well defined, in contrast to a vertically extended cloud. The cloud pressure that is derived is then the pressure level of the Lambertian surface that gives the same spectral signature at the top of the atmosphere as the real cloud does. This spectral signature is represented by a slant column density and a representative value of the continuum reflectance. Note also that this same model is used in the trace gas retrieval algorithms for OMI, and it is therefore appropriate for performing cloud correction in these algorithms.

Next, we investigate the relationship between the properties of realistic scattering cloud (altitude and vertical extent) and the derived pressure level of a Lambertian cloud. This investigation uses radiative transfer calculations to simulate the O_2-O_2 absorption features of realistic clouds. These simulations (the forward model) are described in Section 2.3. The inverse model, where the cloud is approximated with a Lambertian reflector, is described in Section 2.4. The accuracy of the retrieved cloud pressure is reported in Section 2.5. Some remarks on validation of the algorithm and the derived cloud pressure are given in Section 2.6. Finally, in Section 2.7 are the concluding remarks.

2.2. Algorithm overview

In this overview of the cloud pressure algorithm based on O_2-O_2 absorption, the required input is described, the algorithm is outlined, and the output is specified. Throughout this document we will use also the cloud altitude z_L instead of the cloud pressure p_L. To relate both quantities we use the pressure profile that was used during the calculation of the look-up tables in combination with the ground altitude. This profile, the ground altitude, and the ground albedo can be understood as *a priori* information needed by the retrieval procedure.

INPUT

- OMI irradiance and radiance spectra (460 - 490 nm)
- Geometrical information on the pixel involved
- Ground surface albedo from database
- Ground altitude from database
- Absorption cross-section of O_2-O_2
- Look-up tables generated by a DOAS fit on spectra created with the inverse model, in which the cloud layer is replaced by a Lambertian surface with an albedo A_L = 0.80. The look-up tables represent the functional dependence $z_L = z_L(R_c, N_s)$ and $c_L = c_L(R_c, N_s)$, where $R_c = R(l_o)$ is the continuum reflectance at λ_o and N_s is the O_2-O_2 slant column density, both of which are obtained from the DOAS fit. z_L is the altitude of the Lambertian surface and c_L is the effective cloud fraction. The functional dependencies change with the solar zenith angle, viewing zenith angle, azimuth difference between the incident sunlight and the viewing direction, and the ground albedo and ground altitude. Hence, table entries are created to cover all relevant geometries and ground albedo and ground altitude values.

ALGORITHM

- From the measured radiance and irradiance spectra a reflectance spectrum is made, and a DOAS fit is applied to this reflectance spectrum, yielding the continuum reflectance, R_c, the O_2-O_2 slant column density, N_s, and an error covariance matrix S_e for this spectrum.
- From these values of R_c and N_s the Lambertian cloud altitude (z_L) and Lambertian cloud fraction (c_L) are calculated using a LUT interpolation with $c_L = c_L(R_c, N_s)$ and $z_L = z_L(R_c, N_s)$. Next, the cloud altitude z_L is translated to the cloud pressure, p_L.
- Errors in z_L and c_L are calculated, using the diagonal elements of the covariance matrix S_e and an error propagation formula, which contains the derivatives calculated from the lookup tables. Finally, the error in z_L is translated into an error in p_L

OUTPUT

The following output will be generated for each pixel

- Cloud pressure level (p_L) and its error.
- Effective cloud fraction (c_L) and its error.

2.3. Forward model

The forward model is used to simulate reflectance spectra for realistic optical properties of the atmosphere. By applying our retrieval algorithm to these spectra, the performance and accuracy of the retrieval algorithm is investigated. In this section, we first consider the O_2-O_2 absorption cross-section, which is followed by an illustration of the expected spectral reflectance for different cloud altitudes. Next, we briefly discuss the independent pixel approach, and the cloud models we use. Finally, we briefly discuss the radiative transfer code used for the simulations.

2.3.1. Absorption by the O_2-O_2 collision complex

Absorption by the O_2-O_2 collision complex has been described in several publications. *Vigasin* [2000] considers a classification in tightly bound states, metastable states, and free states, whose relative contribution depends on the temperature. For atmospheric temperatures the tightly bound state is unimportant and most of the absorption is due to the free states. *Blickensderfer and Ewing* [1969], *Long and Ewing* [1973], *Greenblatt et al.* [1990], *Newnham and Ballard* [1998], and *Naus and Ubachs* [1999] discuss laboratory measurements of the O_2-O_2 absorption cross-section, providing information on pressure and temperature dependence of this cross-section. *Naus and Ubachs* [1999] confirm that the absorption increases with the square of the pressure.

For our forward and inverse model calculations we choose to use the absorption spectra measured by *Newnham and Ballard* [1998]. More accurate spectra will presumably become available in the near future. Fig. 2.1 shows the spectral absorption cross-sections at several temperatures. Linear interpolation is used to obtain the cross-section at an appropriate temperature (as for example 253 K). The data shown in the Fig. 2.1 have been smoothed to avoid small-scale structures (“noise”) visible in the original data.

The absorption cross-section of the O_2-O_2 collision complex has a peculiar dimension (cm^5 $molecule^{-2}$), because the absorption is proportional to the square of the number density of

the colliding molecules. In the radiative transfer calculations the atmosphere is divided in a number of layers and the absorption optical thickness of O_2-O_2 in a particular layer is:

$$t_{O2-O2}(l) = \int_{z^{bot}}^{z^{top}} s_{O2-O2}(T(z), l)\, n_{O2}(z)\, n_{O2}(z)\, dz \qquad [2\text{-}1]$$

where z^{top} and z^{bot} are the altitudes of the top and bottom of the layer, $s_{O2\text{-}O2}(T(z),l)$ is the temperature dependent absorption cross-section of the collision complex (in cm^5 $molecule^{-2}$) and $n_{O2}(z)$ is the number density (in molecule cm^{-3}) of the oxygen molecules in that layer.

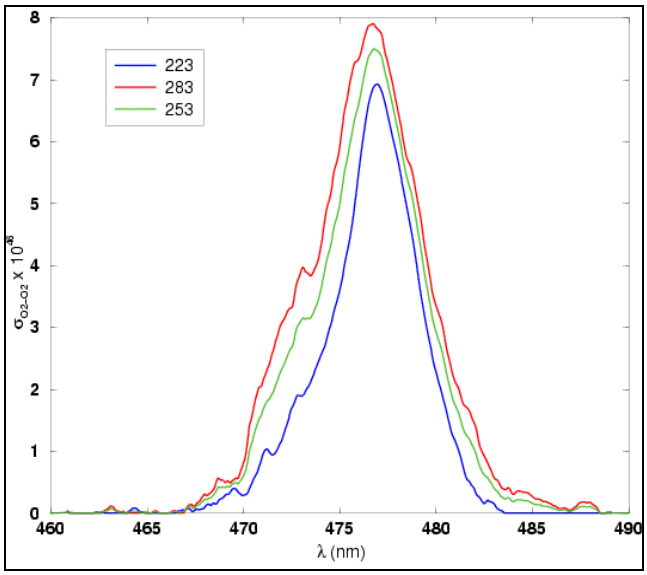

Fig. 2.1 *Absorption cross-section of the O_2-O_2 collision complex near 477 nm, based on measurements by Newnham and Ballard [1998] at 283 K (red curve) and 223 K (blue curve). The curve for 253 K (green) was obtained by interpolation.*

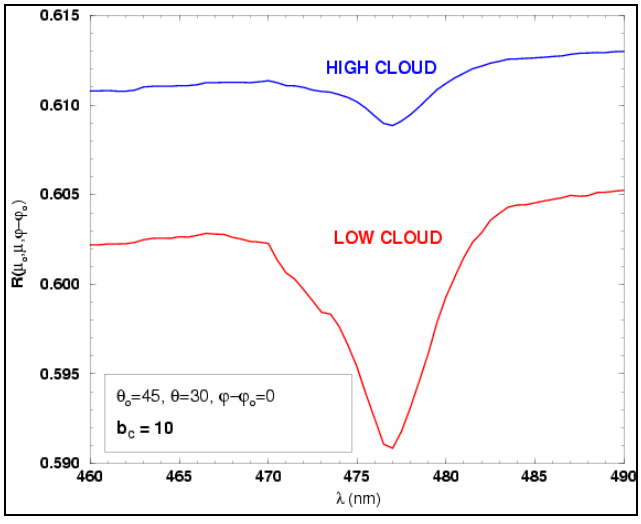

Fig. 2.2 *Simulated reflectance spectra around 477 nm for a pixel fully covered by clouds. Curves are plotted for clouds between 1-2 km ("low cloud") and 7-8 km ("high cloud"). Each cloud has a vertical extent of 1 km and an optical thickness equal to 10. The albedo of the Lambertian ground surface is 0.05.*

The spectral reflectance *R* of an OMI pixel is obtained from the Level 1b product. It is defined as $p\,L/E$, where *L* is the reflected radiance of a particular pixel and *E* is the corresponding solar irradiance incident on that pixel (per unit area of the atmosphere). The reflectance depends on many parameters, among which the wavelength, the viewing zenith angle q, the solar zenith angle q_0, and the azimuth difference between the viewing direction and the incident sunlight $j - j_0$. To illustrate the effect of cloud altitude, Fig. 2.2 shows simulated reflectance spectra for clouds at different altitudes. Clearly, the depth of the absorption feature is larger for low-altitude clouds. Note that the effect of the expected S/N value for OMI at 477 nm (≈1000) will be similar to the smallest division used in the Y-axis (reflectance values).

2.3.2. Independent pixel approximation

We shall use the *independent pixel approximation*, and apply it to sub-pixels. It is assumed that a pixel can be divided into sub-pixels and that the measured reflectance of the pixel is the average of the reflectance of the sub-pixels. Moreover, we assume that for each pixel a plane-parallel atmosphere model can be used to calculate the reflectance. That is, we assume that there is no net lateral transport of radiation between sub-pixel boundaries [see for example *Chambers et al.*, 1997, and references therein]. Consequently, sides of clouds and shadows cast by clouds are ignored in our model. We divide the sub-pixels into cloud-covered sub-pixels and clear sub-pixels, and assume that for a cloudy sub-pixel there is only one cloud layer. In addition, we assume that that the cloud top, cloud bottom, and cloud optical thickness is the same for each cloud-covered sub-pixel, and that the surface albedo is the same for each sub-pixel. The reflectance of each OMI pixel is then given by:

$$\begin{aligned} &R(l,q,q_0,j-j_0;c,z^{top},z^{bot},t_c,A_s) = \\ &c\,R^{cloud}(l,q,q_0,j-j_0;z^{top},z^{bot},t_c,A_s)+(1-c)\,R^{clear}(l,q,q_0,j-j_0;A_s) \end{aligned} \qquad [\,2\text{-}2\,]$$

where *c* is the cloud fraction, z^{top} the cloud top height, z^{bot} the cloud bottom height, t_c the cloud optical thickness, and A_s the surface albedo.

2.3.3. Cloud models

In the previous section clouds were characterized by the parameter values z^{top}, z^{bot}, and t_c. In general, clouds are more complex and additional parameters are required to describe them, even in a plane-parallel approximation. Important additional parameters are: (i) the effective radius of the cloud particles (radius weighted by the geometrical cross-section), (ii) the effective variance of the radius of the cloud particles, and (iii) the refractive index of the water droplets in the cloud (with the imaginary part assumed to be equal to zero). Values of the cloud parameters that are used in our simulation studies are given in Table 2.1.

Table 2.1 Parameter values for the cloud models used in our simulation studies

real cloud fraction, *c*	0.0, 0.1, 0.2, 0.3, …, 1.0
altitude (z^{top}, z^{bot}) in km	lower boundary at 1,3,5,7 and vertical extent 1,3,5
cloud optical thickness, t_c	0.1, 1, 10, 50, 100
effective radius (μm)	0.5, 1.0, 5.0, 10
effective variance	0.12
refractive index	1.33
Geometry (degrees)	θ_0, θ= 0, 15, 30, 45, 60, 75 φ-φ_0= 0, 30, 90, 135, 180

Concerning the cloud-drop sizes used in our simulations, we explored the effects of small (0.5 and 1 μm), medium (5 μm), and large (10 μm) particles. The main conclusion was that the size of the particles has little effect on the reflectance spectrum Therefore, we also expect little difference between cold clouds composed of ice particles and warm clouds, composed of water droplets. For this reason, our simulations were restricted to warm clouds.

2.3.4. Simulation of spectral reflectance

Reflection spectra are usually simulated for the wavelength interval (460 nm - 490 nm), covering the O_2-O_2 absorption feature and regions where no absorption by O_2-O_2 takes place. In all cases the spectral sampling was 0.2 nm. The single-scattering properties of the cloud particles are calculated using Mie theory, employing a two-parameter gamma distribution to model the size distribution of the particles, according to the values listed in Table 2.1. The code used is described in *de Rooij and Van der Stap* [1984]. The Mie code provides the coefficients for the expansion of the scattering matrix in generalized spherical functions, which are subsequently used in the doubling-adding radiative transfer code called DAK [*de Haan et al*., 1987, *Stammes et al*., 1989; *Stammes*, 2001]. Polarization effects are taken into account. Generally, calculations are performed for a 35-layer atmosphere. Various temperature/pressure profiles can be chosen. Mostly the Mid-latitude Winter Profile [*Anderson et al.*, 1986] was used. Trace gases and aerosols can be added if desired. Generally, calculations were performed without aerosols and trace gases, except for the O_2-O_2 collision complex.

2.4. The inverse model

The inverse model is the same as the forward model, but the scattering cloud is replaced by an opaque Lambertian surface with a fixed albedo A_L situated at a height z_L which covers a fraction c_L of a pixel. The reflectance of a pixel for the inverse model is then given by:

$$R(l,q,q_0,j-j_0;c_L,z_L,A_s) = c_L R^L(l,q,q_0,j-j_0;z_L,A_L=0.8) + (1-c_L)R^{clear}(l,q,q_0,j-j_0;A_s) \qquad [2\text{-}3]$$

The albedo A_L has a fixed value equal to 0.8, based on studies by Koelemeijer and Stammes [1999]. They found that A_L= 0.8 yielded the best results for ozone column density retrievals. We use this number in order to be compatible with other retrieval algorithms. We note, however, that this choice introduces a systematic difference with respect to the real cloud fraction (c in Eq. [2-2]) . Hence, the sporadic use of the term “effective” when we refer to the cloud fraction. Note that although real and Lambertian (or effective) cloud fractions are not the same, they are highly correlated.

The altitude of the Lambertian reflector, z_L, will be used to represent the altitude of real clouds. Great care should be used in the interpretation of this quantity due to the difference between “altitude of the Lambertian reflector” and “altitude of the real cloud”. The altitude of a real cloud is not unambiguously defined, because a cloud has a vertical extent. We could choose the top, the bottom or some other level such as the middle (equidistant from top and bottom) of the cloud as a representative level.

In this ATBD we will consider the midlevel as the representative level of a real cloud. The choice of the midlevel is based on results of a sensitivity study using the forward model. Usually the retrieved Lambertian level z_L is near the midlevel of the real cloud (Fig. 2.3). However, we do not always retrieve the same level. Depending on the cloud fraction, optical thickness, vertical extent, altitude, geometry and surface albedo, we retrieve a level that can be above or below the midlevel.

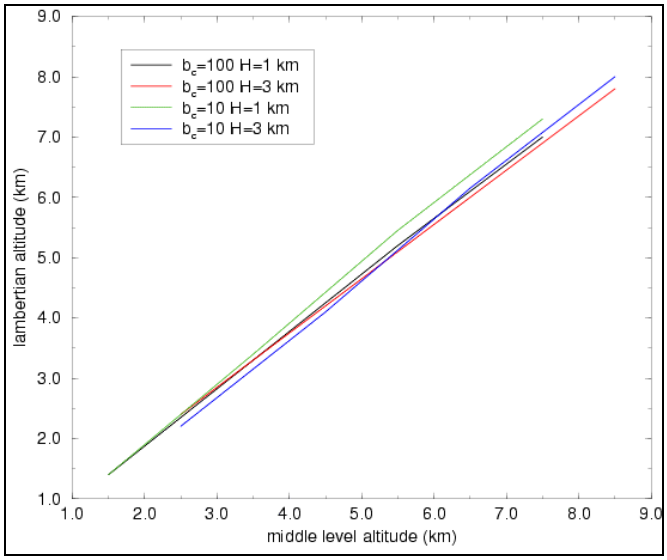

Fig. 2.3 *An example of the relationship between the mid cloud altitude used in the forward model and the retrieved Lambertian cloud altitude. Results for two optical thicknesses (t_c = 10 and 100) and two values of the geometrical extent (H=1, 3 km) of the cloud are given for a representative geometry (q_O=45°, q =30°, $j - j_O$=0°). The real cloud fraction is c=0.3 and the surface albedo is A_S=0.05.*

2.4.1. Retrieval algorithm

The retrieval algorithm consists of two steps. First a DOAS fit is made to determine the continuum reflectance and the slant column density of O_2-O_2. The fit window is 460 nm - 490 nm. Second, a look-up table (see the section 2.4.2) is used to determine the altitude, z_L, and the Lambertian (or effective) cloud fraction c_L. Other approaches, such as a detailed analysis of the shape of the band (for example using both the depth of the band and the FWHM), fail because the O_2-O_2 absorption is weak. Sensitivity studies show that such other approaches become worthwhile only if the signal-to-noise ratio would be a factor of 10-100 better than what is expected for OMI.

The DOAS equation that is used reads:

$$-\ln R(l) = g_1 + g_2 l + N_s s_{O2-O2}(l) + N_{s,O3} s_{O3}(l) \qquad [2\text{-}4]$$

where $R(l)$ is the spectral reflectance, $-\ln R_c = g_1 + g_2 l_o$, where R_c is the continuum reflectance at l_o, N_s is the slant column density of O_2-O_2, and $s_{O2-O2}(l)$ is the absorption cross-section at a representative temperature (throughout this document equal to 253 K). Note also that the effects of absorption by O_3 are taken into account by adding the term with the cross section $s_{O3}(l)$ and the fitted slant column density $N_{s,O3}$. Other absorbers, such as NO_2, are not included because sensitivity studies showed that only ozone interferes significantly with O_2-O_2. The reference wavelength l_o is fixed to the middle value of our fit window, i.e., $l_o = 475\,\text{nm}$. In the actual computations, Singular Value Decomposition is used to obtain the best fit [*Press et al.*, 1992]. Finally, the accuracy of the fitted parameter values is obtained from the covariance matrix. In the retrieval, values of c_L and z_L are obtained by interpolating in the look-up tables.

2.4.2. Look-up Tables

The DOAS fit can be applied to a measured spectrum, but also to spectra simulated by using Eq. [2-3], in order to generate look-up tables. For fixed values of the geometry, ground surface albedo, and ground surface altitude, one obtains from the DOAS fit R_c as a function of c_L and z_L. Similarly, N_s is a function of these parameters. These functions, defined as $R_c^{sim}(c_L, z_L)$ and $N_s^{sim}(c_L, z_L)$ are tabulated for c_L = 0.00 … (0.01)… 1.00 and z_L = 0.0 … (0.1)… 9.0 km. As each (c_L, z_L) combination corresponds uniquely with a (R_c, N_s) combination, it proved possible to create new look-up tables representing the functions $c_L(R_c, N_s)$ and $z_L(R_c, N_s)$. These new look-up tables can directly be used to find (c_L, z_L) for a given value of (R_c, N_s). Such look-up tables were created for all relevant geometries, ground surface albedos and ground surface altitudes.

2.5. Error analysis

This section is devoted to the errors expected in the final products c_L and z_L. There are two main sources of errors. First, we have an error due to detector noise, which translates into an error in the continuum reflectance, $e(R_c)$, and an error in the slant column density, $e(N_s)$. These errors are calculated during the DOAS fit. Second, we have a number of systematic errors, the most important of which is the representation of the cloud by a Lambertian reflector. In the remaining part of this section we first consider the errors due to noise and then discuss systematic errors.

To calculate the errors $e(c_L)$ and $e(z_L)$ in the retrieved quantities c_L and z_L, we consider c_L and z_L as implicit functions of R_c and N_s . Calculations have shown that the correlation between the errors is small and can, therefore, be ignored. Hence, we can use a simplified error propagation formulae, yielding:

$$e^2(c_L) \approx \left(\frac{\partial c_L}{\partial N_s}\right)^2 e^2(N_s) + \left(\frac{\partial c_L}{\partial R_c}\right)^2 e^2(R_c)$$
$$e^2(z_L) \approx \left(\frac{\partial z_L}{\partial N_s}\right)^2 e^2(N_s) + \left(\frac{\partial z_L}{\partial R_c}\right)^2 e^2(R_c) \qquad [2\text{-}5]$$

The derivatives in Eq. [2-5] are calculated from the look-up tables. Table 2.2 shows the O_2-O_2 slant column fitting error $e(N_s)$ for two geometries (case 1: $q_0 = 45^o$, $q = 30^o$, $j - j_0 = 0^o$ and case 2: $q_0 = 60^o$, $q = 60^o$, $j - j_0 = 0^o$), various S/N ratios, and two values of the surface albedo. The error listed is the mean value of the errors produced by clouds with lower boundaries at 1, 3, 5, and 7 km, vertical extents of 1 and 3 km, and real cloud fractions of 0.1, 0.5, and 0.9 (forward model cloud fractions). Inspection of Table 2.2 shows that $e(N_s)$= 10 x 10^{41} molecules^2 cm^{-5} can be regarded as a representative number. A similar approach (not shown) provides the representative number $e(R_c)$ = 0.01 for the error in the continuum reflectance

Table 2.2 *Errors in the O_2-O_2 slant column density $e(N_s)$ x 10^{41} ($molecules^2\ cm^{-5}$) for two geometries, three S/N values, three cloud optical thicknesses and two values for the surface albedo (see text for more details).*

		optical thickness=1		optical thickness=10		optical thickness=100	
	S/N	**case 1**	**case 2**	**case 1**	**Case 2**	**case 1**	**Case 2**
A_S=0.05	**2000**	15	5.6	7.5	3.8	5.1	3.3
	1000	30	10	15	7.6	10	6.6
	800	40	11	20	10	13	8.3
A_S=0.25	**2000**	6.6	4.0	4.5	3.0	3.6	2.6
	1000	13	7.8	9.5	5.9	7.1	5.3
	800	16	10	12	7.4	9.0	6.7

Using these representative values for $e(N_s)$ and $e(R_c)$, we can calculate a representative error $e(z_L)$ for each retrieved combination (z_L, c_L). Fig. 2.4 shows the results of such a calculation, but with the altitude z_L replaced by the pressure level p_L. From this figure it is clear that for clouds below 300 hPa and a Lambertian fraction greater than 0.2, the error is less than 50 hPa.

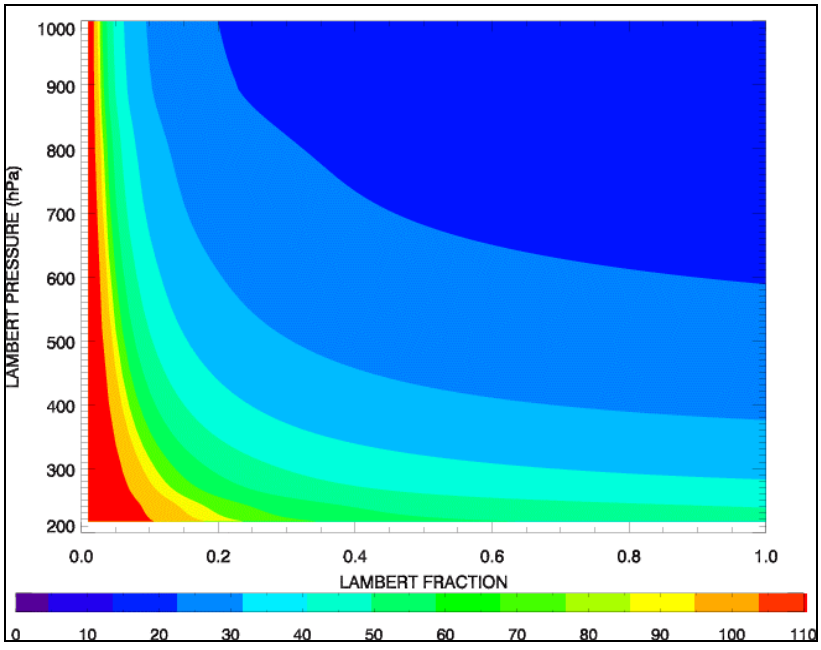

Fig. 2.4 *Error in the cloud pressure $e(P_L)$ in hPa if the surface albedo is A_s=0.05 and q_0=45 , q =30, $j-j_0$=0. The color bar shows the error in hPa; the minimum error is about 15 hPa and occurs for $c_L \approx 1$ and P_L » 1000 hPa. The scientific requirement of 100 hPa corresponds to the orange color.*

The magnitude of the error $e(z_L)$, or equivalently $e(P_L)$, is sensitive to the surface albedo. If A_s increases, the region where $e(P_L)$ > 100 hPa becomes larger, and the orange region in Fig. 2.4 moves towards higher pressures and larger cloud fractions. The error also depends on the

geometry, mainly on the value of the geometrical airmass factor. When it increases, the path length increases, resulting in a higher O_2-O_2 signal, and, therefore, a smaller error.

The error in the Lambertian cloud fraction $e(c_L)$ is, in contrast to $e(P_L)$, nearly independent of the cloud fraction and cloud pressure. In general, $e(c_L) \leq 0.03$ (or 3% if the cloud fraction is 1). This result is expected because the Lambertian cloud fraction mainly depends on the R_c value whereas the pressure level is mainly due to the slant column density. The relative error in the continuum is always small in comparison with the relative error in N_S, resulting in a small error in the Lambertian cloud fraction. In addition, the continuum does not depend significantly on the pressure level of the cloud, because the contribution of Rayleigh scattering at 477 nm is small.

It is expected that the main systematic errors are due to our physical cloud model, namely the approximation of the clouds by a Lambertian reflector. Effects of multiple cloud layers (with or without ice) and the effect of a different distribution of optical thicknesses inside one pixel can only be assessed by an extended forward model. We found from simulations that tropospheric aerosols (absorbing or not) with an optical thickness of one change the cloud fraction over ocean by a small amount, but hardly affect the derived cloud pressure. Apparently, aerosols over ocean mainly increase or decrease the reflectance, but they do not change slant column density of O_2-O_2 in a significant manner.

For a snow covered surface at 1013 hPa, with an assumed albedo of 0.9, calculations show that the retrieved cloud top pressure is near the ground level, whatever the actual altitude of the real cloud, presumably due to photon trapping, which was mentioned in the introduction. Hence, for snow covered surfaces the retrieved cloud pressure does not correspond to the altitude of the real cloud. Research is needed to estimate the effect of this discrepancy on trace gas algorithms that use the retrieved cloud properties.

2.6. Algorithm validation

First the numerical stability of the algorithm is considered. The cloud algorithm consists of two steps: (i) applying a DOAS fit to the reflectance spectrum measured by OMI, resulting in a continuum reflectance and the slant column density of O_2-O_2, and (ii) a look-up table interpolation to derive the effective cloud fraction and the cloud pressure. The first step involves a linear least squares estimate and will be stable, while the second step is very simple. Hence, numerical problems have not been encountered.

Second, internal consistency was tested by simulating the reflectance spectrum with a Lambertian cloud model. In that case the retrieved cloud pressure coincided with the cloud pressure used in the simulations.

Third, our cloud algorithm has been applied to GOME data, not only for testing its robustness, but also to evaluate the relationship between the cloud pressure derived from O_2-O_2 and that derived from the O_2 A-band using the FRESCO algorithm [*Koelemeijer et al*., 2001]. Furthermore, this makes it possible to intercompare cloud pressures derived from ATSR-2, the O_2 A-band, and O_2-O_2 absorption.

As an example of such an intercomparison, Figure 2.5 shows the cloud pressure derived from O_2-O_2 absorption using GOME data (orbit 1337 over the ocean), and pressures derived from FRESCO using the O_2-A band. In addition, pressures derived from ATSR-2 data are shown [see *Koelemeijer et al*., 2001 for details]. Error bars represent the random error, i.e., the error produced by the GOME S/N ratio, calculated using Eq. [2-5]. The mean differences between the derived pressures are: $P_L(O_2\text{-}O_2)\text{-}P_L(O_2\ A) = -69 \pm 59$ hPa and $P_L(O_2\text{-}O_2)\text{-}P_L(ATSR\text{-}2) = 36 \pm 97$ hPa. Concerning the Lambertian cloud fraction, the mean differences between the three procedures are $c_L(O_2\text{-}O_2)\text{-}c_L(O_2A) = -0.01 \pm 0.03$ and $c_L(O_2\text{-}O_2)\text{-}c_L(ATSR\text{-}2) = 0.02 \pm 0.06$

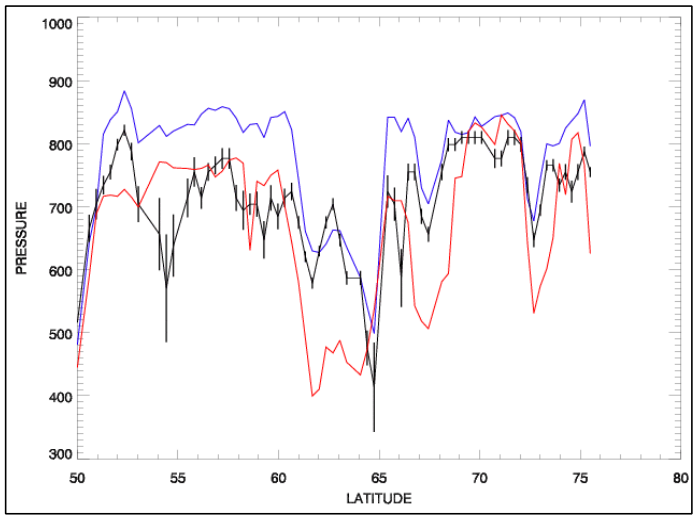

Fig. 2.5 *Inter-comparison of the retrieved cloud pressures along a part of a GOME orbit. Results for different retrieval algorithms are shown: O_2-O_2 (black), O_2-A (blue) and ATSR-2 (red). The vertical error bars (black) represent the random error, i.e, the error calculated as described in Section 2.5*

As can be seen in Fig. 2.5, the random errors are, in general, smaller than the scientific requirement (100 hPa). In fact, the theoretical predictions using OMI simulated data (Fig 2.4) agree very well with the errors found in Fig. 2.5.

Figure 2.6 shows a global comparison between our retrievals using the O_2-O_2 band and results obtained with the O_2-A FRESCO algorithm. The comparison is made for January 2000, using nadir pixels with different illuminations (solar zenith angle) over the ocean. The colors of the figure represent different values for the cloud fraction. The continuous line shows the 1:1 relation between both pressures, and does not represent a fit to the observations. After OMI launch several other comparisons will be made, such as those with CALIPSO and possibly other instruments (as for example CLOUDSAT, MODIS, etc.).

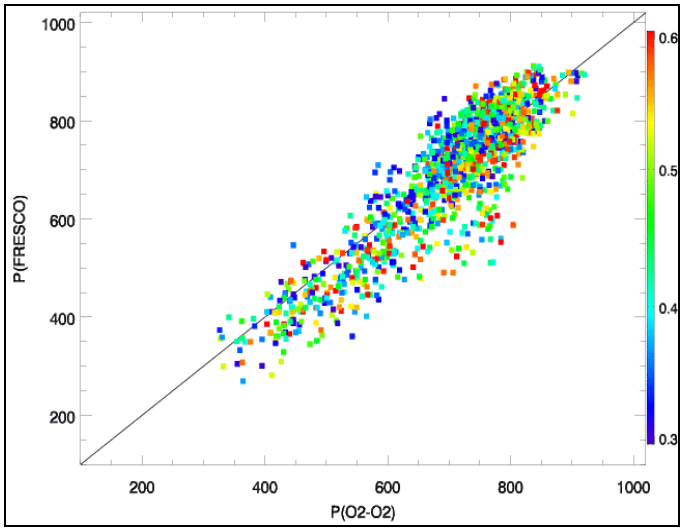

Figure 2.6: *Comparison of cloud pressures derived from the O_2-O_2 and O_2-A band algorithms using GOME data (18-20, January 2002; only nadir pixels over the ocean). The color bar shows the retrieved cloud fraction.*

2.7. Concluding remarks

In this ATBD a method has been described to retrieve cloud products from the O_2-O_2 absorption band at 477 nm. The results obtained so far demonstrate that the algorithm is able to derive cloud fraction and cloud pressure that are similar to those obtained with other algorithms. In addition, it was shown that usually the midlevel of the cloud is retrieved. Finally, the structure of the expected error due to noise was given and some research with regard to systematic errors was reported.

As was mentioned in the introduction, the algorithm described here is a first step. Hence more research is needed to better chart systematic errors and to improve the algorithm. Main issues are:

- More accurate spectroscopic data on the O_2-O_2 absorption cross-section is needed, in particular its temperature dependence.
- In view of photon trapping and because multiple cloud layers often occur, the behavior of the of the algorithm for multi-layered cloud systems needs to be investigated.
- Coupling with trace gas retrieval algorithms is needed to assess a possible cancellation of errors in the retrieved column densities due to errors in the cloud retrieval algorithm.
- Coupling of the algorithm with the algorithm based on the filling in of Fraunhofer lines due to rotational Raman scattering (see Chapter 3 of this volume) might yield an improved algorithm and should be investigated.
- It should be investigated whether the use of UV wavelengths can help constrain the value of the assumed cloud albedo, which is now fixed at 0.8. This might yield a more realistic cloud fraction and reduce errors in the derived trace gas column densities.
- The radiative transfer model now uses a plane-parallel approximation, and should be extended so that it can deal with a spherical shell atmosphere. This is most important for low solar elevations.
- The effects of more realistic cloud models that account for the 3D nature of clouds needs to be investigated, which might lead to different algorithms for different cloud types.

Acknowledgements

We give special thanks to J.P. Veefkind for drawing our attention to the possible use of O_2-O_2 absorption for cloud pressure retrieval. We are grateful to P. Stammes for his help while writing this ATBD and his comments on an earlier version of this ATBD. In addition, we thank R.B.A. Koelemeijer for providing us the FRESCO and ATSR-2 results shown in Fig. 2.5, and the corresponding GOME spectra. The DAK radiative transfer code has been made available to us by P. Stammes (KNMI). Finally, we are grateful to members of the OMI team, for many valuable discussions about the effect of clouds on their algorithms.

2.8. References

Anderson, G. P., S. A. Clough, F. X. Kneizys, J. H. Chetwynd, andE. P. Shettle, 1986, AFGL Atmospheric Constituent Profiles, Tech. Rep.AFGL-TR-86-0110, Air Force Geophysics Laboratory, Hanscom AFB, MA.

Blickensderfer, R.P., Ewing, G.E., 1969, Collision Induced Absorption Spectrum of Gaseous Oxygen at Low Temperatures and Pressures. II, J. of Chemical Physics, 51, 5284-5290

Chandrasekhar, S., 1960, Radiative Transfer, Dover Publications, New York

Chambers, L.H., Wielicki, B.A., Evans, K.F., 1997, Accuracy of the Independent Pixel Approximation for Satellite Estimates of Oceanic Boundary Layer Cloud Optical Depth, J. Geophys. Res., 102, 1779-1794.

Deschamps, P.Y., Fouquart, Y., Tanré, D., Herman, M., Lenoble, J., Buriez, J.C., Dubuisson, P., Parol, F., Vanbauce, C., 1994, Study on the Effects of Scattering on the Monitoring of Atmospheric Constituents, ESA report 3838, ESA contract number 9740/91/NL/BI., Laboratoire d'Optique Atmospheriqué, Université de Lille-1, France

De Haan, J.F., Bosma, P.B., Hovenier, J.W., 1987, The Adding Method for Multiple Scattering Calculations of Polarized Light, Astron. & Astrophys., 183, 371-393

De Rooij, W.A., Van der Stap, C.C.A.H., 1984, Expansion of Mie Scattering Matrices in Generalized Spherical Functions, Astron. & Astrophys, 131, 237-248

Greenblatt, G.D., Orlando, J.J., Burkholder, J.B., Ravishankara, A.R., 1990, Absorption Measurements of Oxygen between 330 and 140 nm, J. Geophys. Res., 95, 18577-18582

Koelemeijer, R.B.A., Stammes, P., 1999, Effects of Clouds on Ozone Column Retrieval from GOME UV Measurements, J. Geophys. Res., 104, 8281-8294.

Koelemeijer, R.B.A., Stammes, P., Hovenier, J.W., de Haan, J.F., 2001, A Fast Method for Retrieval of Cloud Parameters using Oxygen A Band Measurements from the Global Ozone Monitoring Experiment, J. Geophys. Res., 106, 3475-3490

Long, C.A., Ewing, G.E., 1973, Spectroscopic Investigation of van der Waals molecules. I. The Infrared and Visible Spectra of $(O_2)_2$, J. of Chemical Physics, 58, 4824-4834

Naus, H., Ubachs, W., 1999, The $b^1\Sigma^+_g$ — $X^3\Sigma^-_g$ (3,0) Band of $^{16}O_2$ and $^{18}O_2$, J. Molecular Spectroscopy, 193, 442-445

Newnham, D.A., Ballard, J., 1998, Visible Absorption Cross-Sections and Integrated Absorption Intensities of Molecular Oxygen (O_2 and O_4), J. Geophys. Res., 103, 28801-28816

Press, W.H., Teukolsky, S.A., Vetterling, W.T., Flannery, B.P., 1992, Numerical Recipes, 2nd edition, Cambridge University Press.

Stammes, P., de Haan, J.F., Hovenier, J.W., 1989, The Polarized Internal Radiation Field of a Planetary Atmosphere, Astron. Astrophys., 225, 239-259

Stammes, P., 2001, Spectral Radiance Modeling in the UV-Visible Range, IRS2000: Current Problems in Atmospheric Radiation, eds. W.L. Smith, Y.M. Timofeyev, A. Deepak Publ., Hampton (VA), pp. 385-388

Vigasin, A.A., 2000, Collision Induced Absorption in the Region of the O_2 Fundamental: Bandshapes and Dimeric Features, J. Molecular Spectroscopy, 202, 59-66.

3. Retrieval of Cloud Pressure from Rotational Raman Scattering

J. Joiner, NASA/GSFC
A. Vasilkov, SSAI
D. Flittner, Univ. Arizona
E. Buscela, SSAI
J. Gleason, NASA/GSFC

3.1. Introduction

This section of the ATBD focuses on the algorithm to retrieve cloud pressure (CP) from OMI radiances using UV wavelengths. There are two mechanisms that provide radiance sensitivity to CP at these wavelengths: 1) filling-in of solar Fraunhofer lines from rotational Raman scattering (RRS), 2) absorption from O_2-O_2. The output product, Cloud Pressure in hPa, is retrieved from fitting the high-frequency structure of the observed top-of-atmosphere (TOA) radiances with pre-calculated Raman scattering and O_2-O_2 absorption in the spectral range between 355 and 400 nm. The independent sub-pixel approximation is assumed with the effective cloud fraction retrieved from the TOA reflectances in the 355-400 nm range and *a priori* reflectivities of clear and cloudy sub-pixels.

The filling-in of solar Fraunhofer lines, also known as the Ring effect, has been observed previously in ground-based observations [*Grainger and Ring*, 1962] and will affect radiances throughout the OMI spectrum. Pure rotational-Raman scattering (RRS) has emerged as the best explanation for the Ring effect [*Wallace*, 1972; *Brinkman*, 1968; *Aben* et al., 2001]. *Kattawar et al*. [1981] gave a comprehensive survey of inelastic scattering, including both rotational-Raman scattering and Brillouin scattering. An empirical approach has also been used to characterize the Ring effect at visible wavelengths by making use of ground-based observations in parallel and perpendicular polarizations [*Solomon et al*., 1987].

Accurate models for RRS have been developed and have compared well with observations from TOMS, SBUV, GOME, and ground-based measurements [*Joiner et al*., 1995; *Fish and Jones*, 1995; *Chance and Spurr*, 1997; *Vountas et al*., 1998; *Sioris and Evans*, 1999; *de Beek et al*., 2001; *Aben et al*., 2001]. The RRS magnitude scales approximately with the average number of times observed photons are Rayleigh scattered. Therefore the magnitude of the RRS effect, which acts to fill in or deplete solar Fraunhofer lines, depends on the properties of cloud and aerosol, both of which in general reduce (or in some cases enhance) Rayleigh scattering.

Similarly, ultraviolet (UV) absorption due to O_2-O_2 is affected by cloud and aerosol. Therefore, it can also be used to retrieve CP. The two absorption lines considered here are centered at 360 and 380 nm.

3.2. Forward Model

3.2.1. Rotational-Raman scattering

The forward model used in the RRS cloud algorithm is based on *Joiner et al*. [1995] and for brevity will not be reviewed here. The main difference in computing line strengths and frequency shifts here is the inclusion of D_0, the centrifugal distortion constant, which provides more accurate values (D_0=5.76e-6 for N_2 and D_0=4.852e-6 for O_2 from a summary in *Penney et al*., 1974). As in *Joiner et al*. [1995], we treat O_2 as a simple linear molecule, which should be

sufficiently accurate at OMI spectral resolution [*Sioris*, 2001]. Figure 3.1 shows normalized rotational-Raman line strengths at 390 nm and at an atmospheric temperature of 273 K.

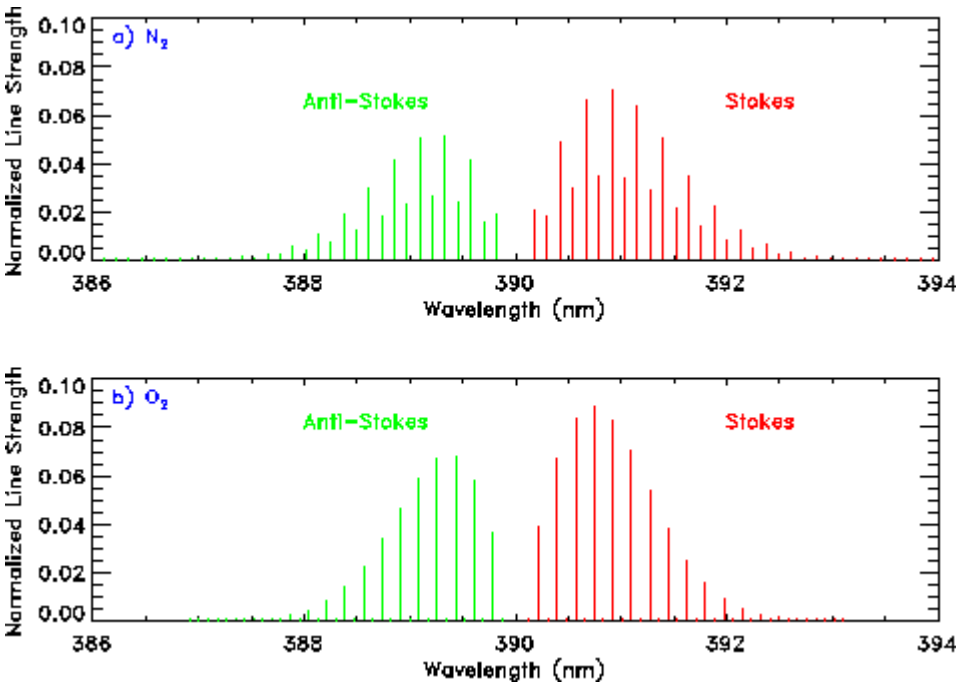

Figure 3.1 Normalized (sum over all lines = 1) rotational-Raman line strengths at 390 nm and T=273K for a) N_2 and b) O_2.

3.2.2. TOMRAD radiative transfer model

The normalized (by the incoming solar irradiance) backscattered intensity I_R observed at the top of the atmosphere can be expressed by

$$I_R = I_R\,(R=0) + R\,I_g\;\; g\,/\,(1 - R\,S_b), \qquad [\,3\text{-}1\,]$$

where R is the surface reflectivity, I_g is the total radiance reaching the surface, g is the transmittance of the radiance reflected from the surface, and S_b is the component of the reflected surface radiance that is scattered by the atmosphere back to the surface. Both I_g and g can be separated into direct and diffuse components. The fraction of each of the above components at every iteration of scattering can be computed with a radiative transfer algorithm.

The forward model used here to compute iteration tables is commonly referred to as TOMRAD, which is an offspring (several generations removed) of work done originally by *Dave* [1964]. TOMRAD computes the source function at various vertical grid points in a vertically inhomogeneous atmosphere with molecular scattering and gaseous absorption using the straight-forward successive orders of scattering method. Polarization of the scattered light is modeled using a modification of the classic Rayleigh scattering phase matrix due to molecular anisotropy and Raman scattering [*Ahmad and Bhartia*, 1995]. The King correction factors computed by *Bates* [1984] are used to correct the Rayleigh (molecular) phase matrix. The lower reflecting surface is diffuse and follows Lambert's cosine law.

While Dave's original work was done for a plane-parallel atmosphere, TOMRAD has two modifications for a spherical atmosphere. First, the direct solar beam is attenuated in a spherical atmosphere to the computational zenith. After this, the source function for each scattering event is computed in a plane-parallel atmosphere. Secondly, the reflected intensity is calculated using the above computed source function in the integration of the source function method

[*Kourganoff*, 1963] for a spherical atmosphere. Basically, for each satellite view angle plane-parallel source functions (with the spherical correction of the solar beam) are attenuated out of the atmosphere to the top of the atmosphere using scattering path lengths that are correct for a spherical atmosphere. These two corrections have been compared to results with a fully spherical model and have errors less than 0.1% for all view angles in plane 90^0 in azimuth to the solar plane and the nadir direction [*Caudill et al.*, 1997]. Larger errors on the order of 10% can occur for q in the solar plane at q_0 of ~88^0. Further details about TOMRAD can be found in the user's guide ("What You Need to Know to Run TOMRAD" by *Celarier and Flittner*, [2001]) that is available with the fortran source code from Code 916, NASA Goddard Space Flight Center, Greenbelt, MD.

In order to quantify the RRS effect on radiance, we use the definition of the filling-in factor, *k*, from *Joiner et al.* [1995]:

$$k(l) = [I_m(l) - I_R(l)] / I_R(l), \qquad [3\text{-}2]$$

where $I_m(l)$ is the measured radiance (including both elastic and inelastic scattering) at effective wavelength l, and $I_R(l)$ is the radiance calculated using Rayleigh scattering only (no RRS) convolved with the instrument bandpass.

Figure 3.2 shows an example of RRS model calculations using TOMRAD. This figure illustrates the RRS dependence on CP at the Calcium K Fraunhofer line near 393 nm and at OMI spectral resolution. This dependence is nearly linear for pressures greater than 0.4 atm.

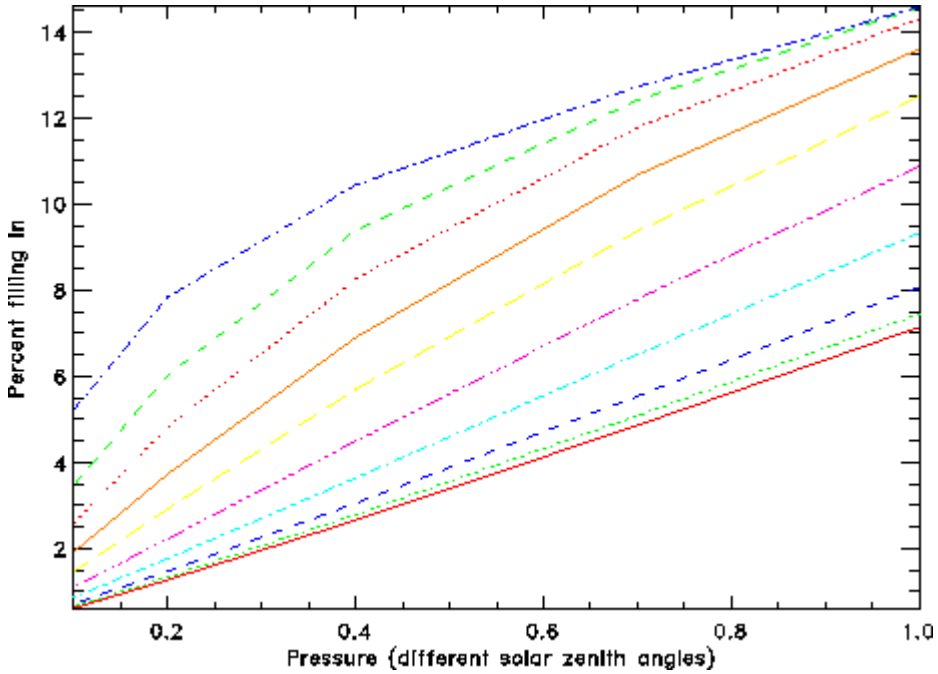

Figure 3.2 Surface pressure (in atm) dependence of the RRS filling-in at R=65%, q=15°, f=0°, and q_o=0, 30, 45, 60, 70, 77, 81, 84, 86, and 88° (bottom curve is 0°) at the Ca K line.

3.2.3. O_2-O_2 absorption in the ultraviolet

There are two relatively weak absorption lines of O_2-O_2 in the 350-400 nm wavelength range (360.4 nm and 380.2 nm). To compute the reflectance spectrum with O_2-O_2 absorption, the input profile of the average temperature in 11 pressure layers is first used, along with the ideal gas law and hydrostatics, to calculate the altitude of the 11 pressure layers. After this the 11 pressures and altitudes are used to interpolate to about 100 levels. These interpolated values are

then used to construct the profile of integrated O_2-O_2 amount from the top of the atmosphere to a level. The O_2-O_2 absorption cross sections are taken from *Greenblatt* [1990] and used with the column O_2-O_2 profile to compute the O_2-O_2 optical depth in each layer of the vertical computational grid used in TOMRAD.

Figure 3.3 shows the fractional change in radiance due to O_2-O_2 lines at different surface pressures. Figure 3.4 shows the dependence on surface pressure for several different solar zenith angles. Because of the pressure-squared dependence of the absorption, these curves are less linear than those of RRS. They also approach zero (or the instrument noise floor) at lower pressures than RRS. Therefore RRS is expected to provide a better mechanism for CP retrieval than O_2-O_2 for high cloud.

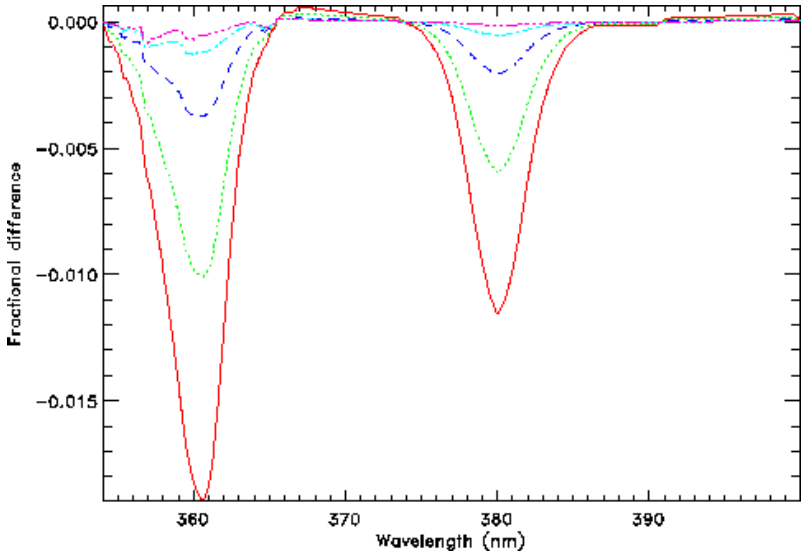

Figure 3.3 Fractional change in radiance due to O_2-O_2 absorption at surface pressures 1013 (solid), 709 (dotted), 405 (dashed), 203 (etc.), and 101 hPa.

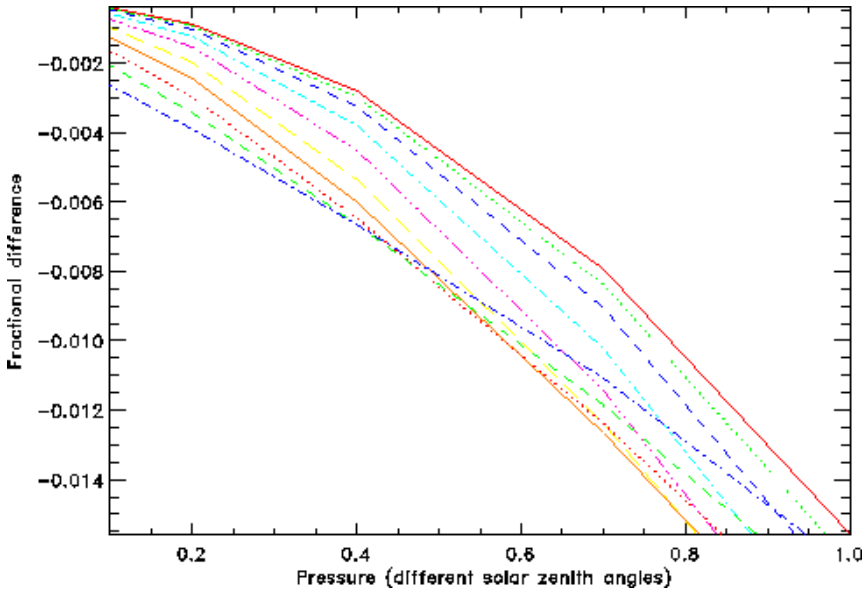

Figure 3.4 Fractional change in radiance due to O_2-O_2 absorption versus pressure at R=65%, q=15°, f=0°, and q_o=0 to 88° (rightmost curve is q_o=0°).

3.2.4. Partial and thin cloud

The primary method used to model the effects of partial or thin cloud within an OMI pixel will be called the modified Lambert-equivalent reflectivity approach or MLER. It combines the independent sub-pixel approximation (IPA) with the assumption of clouds acting as Lambertian surfaces with a given effective reflectivity (LER). A secondary approach, called the thin cloud approximation (TCA) is also being explored. If there is sufficient interest, a second product may be produced using the TCA approach. Other OMI algorithms may be more consistent with one or the other method. As of the writing of this document, most are consistent with the MLER approach.

For the MLER approach, it is assumed that an OMI pixel is covered by a cloud fraction *f*. Then the radiance from that pixel is given by

$$I_{tot} = I_1 \, (1 + k_1) \, (1 - f) + I_2 \, (1 + k_2) \, f, \qquad [3\text{-}3]$$

where I_{tot} is the measured TOA radiance, I_1 and I_2 are the pre-calculated clear sky and cloud radiances respectively, f is the effective cloud fraction, k_1 and k_2 are the filling-in factors, k_1 being computed using look up tables. The effective cloud fraction is defined from measurements at wavelengths not significantly affected by absorption and RRS. To calculate the clear sky and cloud radiances, values of the *a priori* surface reflectivities, R^{cloud} and R^{clear}, are needed. In the TOMS V8 algorithm, R^{cloud}=0.8 and R^{clear}=0.15 and these were assumed invariant. These are the values that will be used in the OMI UV cloud algorithm. The filling-in factor, k_2, containing the information about cloud pressure, is determined from the above equation. Cloud pressure is retrieved from the filling-in factor, k_2, by using lookup tables as discussed below.

The TCA involves the treatment of clouds as a semi-opaque surface that takes into account the radiance contribution of underlying layers. Full Mie-scattering calculations in a cloudy atmosphere in the O_2-O_2 bands have been performed using the University of Arizona Gauss-Seidel iteration code. In the model, clouds are assumed to be horizontally and vertically uniform. A cloud model C1 having the modified gamma size-distribution of water droplets was used [*Deirmendijan*, 1969]. Simulations were carried out for three cloud scenarios defined by the physical cloud-top pressure P_c=300, 500, and 700 hPa. Geometrical thickness of the clouds was defined by a constant pressure difference of 200 hPa between the top and bottom cloud pressures. The simulations included aerosol scattering. A maritime aerosol model was assumed with the aerosol optical thickness of 0.15 at 550 nm. Surface albedo was equal to 0.05. RRS was not included in the calculations.

Figures 3.5 shows O_2-O_2 absorption line depth versus the physical cloud top pressure for clouds with different optical depths at 360 nm. Note that the O_2-O_2 absorption dependence on cloud optical depth (τ) saturates at about 25. An interesting effect at the 360 nm line is the response for the lowest cloud. It can be seen that there is enhanced absorption for the thick cloud as compared with the thin cloud or no cloud. Radiative transfer calculations show that this is the result of a higher cloud reflectivity that increases photon path length between the cloud and Rayleigh-scattering and O_2-O_2 absorbing atmosphere above.

Radiative transfer models of RRS in the thin cloud approximation have been developed at the University of Arizona (UA) and by Robert Spurr (private communication, 2002). Results from the UA model compared well with those of *de Beek et al.* [2001] and will be used below to interpret the meaning of LER pressure.

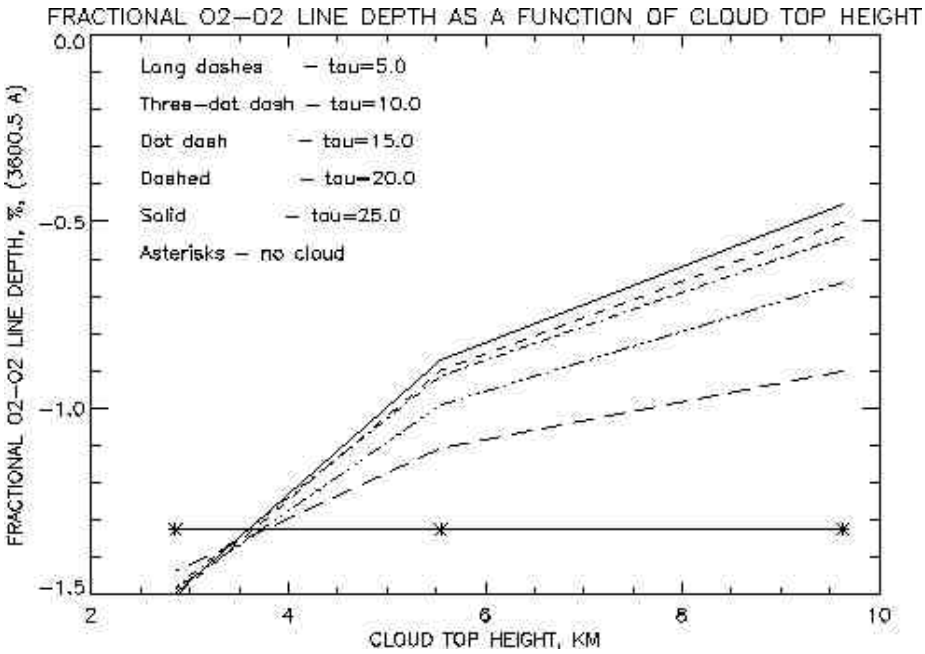

Figure 3.5 O2-O2 absorption cloud-top height and cloud optical depth dependence at 360 nm, qo=45o, nadir, R=5%.

3.2.5. Ocean Raman scattering (ORS) effects

Vibrational Raman scattering has been observed and modeled in the ocean [*Marshall and Smith*, 1990; *Sathyendranath and Platt*, 1998]. This effect causes filling-in of solar Fraunhofer lines [*Kattawar and Xu*, 1992]. When the observed filling-in at the Ca K line is divided by the computed atmospheric component, residual filling-in is observed over ocean as shown in Figure 3.6 for SBUV. The ocean filling-in effect has also been observed with GOME data.

The amount of excess filling-in introduced by ocean Raman scattering (ORS) under cloudy conditions (*i.e.* $f > 0$, $R > R^{clear}$) can be approximated by $k_{exc} = (1-R)^2 k_{oc,}$ where R is the derived reflectivity, k_{oc} is the excess filling-in from the ocean Raman scattering in clear conditions as shown in Figure 3.6. At SBUV resolution and near 393 nm, the maximum value of k_{oc} is about 40%. For R = 60%, typical of full cloud cover, this gives k_{exc} = 6%. For a less opaque cloud with R = 40%, k_{exc} = 14%. Alternatively, an IPA method may be used where a cloud fraction f is defined. Then, we can assume the ORS from the cloudy part of the scene to be negligible and approximate ORS as $k_{exc} = (1-f)\, k_{oc.}$

Vasilkov et al. (2002) have developed a model to compute k_{oc}. In this model, the magnitude of ORS for a given viewing geometry is computed as a function of chlorophyll content. Figure 3.7 shows the spectral dependence of ORS. Although there is some correlation with RRS, the magnitude ORS decreases with wavelength (unlike of RRS), because the radiance reaching the ocean surface from the excitation wavelength (~3400 cm^{-1} to the blue) decreases due to ozone absorption. The model explained the difference in excess filling-in in GOME observations at the Ca K line for clear and turbid conditions (*Vasilkov et al,*. 2002).

As it is seen from Figure 3.7, the magnitude of the filling-in factor due to ORS depends on chlorophyll concentration significantly. In clear waters with low chlorophyll concentrations, the filling-in factor is substantially higher than in turbid waters with high chlorophyll concentrations.

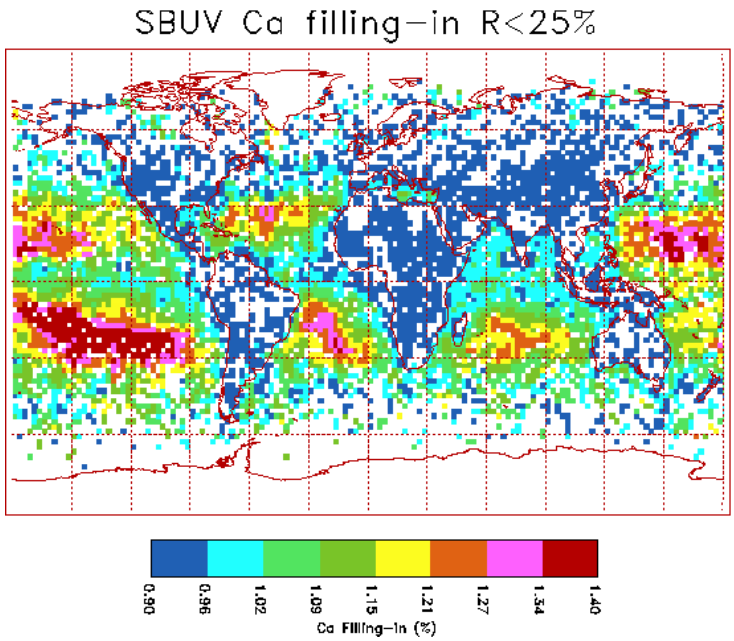

Figure 3.6 Excess Raman scattering for scenes with R < 25% from SBUV continuous scan data from 1978-1986.

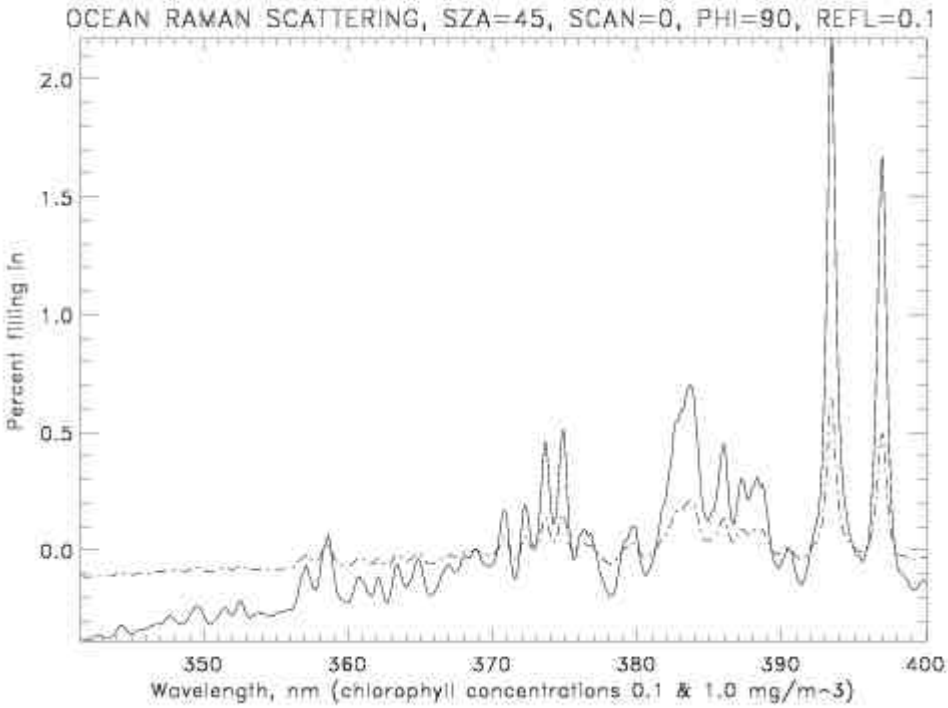

Figure 3.7 Spectral dependence of ORS computed for 2 chlorophyll concentrations

3.3. Inverse Model

The general approach for retrieving the CP is a fast linear least-squares algorithm based on table lookup. We next outline some of the algorithmic details.

3.3.1. Table generation

Tables of the iteration values output from the TOMRAD code were generated for wavelengths between 340 and 400 nm for a single O_3 profile (O_3 absorption is very weak in this spectral range) for 5 difference surface pressures (P = 1.0, 0.7, 0.4, 0.2, and 0.1 atm.), 10 solar zenith angles (q_o=0, 30, 45, 60, 70, 77, 81, 84, 86, 88^o), 6 satellite zenith angles (q =0, 15, 30, 45, 60, 70^o), and 7 azimuth angles (ϕ=0, 30, 60, 90, 120, 150, 180^o). Using a solar spectrum, a second set of tables of the RRS filling-in and normalized radiance has been generated at OMI spectral resolution at 6 reflectances (R=1, 10, 20, 40, 65, 95%).

For algorithm development and testing, the second set of tables were generated for several solar spectra: 1) a solar spectrum from *Kurucz et al*. [1994] convolved with a triangular slit having a full-width half maximum of 0.63 nm, 2) an observed GOME solar spectrum for used with GOME data at its original spectral resolution, 3) a GOME solar spectrum convolved with an OMI response function (J.P. Veefkind, private communication) for use with a GOME test data set made to simulate OMI data. *Joiner et al*. [1995] pointed out that more accurate results would be obtained using a solar spectrum from OMI when it becomes available. Therefore, the tables will be regenerated post-launch using a measured OMI solar spectrum and will be recomputed as necessary to account for changes in the instrument and/or solar spectrum.

3.3.2. Reflectivity, cloud fraction, Aerosol Index, and cloud optical depth calculation

The reflectivity and effective cloud fraction will be calculated at two wavelengths chosen such that they are relatively free of RRS and O_2-O_2 absorption by inversions of (3.1) and (3.3). For testing with GOME, these are 346.8 and 373.2 nm, but for OMI this choice will depend on the wavelengths available in the VIS channel.

An aerosol index, *AI*, will be computed using the same wavelengths. *AI* will be used to flag absorbing aerosol-contaminated pixels.

The effective cloud fraction is determined by inversion of (3.3). This calculation assumes that the filling-in factors at these wavelengths are negligible. The inversion is performed with *a priori* values for clear and cloudy reflectivities as described above for the MLER.

For a given geometry, the effective cloud optical depth, t, can be determined from TOA reflectance using the TCA approach. The cloud TOA reflectance dependence on cloud height is very weak, therefore, t can be retrieved from a pre-calculated lookup table of TOA reflectance, surface albedo, and geometry. The Earth's surface albedo is needed to create the lookup table and can be obtained from climatological datasets. The climatological data is reasonable because of the relatively small effects of the surface reflectance in a cloudy atmosphere. However, the surface plays a strong role in the presence of snow, ice, and sun-glint. Therefore, under these conditions, cloud fraction and optical depth will be flagged as questionable.

3.3.3. Cloud pressure retrieval by least-squares fitting

The cloud pressure is retrieved by an iterative minimum-variance (least-squares) solution of the form

$$x_{n+1} = x_n + (H' (O+F)^{-1} H)^{-1} (O+F)' R^{-1} (y_{obs} - y_{calc}), \qquad [3\text{-}4]$$

where x_n is state vector estimate at iteration n (the algorithm typically converges in 3-4 iterations), H is the Jacobian matrix (partial derivatives of the observation vector with respect to the state vector), O and F are the observation and forward model error covariance matrices, respectively, and y_{obs} and y_{calc} are vectors of observed and calculated radiances, respectively.

The observation vector will include normalized radiances from 365-400 nm (note: 365 nm is the nominal shortest wavelength of the OMI VIS channel). If shorter wavelengths are usable in this channel, they will be incorporated into the algorithm. This implicitly includes wavelengths affected by RRS and O_2-O_2. The observations are spline-interpolated to the table wavelengths which greatly reduces the amount of computation required for interpolation. The total $O + F$ will be a diagonal matrix with errors that will be adjusted. Currently, for testing with GOME data, the square root of the diagonal (estimated standard deviation) is conservatively set to 1% of the observed value.

The state vector includes three coefficients to form a quadratic fit of the low-frequency component of the radiances (*i.e.*, $A + B\ l + C\ l^2$), two coefficients to correct for wavelength differences between the solar irradiance and earth-view spectra (shift and squeeze), and the cloud pressure. It is the wavelength shift and squeeze that contributes most to non-linearity and necessitates an iterative solution. The spectral shift and squeeze may not be needed for OMI because it is expected to have better spectral calibration than GOME. However, the spectral shift and squeeze are essential for GOME. Over ocean or large lakes, chlorophyll content can be added to the state vector. The quadratic coefficients account for Rayleigh scattering as well as calibration errors so that the cloud pressure is determined only from the high-frequency component of the spectra. Figure 3.8 shows the RRS filling-in factor at OMI (VIS channel) resolution.

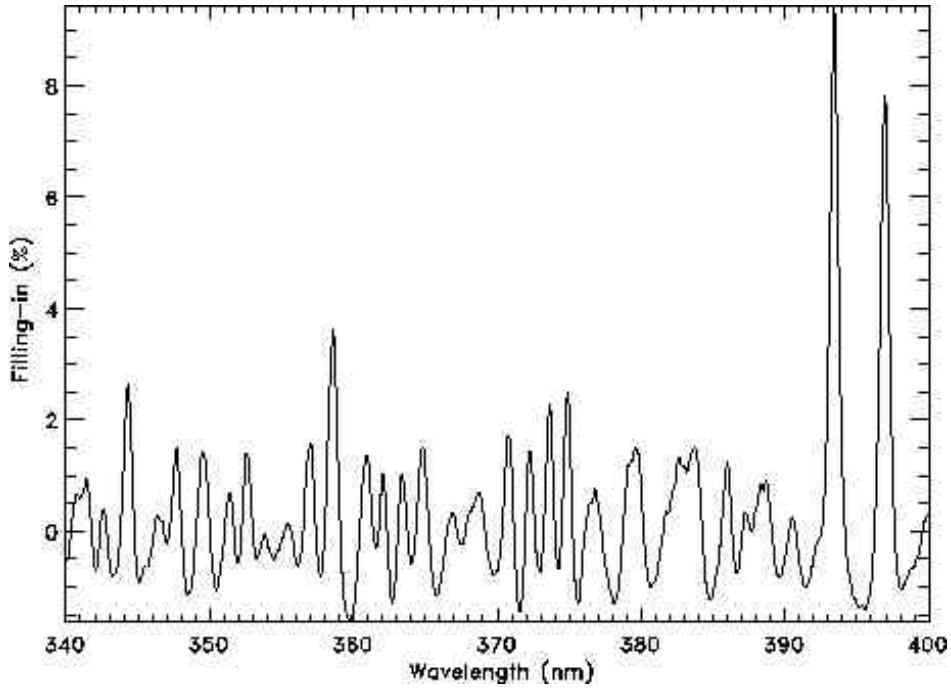

Figure 3.8 Computed filling-in at OMI resolution at q_o=60^o and R=65%.

The radiances y_{calc} are computed by linear interpolation in R, P, q_o, q, and ϕ. Under clear or overcast conditions, calculations are performed using the retrieved reflectivity. In partial cloud, calculations are performed at the *a priori* clear and cloudy values of reflectivity. The

pressure, chlorophyll, and wavelength shift and squeeze Jacobians are computed by finite differences.

At every iteration, a quantity χ , defined as

$$c=[y_{resid}\,(O+F)^{-1}\,y_{resid}]^{1/2}/N \qquad [\,3\text{-}5\,]$$

is computed, where N is the number of wavelengths, and y_{resid}, called the radiance residual, is defined as $y_{resid}=y_{obs}-y_{calc}$. Iterations continue until $(\chi_{n-1}-\chi_{n})/\chi_{n-1}<0.03$. If convergence is not reached in 6 iterations or the value of χ begins to increase, the retrieval is flagged as unsuccessful.

3.3.4. *A priori* information

For the calculation of *f*, *AI*, and *t*, a climatological map of surface pressure is used. However, the radiances have little dependence on surface pressure. A climatological map of surface albedo is needed for the computation of *t*. The same database can be used for the determination of *f*. Constant values of R^{clear} and R^{cloud} can also be used for the determination of *f* as in the TOMS V7 algorithm [*McPeters et al.*, 1996] and as described above and these will be used initially.

3.3.5. ORS adjustments

Several methods of minimizing the effects of ORS have been implemented and tested by retrieving the surface pressure over clear ocean GOME pixels. One method is to estimate the ocean Raman contribution to the filling-in using a theoretical model. In clear skies, *Vasilkov et al*. [2002] have shown that the ocean Raman filling-in can be modeled in terms of a single parameter, chlorophyll content. Preliminary results with GOME data indicate that chlorophyll content can be determined from OMI observations and this will be an experimental product. Figure 3.9 shows the scene pressures for clear pixels retrieved with and without correction for the ocean Raman contribution. The scene pressures, which should be equal approximately to 1 atm, are significantly overestimated if no correction is performed. Using a global climatology for chlorophyll content with the theoretical model also overestimates the scene pressure. Including chlorophyll content as part of the retrieval state vector significantly improved the retrieval of scene pressure.

3.4. Error Analysis and Interpretation

The retrieval error covariance, *P*, can be computed by linear error analysis, *i.e.* $P=(H'(O+F)^{-1}H)^{-1}$. This formulation assumes that the errors are Gaussian and uncorrelated with respect to each other. Based on the results of Figure 3.11, we estimate the forward model errors to be ~0.5%. We note that if the errors are dominated by a systematic component, this will lead to biased results as opposed to random errors. Also note that the CP error is approximately inversely proportional to the cloud fraction *f* so that as $f \to 0$, CP error$\to\infty$. We find for f = 1.0 (high reflectivity), the CP error is approximately 10 hPa using an estimate of $(O+F)$ which is a diagonal matrix (*i.e.* uncorrelated errors) with the square root of the diagonal elements (*i.e.* standard deviations) set to 0.5%. These results did not vary significantly with cloud pressure or viewing angle. As cloud fraction decreases, the CP error increases, so that at f = 0.1 and 0.05, the CP errors are approximately 40 and 70 hPa, respectively with errors of 0.5%. All other parameters (including wavelength shift and squeeze) are determined with very high accuracy.

Estimated pressure errors for low reflectivities associated with clear pixels were nearly double those estimated for high reflectivity due to decreased sensitivity.

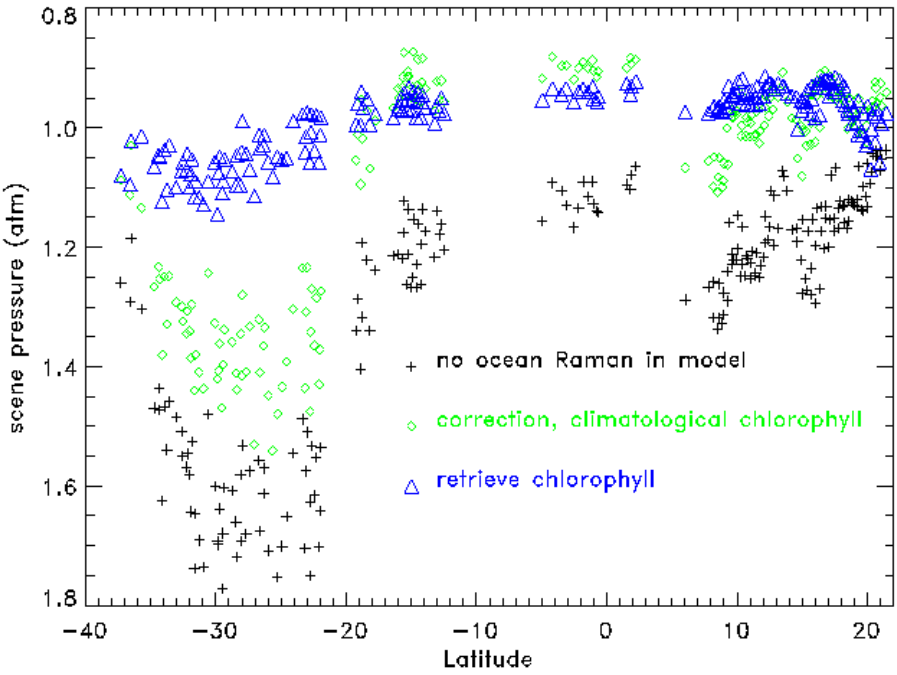

Figure 3.9: Derived scene pressures for different cases: no ocean Raman contribution (black +), ocean Raman correction using climatological chlorophyll concentrations (green diamonds), and ocean Raman correction using the simultaneous retrieval of pressures and chlorophyll concentrations (blue triangles).

The correlation of the error estimates can be determined from *P*. When chlorophyll is not included in the state vector, the errors are not significantly correlated (all error correlations less than 10%). This indicates that given the retrieved cloud fraction, there is a nearly unique solution for cloud pressure. When chlorophyll is added to the state vector assuming a clear scene, the estimated pressure error nearly doubles, but the error is highly correlated with that of chlorophyll, indicating that within the range of estimated uncertainties, there are non-unique pairs of chlorophyll and pressure that could produce the observed radiances.

A fully non-linear simulator was developed in which radiances were simulated from a "truth" and random noise added. The results validated the estimates obtained with the linear analysis.

Joiner et al. [1995] showed that the effect of temperature on the filling-in is very small ($\Delta k/\Delta T \approx 0.0042\%/K$) for nadir-viewing instruments. Therefore, the use of a constant temperature (273 K) in the calculation of the RRS spectra should produce a negligible error.

Simulations were performed with the UA thin cloud RRS model for a 100 hPa thick cloud at several cloud top pressures between 400 and 900 hPa at $\theta_o=55^o$ and for $\tau=0.1$-50. The results showed that the retrieved LER cloud pressure (assuming a cloud fraction of 100%) will be approximately 50-80 hPa higher than the physical cloud top for $\tau>2$. Therefore, the retrieved LER pressure is in the middle to lower portion of the cloud. These simulations are important for interpreting differences between retrieved LER pressure and other types of cloud pressure estimates such as those from thermal IR observations as will be shown in the next section.

3.5. Algorithm validation

The UV CP cloud algorithm has been tested with GOME data using the MLER method. The retrieved CP can be compared with that derived from the GOME oxygen A-band technique and thermal infrared observations from ATSR-2, which flies on the same satellite. Figure 3.10 shows the fit to a single GOME spectrum between 350 and 400 nm. Figure 3.11 shows the radiance residuals averaged over 70 GOME scans (bias) and the standard deviations. For most wavelengths, the bias is less than 0.5%, but larger than the standard deviation which is typically less than 0.2%. There is a feature near 380 nm that is most likely related to errors in the O_2-O_2 absorption calculation such as the temperature dependence of the O_2-O_2 cross-section or a wavelength error in the O_2-O_2 cross-section. Biases are larger short-ward of 355 nm where O_3 absorption begins to become significant. These wavelengths will not be used with OMI.

Figure 3.12 shows a preliminary comparison of derived cloud pressures for GOME orbit 80324174 (March 24, 1998). On this day, GOME was in the small pixel mode so that the ground pixel size was 40 X 80 km. ATSR-2 retrievals of cloud-top pressure were provided by the Rutherford Appleton Laboratory. In this data set, ATSR-2 pixels (1 X 1 km) were collocated with and averaged over the GOME ground pixel. Preliminary retrievals of cloud pressure derived from the GOME O2-A band using the GOMECAT algorithm were provided by T. Kurosu (private communication). The comparison here used pixels in which the ATSR-derived cloud fraction was 100% and the GOME reflectivity was at least 40%. The cloud fraction was assumed to be 100% (i.e. for this comparison R^{cloud} was assumed to be 40%).

Correlation between the UV-retrieved GOME cloud pressures and the IR ATSR is 0.75 and was slightly higher on other orbits. However, there are systematic differences between the methods that will require further analysis. It is important to note that the LER cloud pressure retrieved with RRS and/or O_2-O_2, can be thought of as scattering and/or photon path length approaches. These are fundamentally different from thermal emission algorithms. Scattering approaches are affected by enhanced photon path-lengths inside and below cloud while the thermal IR is not as discussed in the previous section.

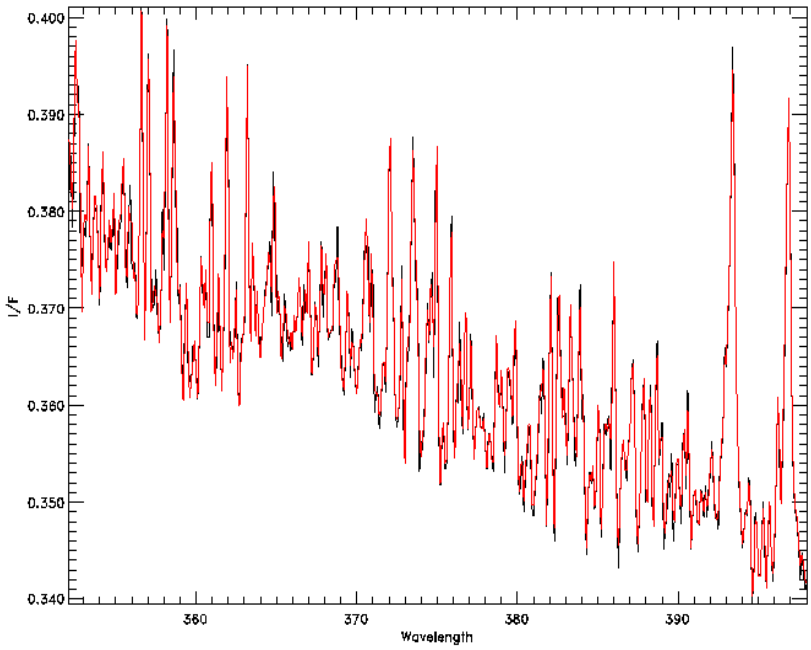

Figure 3.10 Observed (black) and computed (red) normalized radiances for a single GOME pixel after convergence.

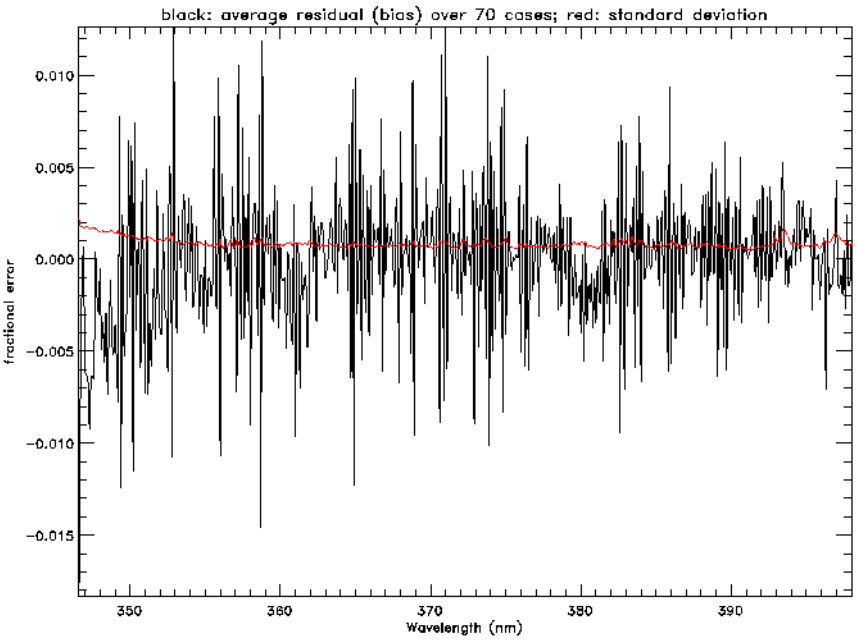

Figure 3.11 Bias (black) and standard deviation (red) of radiance residuals averaged over 70 GOME pixels.

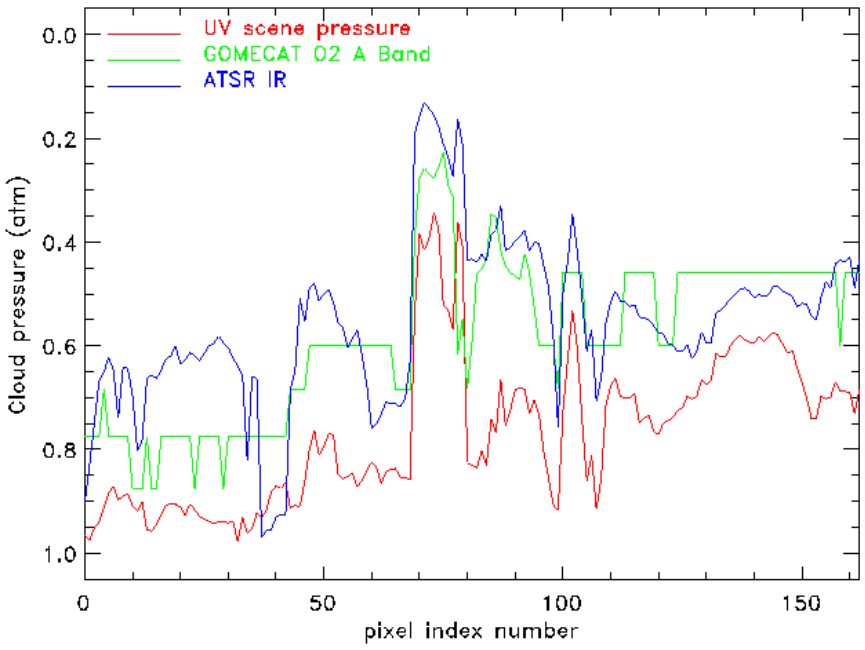

Figure 3.12 Derived cloud pressures from GOME small pixels (profiles) for high-reflectivity (R>40%, f=1.0) using OMI CP algorithm (red), collocated ATSR infrared-derived from RAL, and GOMECAT O_2-A-band (Kurosu, private communication).

As part of the cloud pressure validation, other OMI algorithms will be tested using the UV cloud pressures. The results will be compared with those obtained using cloud pressures from other sources. Specific areas of interest such as the south Atlantic, where persistent marine stratocumulus reside, will be studied. Total ozone derived over these clouds from TOMS has a known bias and correlation with reflectivity [*e.g Thompson et al.,* 1992; *Hsu et al.,* 1997].

Other instruments that will retrieve cloud properties will fly on satellites in formation with EOS Aura such as EOS Aqua (infrared and visible imager MODIS and kilo-channel infrared sounder AIRS), a 94 GHz radar on Cloudsat, and a dual-wavelength lidar and infrared imager on the Cloud-Aerosol Lidar and Infrared Pathfinder Satellite Observations (CALIPSO). Cloud pressures will be compared with available data from these instruments during the commissioning phase. Ultimately it is hoped that different types of measurements (*e.g.* UV and IR) may be combined to give information on cloud structure.

3.6. References

Aben, I., Stam, D. M., and F. Helderman (2001). The Ring effect in skylight polarisation. *Geophys. Res. Lett.*, **28**, 519-522.

Ahmad, Z. and P. K. Bhartia (1995). Effect of molecular anisotropy on the backscattered UV radiance. *Appl. Opt.*, **34**, 8309-8314.

Bates, D. R. (1984). Rayleigh scattering by air. *Planet. Space Sci.*, **32**, 785-790.

de Beek R., Vountas, M., Rozanov, V. V., Richter, A., and J. P. Burrows (2001). The Ring Effect in the cloudy atmosphere. *Geophys. Res. Lett.*, **28**, 721-724.

Brinkman, R. T. (1968). Rotational Raman scattering in planetary atmospheres. *Astrophys. J.*, **154**, 1087-1093.

Caudill, T. R., Flittner, D. E., Herman, B. M., Torres, O., and R. D. McPeters (1997). Evaluation of the pseudo-spherical approximation for backscattered ultraviolet radiances and ozone retrieval. *J. Geophys. Res.*, **102,** 3881-3890.

Chance, K. V. and R. D. Spurr (1997). Ring effect studies: Rayleigh scattering, including molecular parameters for rotational Raman scattering, and the Fraunhofer spectrum. *Appl. Opt.*, **36**, 5224-5230.

Dave, J. V., (1964). Meaning of successive iteration of the auxiliary equation in the theory of radiative transfer. *Astrophys. J.*, **140**, 1292-1303.

Deirmendjian, D. (1969). Electromagnetic scattering on spherical polydispersions. American Elsevier Pub. Co., N. Y., N. Y., USA, 290 pp.

Fish, D. J., and R. L. Jones (1995). Rotational Raman scattering and the Ring effect in zenith-sky spectra. *Geophys. Res. Lett.*, **22**, 811-814.

Grainger, J. F., and J. Ring (1962). Anomalous Fraunhofer line profiles. *Nature*, **193**, 762.

Greenblatt, G. D., Orlando, J. J., Burkholder, J. B., and A. R. Ravishankara (1990). Absorption measurements of oxygen between 330 and 1140 nm. *J. Geophys. Res.*, **95**, 18577-18582.

Hsu N. C., McPeters R. D., Seftor C. J., Thompson A. M. (1997). Effect of an improved cloud climatology on the total ozone mapping spectrometer total ozone retrieval. *J. Geophys. Res.*, **103**, 4247-4255.

Joiner J., Bhartia, P. K., Cebula, R. P., Hilsenrath, E., and R. D. McPeters (1995). Rotational-Raman Scattering (Ring Effect) in Satellite Backscatter Ultraviolet Measurements. *Appl. Opt.*, **34**, 4513-4525.

Joiner J., and P. K. Bhartia (1995). The Determination of Cloud Pressures from Rotational-Raman Scattering in Satellite Backscatter Ultraviolet Measurements. *J. Geophys. Res.*, **100**, 23019-23026.

Kattawar, G. W., Young, A. T., and T. J. Humphreys (1981). Inelastic scattering in planetary atmospheres. I. The Ring effect, without aerosols. *Astrophys. J.*, **243**, 1049-1057 .

Kattawar, G. W., and X. Xu (1992). Filling in of Fraunhofer lines in the ocean by Raman scattering. *Appl. Opt.*, **31**, 6491-6500.

Kourganoff, V. (1963). Basic methods in transfer problems. Dover Publications, Inc. New York, 281 pp.

Kurucz, R. L., Furenlid, I., Brault, J., and L. Testerman (1984). Solar flux atlas from 296 to 1300 nm. National Solar Observatory, Sunspot, New Mexico, 240 pp.

Marshall, B. R., and R. C. Smith (1990). Raman scattering and in-water ocean optical properties. *Appl. Opt.*, **29**, 71-84.

McPeters, R. D., Krueger, A. J., Bhartia, P. K., Herman, J. R., Oaks, A., Ahmad, Z., Cebula, R. P., Schlesinger, B. M., Swissler, T., Taylor, S., Torres, O., and C. G. Wellemeyer, Nimbus-7 total ozone mapping spectrometer (TOMS) data products user's guide, *NASA Ref. Publ., 1384*, 1996.

Penney, C. M., St. Peters, R. L., and M. Lapp (1974). Absolute rotational Raman cross sections for N_2, O_2, and CO_2, *J. Optic. Soc. Amer.*, **64**, 712-716.

Sathyendranath S., and T. Platt (1998). Ocean-color model incorporating transspectral processes. *Appl. Opt.*, **37**, 2216-2227.

Sioris, C. E. (2001). Filling in of absorption lines in sky spectra due to rotational Raman scattering. PhD Thesis. York University, Canada, 133pp.

Sioris, C. E., and W. F. J. Evans (1999). Filling in of Fraunhofer and gas-absorption lines in sky spectra as caused by rotational Raman scattering. *Appl. Opt.*, **38**, 2706-2713.

Solomon, S., Schmeltekopf, A. L., and R. W. Sanders (1987). On the interpretation of zenith sky absorption measurements. *J. Geophys. Res.*, **92**, 8311-8319. mn

Thompson, A. M., McNamara, D. P., Pickering, K. E., and R. D. McPeters (1993). Effect of marine stratocumulus

Vasilkov, A. P., Joiner, J., Gleason, J. F., and P. K. Bhartia (2002). Ocean Raman scattering in satellite backscatter ultraviolet measurements. *Geophys. Res. Lett.*, in press.

Vountas M., Rozanov V. V., J. P. Burrows (1998). Ring effect: Impact of rotational Raman scattering on radiative transfer in Earth's atmosphere. *J. Quant. Spect. Rad. Trans.*, **60**, 943-961.

Young A. T., (1981). Rayleigh scattering. *Appl. Opt.*, **20**, 533-535.

Wallace, L., (1972). Rayleigh and Raman scattering by H_2 in a planetary atmosphere. *Astrophys. J.*, **176**, 249-257.

4. OMI Aerosol Retrieval Algorithm

Omar Torres[1], Rob Decae[2], Pepijn Veefkind[3], Gerrit de Leeuw[2]
[1]NASA GSFC/ University of Maryland, Baltimore County, Baltimore, USA
[2]TNO, Physics and Electronics Laboratory, The Hague, The Netherlands
[3]Royal Netherlands Meteorological Institute (KNMI), De Bilt, The Netherlands

4.1. Introduction

Tropospheric aerosols influence the Earth's climate in many ways. The direct cooling effect of aerosols on climate, by scattering a fraction of the incoming solar radiation back to space, is relatively well understood. Cooling by scattering or local heating by aerosol absorption of short and long wave radiation can produce changes in net heating rates that may in turn produce changes in atmospheric circulation. In addition, aerosols can indirectly affect climate through their action as cloud condensation nuclei (CCN). Aerosols are also important for non-climate-related phenomena, such as local, regional, and global air pollution; the attenuation of UV-B and UV-A radiation reaching the Earth's surface; tropospheric chemistry; and remote sensing of other geophysical parameters.

Aerosols on regional to global scales can be determined using satellite based instruments such as the Ozone Monitoring Instrument (OMI). The algorithm developed for detection and characterization of aerosols over land and water using OMI is described in this chapter. It takes full advantage of the hyper-spectral OMI measurements to differentiate between aerosol types and quantify its physical properties in terms of total aerosol optical thickness and single scattering albedo. The OMI aerosol algorithm was developed in fulfillment of the EOS-Aura mission objectives as established in the Science Requirements Document for OMI-EOS [*Levelt et al.*, 2000]. The required accuracy for aerosol optical thickness over the oceans is the largest of 30% or 0.1 at 400 nm, which corresponds to 30 % or 0.08 in the mid-visible. Single scattering albedo will be available as a research product, and its accuracy will be assessed by comparisons with results from independent measurements. Aerosol properties will be derived over cloud free areas on a daily basis worldwide at a spatial resolution of 13×24 km^2. In the OMI algorithm aerosol retrievals are carried out using two approaches: a multi-wavelength approach that uses 17 wavelengths in the 331-500 nm range, and a method that uses two wavelengths in the near UV. Experience in the application of the near UV method to the TOMS data [*Torres et al.*, 2002] has proven this method to be a robust retrieval approach. The multi-wavelength method is an extension of the near UV method to a wider wavelength range. Although the two inversion processes will be applied over all surface types, the multi-wavelength approach is the primary retrieval method over the oceans, and the near UV method is the primary retrieval technique over land. The reason for this is that over land the available spectral surface reflectivity databases may not be good enough to apply the multi-wavelength method.

A brief overview and background discussion on the use of satellite observations to monitor aerosols is presented in Section 4.2. The physical basis of the retrieval approach, the choice of wavelengths and the use of radiative transfer calculations are discussed in Section 4.3. Section 4.4 presents a detailed discussion of the inversion method, followed by a description of the required ancillary data to characterize surface and atmospheric properties (i.e., environmental model) that affect the aerosol retrieval process. The results of sensitivity analyses are presented in Section 4.6, and a discussion of validation plans in Section 4.7.

4.2. Overview and background

4.2.1. Historical Perspective

Given sufficient retrieval accuracy, use of satellite observations is the most efficient way to determine tropospheric aerosol physical properties on the temporal and spatial scales needed to understand and monitor their effects on the Earth-atmosphere system (cf. *King et al.* [1999] for a review). Satellite-based observations of back-scattered radiances at the top of the atmosphere have been used to retrieve information on tropospheric aerosol properties for the past twenty years. Measurements at 640 and 840 nm from the Advanced Very High Resolution Radiometer (AVHRR) on board NOAA satellites have been used to retrieve aerosol properties over the ocean [e.g. *Stowe et al.*, 1997; *Mishchenko et al*.,1999; *Nakajima and Higurashi*, 1998; *Veefkind et al.,* 1999]. New retrieval algorithms which enable the retrieval of the aerosol loading as well as information on the size distribution have been applied to instruments with additional and narrower wavelength bands, such as the MODIS (Moderate Resolution Imaging Spectrometer) and MISR (Multi-angle Imaging Spectro-Radiometer) sensors onboard the TERRA spacecraft, and the ATSR-2 (Along Track Scanning Radiometer) on board the European ERS-2 satellite.

Until recently, it was thought that satellite retrieval of aerosols was only feasible over dark surfaces such as oceans, where in the visible and near infrared the reflected radiance is dominated by aerosols. Over land areas, the surface contribution can be significantly larger than the aerosol contribution, which renders the aerosol retrieval difficult. Recently, instrumental and algorithmic innovations to retrieve aerosol properties over land using visible and near infrared observations have been developed. Multi-angle radiometry (a technique that allows the separation of the atmospheric and land contributions to the measured signal), was first applied to ATSR-2 data [*Veefkind et al*., 1998; *Robles-Gonzalez et al.*, 2000] and will be further explored using the MISR instrument [*Diner et al.,* 1998]. Another method to derive aerosol properties over land has been developed for MODIS. This method uses the relationship between the surface albedo in the mid-IR and the visible to separate atmospheric and land contributions [*King et al.*, 1999]. The combination of different viewing angles and measurements of the degree of polarization has also been explored for the retrieval of aerosol properties over land [*Deschamps et al*., 1994] using POLDER observations.

A new method to retrieve aerosol properties over land and water surfaces using measurements in the near UV region of the spectrum (330-380 nm) has been developed in the last few years [*Herman et al.,* 1997, *Torres et al.,* 1998]. The near UV approach was developed using observations from the TOMS (Total Ozone Mapping Spectrometer) series of instruments. The TOMS near UV technique of aerosol retrieval is uniquely sensitive to aerosols that absorb solar radiation in the ultraviolet such as carbonaceous, mineral dust and volcanic ash aerosols. Another significant advantage of this method is the capability to retrieve aerosol properties over all terrestrial surfaces (free of ice and snow) including arid areas which are highly reflective in the visible and near infrared, but have very low reflectivity in the UV. This method has been successfully applied to data from the TOMS instruments on the Nimbus-7 and Earth Probe satellites [*Torres et al*., 2002].

The OMI aerosol algorithm will enhance the advantages of the TOMS aerosol retrieval method. TOMS measurements are limited to a few wavelength bands in the UV, whereas OMI will measure a spectrum that ranges from the UV to the visible (270-500 nm). This will enable us to bridge the gap between aerosol satellite observation in the visible and near-infrared (e.g. MODIS, AVHRR) and those in the UV (TOMS). The improved spectral resolution and wavelength range compared to TOMS will be exploited to better distinguish between various

types of aerosols. The OMI ground pixel size (13×24 km^2) is an improvement over TOMS (40×40 km^2), and is much smaller than that of the other hyper-spectral sensors GOME (Global Ozone Monitoring Experiment) and SCIAMACHY (Scanning Imaging Absorption spectrometer for Atmospheric Cartography), ensuring less cloud contamination and therefore an increased ability to obtain information on tropospheric aerosols.

4.2.2. Product description

The operational OMI aerosol products are the aerosol optical thickness (τ) and single scattering albedo (ω_0). These parameters will be derived by two methods, the multi wavelength method and the near UV method. Although both retrieval techniques will be applied to all ground pixels, the primary retrieval technique over the ocean is the multi-wavelength method, and over land the primary method is the near UV method. The near UV method will produce the aerosol optical thickness and single scattering albedo at 388 nm, the multi wavelength method will produce at selected wavelength between 330 and 500 nm, including 388 nm. The optical thickness and single scattering albedo will be derived for all cloud free Level 1B OMI ground pixels. In the OMI global operational mode the spatial resolution is 13×24 km^2 at nadir. The spatial resolution can be increased to 13×12 km^2 in the OMI zoom modes. In addition, two aerosol indices that give an indication of the dominating aerosol type are determined. The aerosols indices will be reported even in the case of cloud contaminated pixels.

The aerosol optical thickness, t, is defined as the vertically integrated (from the surface to the top of the atmosphere, TOA) aerosol extinction coefficient, k_{ext}

$$t(l) = \int_0^{TOA} k_{ext}(l, z)\, dz . \qquad [4\text{-}1]$$

Note that the aerosol optical thickness depends on the wavelength l.

The aerosol extinction coefficient is a measure of the attenuation of the incoming solar radiation by particle scattering and absorption, i.e., $k_{ext} = k_{sca} + k_{abs}$. It depends on the wavelength, aerosol material refractive index, particle size distribution, and particle shape. If the particle size distribution is fixed, the aerosol optical thickness is directly proportional to the total aerosol loading. The spectral variation of the aerosol optical thickness contains information on the aerosol size distribution and wavelength dependent refractive index.

The single scattering albedo is a measure of the fraction of aerosol extinction which is due solely to aerosol scattering effects. It is defined as the ratio of scattering to extinction coefficients,

$$w_0(l) = \frac{\int_0^{TOA} k_{sca}(l, z)\, dz}{\int_0^{TOA} k_{ext}(l, z)\, dz} . \qquad [4\text{-}2]$$

The single scattering albedo of non-absorbing aerosols is unity.

4.3. Theoretical background

4.3.1. Physical basis

In the absence of aerosol particles and clouds the radiance field emerging at the top of the Earth's atmosphere in the 330-500 nm region of the electromagnetic spectrum is mainly driven

by the scattering of incoming solar radiation by air molecules, and the radiation reflected by the surface and transmitted through the atmosphere. These radiative transfer processes are a strong function of wavelength. Absorption effects by gaseous species (mainly ozone and nitrogen dioxide) are of secondary importance in this spectral region. The surface contribution depends on the surface type. In the 330-400 nm region the surface albedo is generally very small (less than 0.1) for all scene types including deserts, but excluding snow and ice. At wavelengths longer than 400 nm, the surface contribution is still small for water-covered surfaces and most vegetation types, but increases rapidly with wavelength over the arid and semi-arid regions of the Earth.

Since molecular scattering and gas absorption effects are well known, for cloud-free conditions the satellite-measured departure of the radiation field from the pure Rayleigh-scattering case is due to the processes of scattering and absorption by aerosol particles and surface reflection effects.

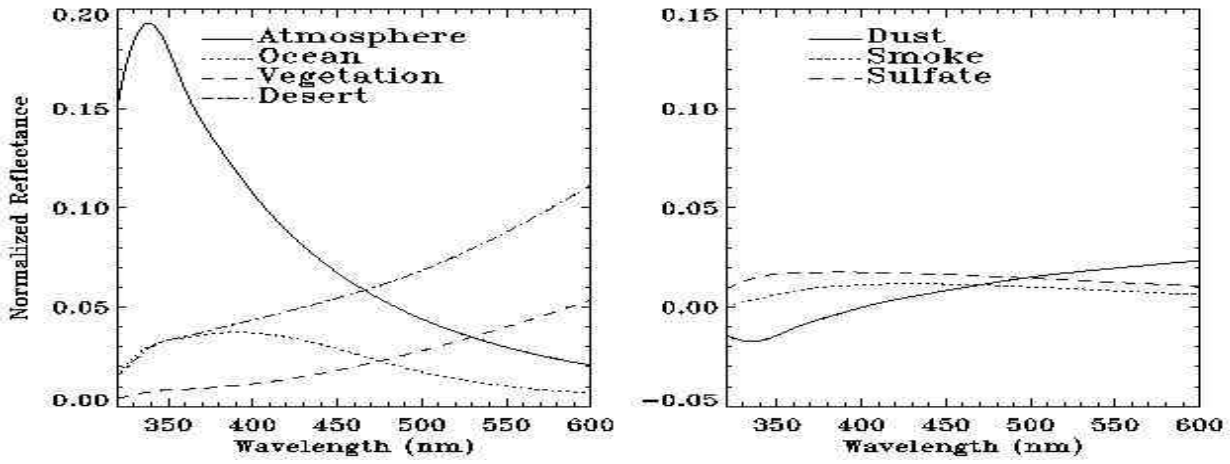

Figure 4.1. Left panel: Rayleigh atmosphere and surface components (for several surface types) of the reflectance at TOA as a function of wavelength.
Right panel: Contribution by three aerosol types of optical thickness 0.2 (550 nm), to TOA reflectance as a function of wavelength.

The atmosphere and surface contribution to the TOA reflectance as a function of wavelength is shown in Figure 4.1. In the visible and near infrared spectral regions, the contribution of Rayleigh scattering (mostly singly-scattered radiation) is generally small. Over water surfaces, the contribution of the surface to the TOA reflectance is also small in the visible and near infrared. Over most land surfaces, however, the contribution by the surface is significantly larger than the contribution of aerosol scattering, as shown in Figure 4.1. Therefore, the separation of the aerosol effect is very difficult without a precise characterization of the surface albedo. For this reason, visible and near infrared satellite retrieval of aerosol properties from radiance measurements is generally limited to dark water surfaces.

In the near UV Rayleigh scattering is much larger than in the visible and cannot be neglected. Multiple Rayleigh scattering increases the length of photon paths through an absorbing aerosol layer, so that the chance of absorption by aerosols is significantly enhanced. The height of an absorbing aerosol layer is also important. If the aerosol layer occurs high in the atmosphere, nearly all light that reaches the detector has to pass twice through the absorbing layer. If, on the other hand, the aerosol layer is located near the surface, only a fraction of the light that reaches the detector has to pass through this layer. For non-absorbing aerosols the altitude of the aerosol layer is much less important because scattering by aerosols does not

appreciable reduces the amount of multiple Rayleigh scattering. The near-UV surface contribution is low over both water and land surfaces [*Herman and Celarier,* 1997; *Koelemeijer et al.,* 2002]. The near UV ocean reflectivity is seldom larger than about 0.08, whereas all vegetated surfaces show a reflectivity no larger than about 0.04. The largest reflectivity of ice/snow free surfaces in the near UV corresponds to deserts with a typical value of about 0.08. In summary, the detection capability for absorbing aerosols is enhanced in the near UV where the large Rayleigh-scattering component enhances the aerosol 'color'. The capability of aerosol detection over the continents comes from the low value of the near UV albedo of most terrestrial surfaces.

The manner in which particle scattering and absorption modify the up-welling radiation at the top of the atmosphere depends on the aerosol microphysical properties and loading. In general, the main aerosol effect is an increase of the up-welling atmospheric radiation resulting from scattering by aerosol particles. Certain aerosol types, however, also absorb radiation and the resulting net effect depends on the strength of the absorption process as determined by the imaginary component of the aerosol refractive index. Aerosol absorption, therefore, can be inferred from satellite measurements in the near UV where multiple Rayleigh scattering is significant.

As illustrated in the right panel of Figure 4.1, the combination of near UV and visible observations in the OMI sensor allows a more precise characterization of aerosols properties than can be achieved using near UV or visible measurements separately.

4.3.2. Wavelength selection

The OMI instrument measures the backscattered radiance in the wavelength range between 270 and 500 nm, with a spectral resolution of approximately 0.5 nm. In this wavelength range, the scattering and absorption by atmospheric aerosol particles vary smoothly with the wavelength. The wavelength dependence is used to obtain information on the aerosol type, concentration and the size distribution. Because of the smooth variations with wavelength, the radiance spectrum may be conveniently sampled with an wavelength step of about 10 nm, without losing information.

In selecting wavelengths for aerosol sensing, the interference of absorption by gas species has to be avoided. Because at wavelengths shorter than about 330 nm the absorption of solar radiation by ozone (O_3) molecules is significant, the OMI aerosol algorithm uses wavelengths in the 330 –500 nm spectral region. The narrow O_2-O_2 absorption bands at 360 and 380 nm, as well as regions of strong Ring lines have been avoided. To increase the signal-to-noise ratio of the measured radiance, the spectral averaging is done over a 1-nm wide band instead of using the actual OMI spectral sampling distance. Thus, seventeen wavelength bands were selected for aerosol retrieval, and where possible, the wavebands were chosen to match wavelength bands of other sensors such as MODIS and TRIANA. Two additional wavelengths were selected: the peaks of the absorption of chlorophyll-a at 443 nm and chlorophyll-b at 470 nm. The selected wavelengths are listed in Table 4.1. Figure 4.2 shows a GOME spectrum for the 300 to 500 nm wavelength range. The vertical lines in this figure indicate the selected wavelength bands.

Table 4.1 Selected wavelength bands for the OMI aerosol product. Each band is 1 nm wide.

No	Wav. [nm]	Comments
1	331.7	
2	342.5	
3	354.0	
4	367.0	
5	376.5	
6	388.0	TRIANA
7	399.5	
8	406.0	
9	416.0	
10	425.5	

No	Wav. [nm]	Comments
11	436.5	
12	442.0	MODIS Ch 9
13	443.0	Max chlorophyll a abs, MODIS Ch 9
14	451.5	
15	463.0	MODIS Ch 3
16	470	Max chlorophyll b abs, MODIS ch 3
17	471	MODIS ch 3
18	483.5	MODIS ch 10
19	494.5	

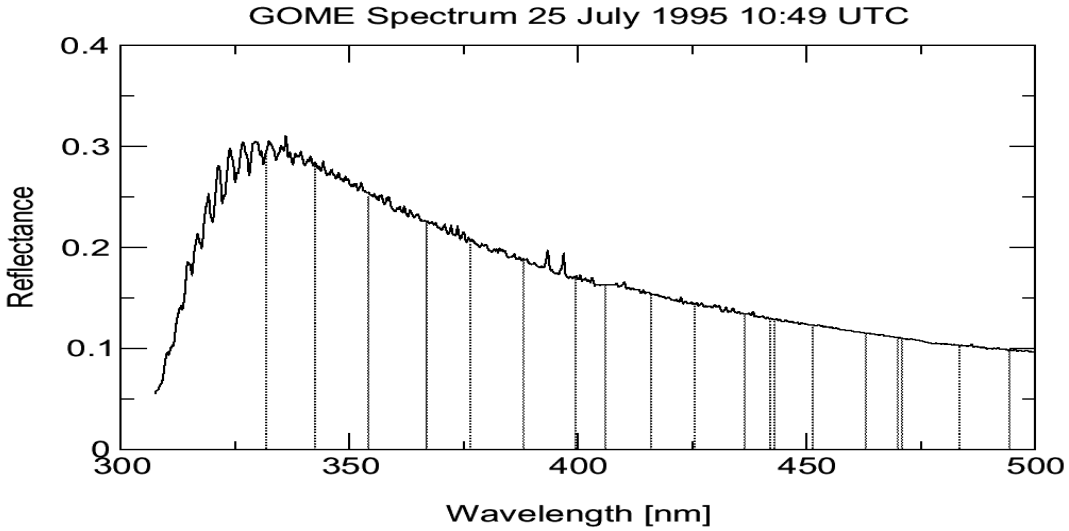

Figure 4.2. GOME reflectance spectrum between 300 and 500 nm, for a cloud-free pixel over the Netherlands (center of pixel 52.23°N, 4.71°E) measured on 25 July 1195, 10:49 UTC. The spectral resolution is decreased to match the OMI spectral resolution. The vertical lines indicate the center of the wavelength bands selected for the OMI aerosol algorithm.

4.3.3. Aerosol models

Satellite retrieval of aerosol properties using nadir-viewing instruments like OMI is a so-called ill-posed problem, meaning that there are more unknowns than equations. Retrieval of the aerosol optical thickness and single scattering albedo requires the use of microphysical aerosol models. The aerosol physical properties that drive their radiative transfer effects are the aerosol particle size distribution and complex refractive index. In addition, aerosol radiative transfer effects in the blue and the UV depend on the vertical distribution of the aerosols. The aerosol size distribution and the chemical composition of the particles are determined by the geographic location of emission sources, type of emission, and transport, transformation and removal processes.

A set of 24 candidate aerosol models are used in the OMI aerosol algorithm. The models are grouped in five major aerosol types according to their origin. Each aerosol type consists of sub-types according to their optical properties. An aerosol sub-type includes several aerosol models depending on particle size distribution or vertical distribution. On a global scale, four

main tropospheric aerosol types can be distinguished according to their production processes: urban-industrial aerosols originated from fossil fuel combustion; carbonaceous aerosols generated from natural and anthropogenic biomass burning: desert dust aerosols, injected in the atmosphere by the wind lifting capability; and the naturally produced oceanic aerosols. After major volcanic eruptions, the aerosol optical thickness of the stratosphere can be significantly increased for several years. For this reason also a volcanic aerosol type is included. So in total five main aerosol types are used in the OMI aerosol algorithm. The aerosol size distributions are represented by log-normal functions. The parameters of the particle size distributions (i.e., mode radii and standard deviations) and the refractive index data used in the OMI aerosol algorithm were taken mainly from long term Aerosol Robotic Network (AERONET) sun-photometer observations [*Holben et al.*, 1997] and are listed in Table 4.2. A brief description of each main aerosol type is given below.

Urban-industrial

Fossil fuel combustion is the main source for the urban-industrial type aerosols. The size of the particles is a function of the relative humidity. The soot content, that mainly determines the absorption of the mixture, varies according to industrial development and environmental regulations. To account for variations in the size distribution and absorption, the industrial type consists of six sub-types (see Table 4.2).

Biomass burning

Anthropogenic biomass burning occurs on a large scale in many parts of the world. These fires are often seasonal as they precede the new growth season just before the rainy season. Natural forest fires may occur from the arctic circle to the tropics and these fires are difficult to predict. The optical properties of smoke from biomass burning change somewhat with the type of vegetation that is burned. The refractive index varies a little between the Amazonian rain forest, South American Pampas and the African Savanna. To account for variations in absorption and size distribution, six sub-types are used for the biomass burning aerosol type.

Desert dust

Desert dust can be transported in elevated layers over several thousands of kilometers from its source. The chemical composition and thus the refractive index is determined by the source region. Absorption by dust increases strongly towards the UV, and the magnitude of the increase is largely determined by the hematite content, which varies for the different dust sources [*Sokolik et a.*, 1993]. Two desert dust aerosol sub-types characterized by low and high hematite content are used. Each dust model consists of a bimodal particle size distribution with a fine or accumulation particle mode, representing particles that can be transported over large distances, and a coarse mode that will be of more importance close to the source. The effect of dust aerosol on the top-of-the-atmosphere radiance depends also on the height of the dust layer. Therefore, two aerosol heights, 3 and 5 km, are used in this aerosol type. The wavelength dependent refractive index of dust is based on the work by *Colarco et al.* [accepted for JGR, 2002] and *Sinyuk et al.* [2002], based on the combined used of AERONET observations, transport model calculations and TOMS observations. Non spherical effects are especially important for desert dust particles. For this reason we will also use desert dust models with non-spherical particles. The non-spherical particles size distribution are computed using the T-Matrix method [*Mishchenko and Travis*, 1998]. During the validation phase, we will evaluate the advantages of using non-spherical dust models.

Oceanic

In clean marine environments, the aerosols consists mainly of sea salt. In the coastal regions, however, the aerosol can be a mixture of sea salt and continental outflow. To account for these effects we use three aerosol models over the ocean. These models are based on the Navy Oceanic Vertical Aerosol Model [*Gathman and Davidson*, 1993]. Two of these models are intended for the coastal regions, the difference between them being the absorption of the small mode. The third model is for clean marine conditions and it is dominated by the larger sea salt particles.

Volcanic

The main component of volcanic aerosol is sulfuric acid. The layer height- and size-distribution are based on SAGE observations of the Pinatubo eruption [Bauman, 2000].

Table 4.2 Aerosol size distribution and refractive index for the selected OMI aerosol models. Several of the five major types are divided into sub-types according to amount of absorption or the vertical, log-normal distribution. These sub-types can contain a number of aerosol models that differ in particle size distribution and/or refractive index. The industrial and biomass types have a bi-modal distribution. The mean particle radius and its standard deviation are given separately for both modes. Aerosol number concentration is normalized to unity. The relative contribution of the second mode to the number concentration is represented by the fraction m2.

			Mean Radius (μm)		Standard Deviation (μm)		Fraction of m2	Ref. Index	
Type	Sub-type	Model	m1	m2	m1	m2		real	imag
Industrial	IS	IS1	0.078	0.497	1.499	2.160	$4.36\ 10^{-4}$	1.4	0.004
		IS2	0.088	0.509	1.499	2.160	$4.04\ 10^{-4}$	1.4	0.004
		IS3	0.137	0.567	1.499	2.160	$8.10\ 10^{-4}$	1.4	0.004
	IA	IA1	0.085	0.641	1.560	2.004	$7.00\ 10^{-4}$	1.45	0.012
		IA2	0.090	0.676	1.560	2.004	$6.84\ 10^{-4}$	1.45	0.012
		IA3	0.109	0.804	1.560	2.004	$6.95\ 10^{-4}$	1.45	0.012
Biomass	BL	BL1	0.074	0.511	1.537	2.203	$1.70\ 10^{-4}$	1.5	0.010
		BL2	0.087	0.567	1.537	2.203	$2.06\ 10^{-4}$	1.5	0.010
		BL3	0.124	0.719	1.537	2.203	$2.94\ 10^{-4}$	1.5	0.010
	BH	BH1	0.076	0.665	1.492	2.075	$2.07\ 10^{-4}$	1.5	0.020
		BH2	0.080	0.705	1.492	2.075	$2.05\ 10^{-4}$	1.5	0.020
		BH3	0.097	0.866	1.492	2.075	$1.99\ 10^{-4}$	1.5	0.020
Desert Dust	DL	DL3KS	0.052	0.67	1.697	1.806	$4.35\ 10^{-3}$	1.53	[a] LS
		DL5KS	0.052	0.67	1.697	1.806	$4.35\ 10^{-3}$	1.53	[a] LS
		DL3KN	0.052	0.67	1.697	1.806	$4.35\ 10^{-3}$	1.53	[a] LN
		DL5KN	0.052	0.67	1.697	1.806	$4.35\ 10^{-3}$	1.53	[a] LN
	DH	DL3KS	0.052	0.67	1.697	1.806	$4.35\ 10^{-3}$	1.53	[a] HS
		DL5KS	0.052	0.67	1.697	1.806	$4.35\ 10^{-3}$	1.53	[a] HS
		DL3KN	0.052	0.67	1.697	1.806	$4.35\ 10^{-3}$	1.53	[a] HN
		DL5KN	0.052	0.67	1.697	1.806	$4.35\ 10^{-3}$	1.53	[a] HN
Oceanic	MS	MS	0.030	0.240	2.030	2.030	$1.55\ 10^{-4}$	1.4	0.004 (m1) $5\ 10^{-8}$ (m2)
	MA	MA	0.030	0.240	2.030	2.030	$1.55\ 10^{-4}$		0.012 (m1) $5\ 10^{-8}$ (m2)
	MC	MC	0.030	0.240	2.030	2.030	$1.53\ 10^{-2}$	1.4	$5\ 10^{-8}$
Volcanic [b]	V	V	0.230	-	0.800	-	-	1.45	7.5010^{-7}

[a] Wavelength-dependent with (H)igh or (L)ow absorbance and (S)pherical or (N)on spherical particles.
[b] Only used in case of eruptions

4.3.4. Forward model

Radiative transfer calculations

The OMI aerosol algorithm derives aerosol optical properties by comparing the measured reflectance to results from radiative transfer calculations. These radiative transfer calculations are performed for cloud-free and horizontally homogeneous atmospheres, overlying a Lambertian surface. In this case, the reflectance emerging at the top of the atmosphere can be written as:

$$R(l) = R_a(l) + \frac{A_s(l)}{1 - A_s(l) \cdot s(l)} T(l) \qquad [4\text{-}3]$$

where $R_a(l)$ is the contribution of atmospheric scattering (also called path reflectance), $A_s(l)$ is the surface reflectivity, $T(l)$ the total direct and diffuse transmittance of the atmosphere for light that travels to the surface and then back to the sensor, and $s(l)$ is the spherical albedo of the atmosphere when it is illuminated from below. Note that all terms, except the surface reflectivity and the spherical albedo, depend on the Sun and viewing geometry. With the exception of the surface albedo, all terms in equation [4-3] also depend on atmospheric surface pressure.

Radiative transfer models are used to determine the path reflectance ($R_a(l)$), the transmission ($T(l)$), and the spherical albedo ($s(l)$) for all wavebands used in the algorithm. Multiple scattering and polarization are taken into account. At large solar zenith angles (>70°) spherical effects of the Earth's atmosphere also have to be accounted for. The pressure and temperature profiles, important for the Rayleigh optical thickness, and ozone and nitrogen dioxide profiles are taken from the US 1976 Standard Atmosphere. The Ring effect is neglected in the radiative transfer calculations.

Two radiative transfer codes are available to the algorithm development team. The first model is the Doubling Adding KNMI (DAK) code [*De Haan et al.,* 1987; *Stammes et al.,* 1989; *Stammes,* 2001]. DAK uses the doubling-adding method to solve the radiative transfer equation for plane parallel atmospheres. The second radiative transfer code uses the Gauss-Seidel iteration scheme to calculate a steady-state solution including all significant orders of scattering [*Herman and Browning,* 1965]. It includes polarization and accounts for spherical atmosphere effects via the pseudo-spherical approximation [*Caudill et al.,* 1997]. Comparing results from the two radiative transfer codes will provide an indication of the accuracy of the radiative transfer calculations.

Look-up tables

Radiative transfer calculations are carried out for a set of nodal points in solar zenith angle, viewing zenith angle, relative azimuth angles, surface pressure and aerosol concentration. The results are stored in separate files for each of the 24 aerosol models as well as for Rayleigh scattering.

Table 4.3 contains an overview of the discrete values for each of the LUT parameters. The values for the entries are chosen in such a way that interpolation errors are minimized while retaining a manageable table size. These multi-dimensional tables contain the following results from the radiative transfer calculations: the reflectivity at the top of the atmosphere, the bi-directional diffusely transmitted radiation for a black surface (stored in anticipation of future retrieval improvement by taking into account bi-directional surface reflection), the product of the direct and diffuse transmittance, the spherical albedo of the atmosphere as seen from below, and the total and diffuse downward flux (see Table 4.4). In addition, the aerosol optical thickness and the single scattering albedo for each wavelength are stored.

Table 4.3. Overview of the look-up table dimensions for 24 aerosol types and for the Rayleigh atmosphere. These variables are the axis of a multi-dimensional grid with a limited amount of nodal entries. The grid contains the pre-calculated values.

Variable name	Symbol	Units	Nr. of entries	Entries
Surface pressure	p_{sfc}	hPa	2	1013, 600
Wavelength	λ	nm	19	see Section 4.3.2
Cosine of the solar zenith angle	μ_0	degree	8	0.3, 0.4, ... , 1.0
Cosine of the viewing zenith angle	μ	degree	5	0.5, 0.6, ... , 1.0
Relative azimuth angle	ϕ-ϕ_0	degree	11	0, 30, 60, 90, 120, 150, 160, 165, 170, 175, 180
Aerosol optical thickness at 500 nm	τ_{500}		5	0.1, 0.5, 1.0, 2.5, 4.0

Table 4.4 Variables and dimensions for the results of Mie and radiative transfer calculations in the look-up tables for atmospheres without aerosols (pure Rayleigh case) and for atmospheres with aerosols, for 24 different aerosol models. The number of values in each dimension can be found in Table 4.3.

Variable name	Symbol	Dimensions
Path reflectance	R_a	p_s , λ, μ_0, μ, ϕ-ϕ_0, τ_{500}
Bi-directional transmitted radiation (A_s=0)	T_d	p_s , λ, μ_0, μ, ϕ-ϕ_0, τ_{500}
Total transmission (downward-upward)	T	p_s , λ, μ_0, μ, τ_{500}
Diffuse downward flux	F_d	p_s , λ, μ_0, τ_{500}
Total downward flux	F_t	p_s , λ, μ_0, τ_{500}
Spherical albedo	s	p_s , λ, τ_{500}
Aerosol optical thickness	τ	λ, τ_{500}
Single scattering albedo	ω_0	λ

4.4. Inversion procedure

Based on the theoretical basis discussion presented in Section 4.1, two inversion methods will be applied to the OMI aerosol data. The primary method of aerosol retrieval over water surfaces is a multi-wavelength fitting procedure that uses the 17 selected wavelengths (Table 4.1). The application of this approach over the oceans takes advantage of the low surface albedo over the entire OMI spectral range. Because of the uncertainty associated with the characterization of surface effects in the 400-500 nm range in the application of the multi-wavelength approach over land, the near UV inversion method [*Torres et al.*, 1998] is used as the primary retrieval technique over the land surfaces, including deserts. The near UV method uses measurements at 342.5 and 388 nm to retrieve aerosol optical thickness and single scattering albedo. Figure 4.3 shows a schematic of the inversion procedure. Five key steps can be distinguished: 1) computation of aerosol indices, 2) cloud and glint screening, 3) aerosol type pre-selection, 4) application of inversion method, and 5) output collection.

First the aerosol indices are determined. In case of cloud contamination, the aerosol indices are the only aerosol parameters that are available in the output product. Also, these aerosol indices are used further on in the retrieval process. The second step includes cloud and sea glint screening. In the screening of sub-pixel cloud contamination, the OMI Level 2 cloud product, the aerosol indices, and the measured radiances themselves will be used. Sea glint screening is done by means of geometric considerations. In the third step of the inversion method a pre-selection of the aerosol types is made. This pre-selection is based on a geographical distribution of background aerosol, and on the aerosol indices (derived in step 1) to take into account the presence of non-background aerosols (see Sections 4.4.2 and 4.5.4). In the fourth step the actual retrieval takes place using the multi-wavelength and near UV methods

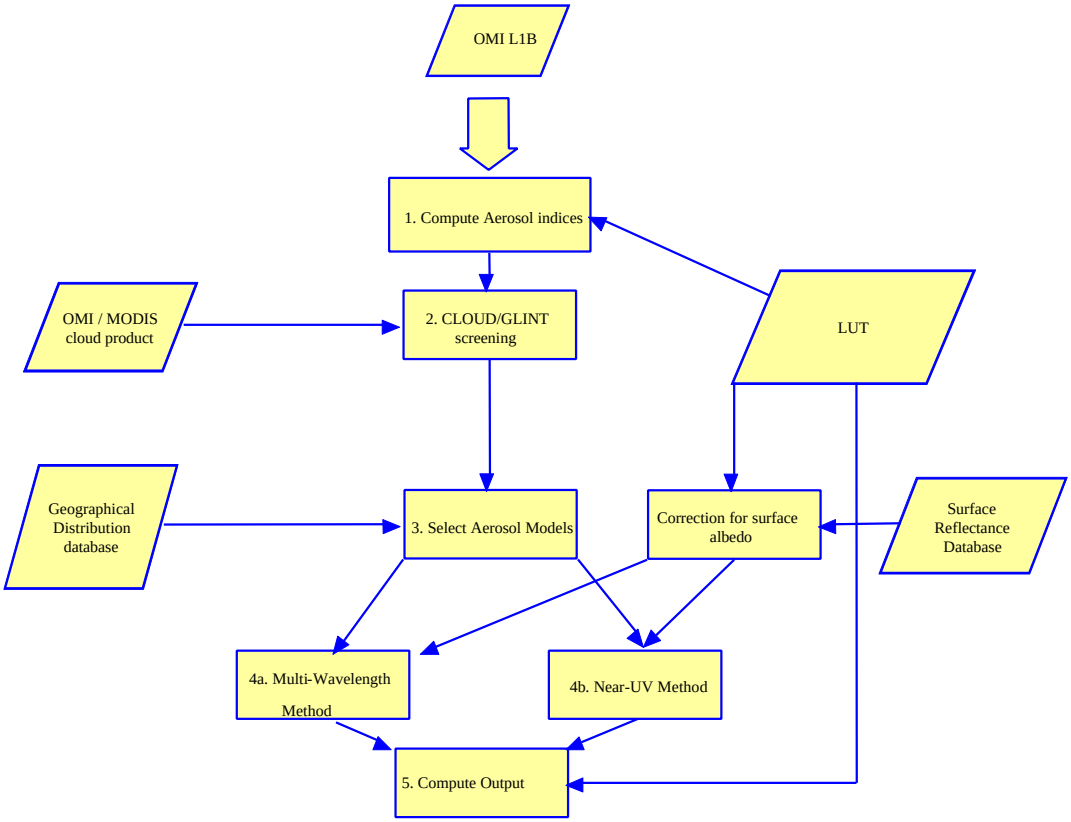

Figure 4.3 Schematic of the inversion method.

Finally, the output of the algorithm is collected. In case of cloud contamination the only aerosol parameters are the aerosol indices. For cloud-free conditions, the aerosol optical thickness and single scattering albedo for the wavelengths in Table 4.1 (multi-wavelength method) will be reported, in addition to the 388 nm aerosol optical thickness and single scattering albedo retrieved by the near UV inversion method. The inversion steps are described in more detail in the following sections.

4.4.1. Aerosol indices

The Aerosol Index concept [*Torres et al.,* 1998], which was developed based on the TOMS observations in the near UV, will be applied to the OMI measurements, and will be extended to the visible spectral region. As used in the OMI aerosol algorithm the Aerosol Index is defined as

$$a_{l_2} = -100\log\{[I_{l_1} / I_{l_2}]_{meas}\} + 100\log\{[I_{l_1}(A_{LER_{l_1}}) / I_{l_2}(A_{LER_{l_2}})]_{calc}\} \qquad [4\text{-}4]$$

where $(I_{l_1}, I_{l_2})_{meas}$ are the measured radiances at two wavelengths ($l_2 > l_1$), and $(I_{l_1}, I_{l_2})_{calc}$ are the corresponding calculated radiances. A_{LER} is the wavelength dependent surface Lambert-equivalent reflectivity. When using $?_1$= 342.5 nm and $?_2$= 388.0 nm in equation [4-4], a UV aerosol index, a_{388}, is obtained. By the same token when $?_1$= 388 nm and $?_2$= 494.5 nm a visible aerosol index, a_{494}, is calculated. These aerosol indices are a measure of the change in spectral contrast (with respect to a pure Rayleigh atmosphere) due to the wavelength-dependent effects of clouds and aerosols. Clouds or any other type of non-absorbing large aerosol particle yield near-zero UV aerosol index values [*Hsu et al.,* 1996]. To isolate the net aerosol effect, the spectral

dependence of the surface reflectance must be taken into account. Because of the short separation of the wavelengths involved, the surface effect in the computation of the UV aerosol index is very small. To compute the visible aerosol index, however, information on the spectral contrast of the surface reflectance is required. Climatological data sets on surface reflectance obtained from SeaWIFS, MODIS and TOMS observations [*Herman and Celarier*, 1997] will be used to characterize the spectral dependence of the surface reflectance.

4.4.2. Aerosol type selection

Non-background aerosol type will be selected based on two criteria: spectral differentiation using the aerosol indices, and geographical distribution. Absorbing and non-absorbing aerosols are easily separated based on the near UV aerosol index which is positive for absorbing aerosols and negative for non-absorbing aerosols [*Torres et al.*, 1998]. The selection of absorbing aerosol type (i.e., carbonaceous and mineral dust aerosols) will be primarily based on geographical considerations taking advantage of the known global distribution of sources of mineral aerosols and transport patterns, as well as the global distribution and seasonality of biomass burning activity and boreal forest fires. An alternate approach based on the use of the visible aerosol index will be applied over those areas of the world where the presence of either dust or smoke is likely to occur such as the tropical Atlantic Ocean during the November-April period and Western Australia during the southern hemisphere spring season.

Based on radiative transfer calculations, the visible aerosol index (a_{494}), allows the separation of gray absorbing particles (wavelength independent imaginary refractive index), such as carbonaceous aerosols, that in most cases yield negative a_{494} values, from colored absorbing aerosols (wavelength dependent imaginary refractive index) like mineral dust, that produce positive values of a_{494}. As shown in Figure 4.4, aerosol types can be identified with the combined use of the UV and visible aerosol indices. When the optical thickness of carbonaceous aerosols becomes extremely large (greater than about 2), a_{494} becomes positive and smoke aerosols cannot be differentiated from dust. This technique of aerosol type identification will be tested in the OMI algorithm.

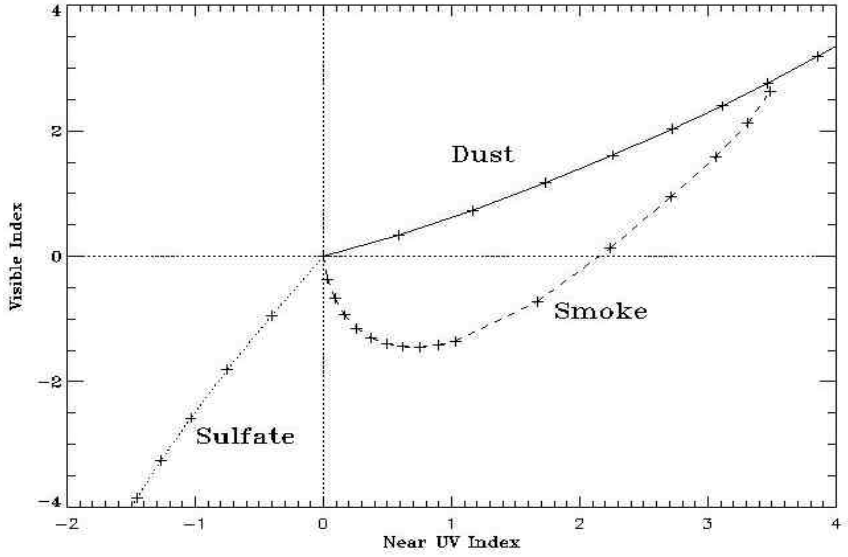

Figure 4.4 An example of separation of aerosol types using the aerosol indices. Lines represent increasing aerosol optical thickness (550 nm) from 0 to 1.0 (in 0.1 steps) and from 1.0 to 4.0 (in 0.5 increments). The solid line represents desert dust aerosols, the dashed line represents carbonaceous aerosols, and the dotted line represents non-absorbing aerosols Smoke layers of optical thickness smaller than about 2 produce a negative visible aerosol index and are clearly distinguishable from dust layers.

4.4.3. Multi-wavelength method

The multi-wavelength method makes maximum use of all available information on aerosol properties in the 17 selected wavelength bands between 330 and 500 nm. Because the available information is limited [e.g., *Tanré et al.*, 1996], it is not possible to use all 24 aerosol sub-types to fit the measured spectrum. Instead, first a pre-selection of 2 to 3 aerosol sub-types is made, based on the aerosol indices and the aerosol geographical distribution climatology (see Section 4.5.5). To determine which of the pre-selected sub-types fits the measured spectrum best, a least squares minimization is applied using each of the sub-types. Thus, the following merit function c^2 is minimized for each of the pre-selected sub-types:

$$c_j^2 = \sum_{i=1}^{17} \left(\frac{R_m(\lambda_i) - R_j(t_j(\lambda_{ref}), \lambda_i)}{e_m(\lambda_i)} \right)^2, \qquad [4\text{-}5]$$

where $R_m(\lambda_i)$ is the measured reflectance, $R_j(t_j(\lambda_{ref}),\lambda_i)$ is the reflectance for the aerosol sub-type j as a function of the aerosol optical thickness at the reference wavelength $t_j(\lambda_{ref})$, and $e_m(\lambda_i)$ is the error in the measured reflectance.

The aerosol sub-type with the smallest c^2 is selected for the present ground pixel and used to determine the aerosol optical thickness at all wavelengths. The single scattering albedo is directly determined by the selected aerosol type.

As the reflectance is a non-linear function of the aerosol optical thickness, a non-linear fitting method has to be applied. A modified Levenberg-Marquardt method [*More*, 1978] as adapted from the SLATEC mathematical library [*Fong et al.*, 1993] is used for the non-linear fitting. Information on the quality of the fit is derived from the covariance matrix. From the covariance matrix the variance of the fitted parameters is determined, as well as the correlation between them. This information is used to calculate the precision in the derived aerosol optical thickness. In addition, the residual reflectance contains information on how well the measurements are represented by the fitted aerosol model.

4.4.4. Near UV method

The near UV approach takes advantage of the low ultraviolet surface albedo of all terrestrial surfaces (free of ice and snow) for the characterization of aerosols over all land types including deserts. The application of the near UV approach to the OMI data will extend the multi-year long record of aerosol properties derived from the TOMS record [*Torres et al.*, 2002].

In the near-UV method, measurements of the backscattered radiances at 342.5 and 388 nm are used. Aerosols are characterized in terms of optical thickness and single scattering albedo by examining the relationship between the spectral contrast ($I_{\lambda 1}/I_{\lambda 2}$) and the radiance at the longer wavelength ($I_{\lambda 2}$). The inversion algorithm makes use of pre-computed look-up tables of radiances emerging at the top of an aerosol-laden atmosphere. A set of three to five candidate aerosol models is selected according to geographical location and season.

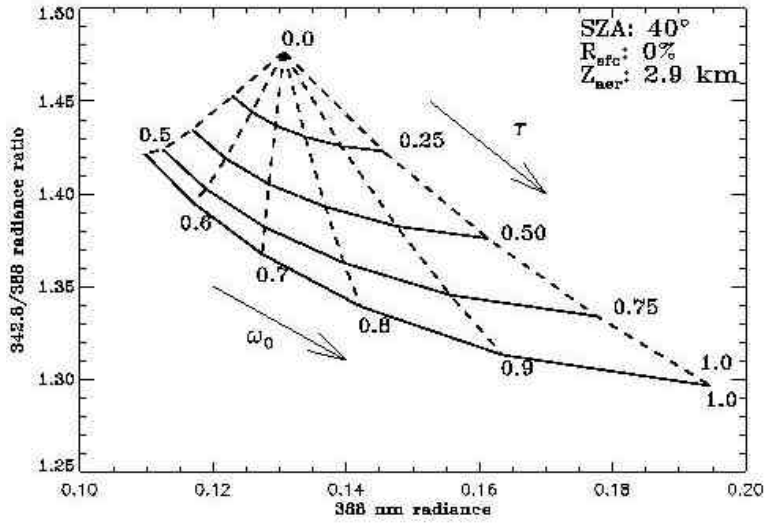

Figure 4.5 Graphic illustration of the near UV retrieval method. Dashed lines represent different aerosol models as characterized by their single scattering albedo. Solid lines represent different values of optical thickness. For a given geometry and aerosol layer height, the measured radiances at 342.5 and 388 nm are associated with a set of values of aerosol optical thickness (t) and single scattering albedo (? $_0$).

As shown in Figure 4.5, a set of measurements of radiances at two near UV channels is, within the domain of the selected aerosol models, associated with a set of values of optical thickness and single scattering albedo. Near UV surface albedo and height of absorbing aerosol layers above the surface are prescribed. Aerosol optical thickness derived by application of the near UV approach to the TOMS data has been validated with AERONET measurements [*Torres et al*., 2002] as illustrated in Figure 4.6. An unpublished comparison of TOMS retrieved to AERONET [*Dubovik and King*, 2000] derived single scattering albedo of carbonaceous aerosols at several sites in Africa during the SAFARI 2000 campaign is shown in Table 4.5.

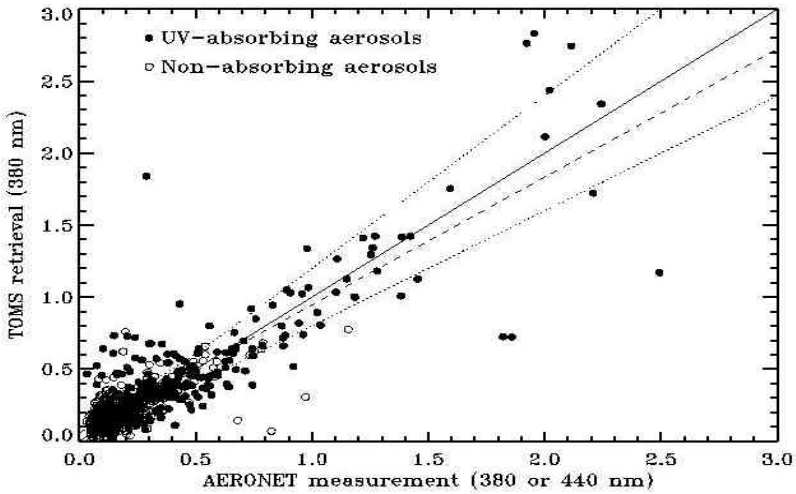

Figure 4.6 Validation of TOMS retrieved optical thickness over a three-year period at six AERONET stations. Solid curve represents the perfect agreement line, dashed line is the resulting linear fit, and the dotted lines represent the estimated uncertainty (±30%). Details of the validation analysis are discussed in Torres et al. [2002].

Table 4.5 Comparison of single scattering albedo retrieved by AERONET (440 nm) to TOMS derived values (380 nm).

Site	Location	AERONET (440 nm)	TOMS(380 nm)
Mwinilunga	11S 24E	0.89±0.03	0.89±0.03
Ndola	12S 28E	0.87±0.03	0.88±0.03
Senanga	16S 23E	0.88±0.03	0.87±0.03
Solwezi	12S 26E	0.88±0.03	0.88±0.03
Zambezi	13S 23E	0.86±0.03	0.88±0.03

4.5. Environmental model

4.5.1. Surface Reflectivities

One of the most important a priori data sets that are needed in the OMI aerosol algorithm are the surface reflectivities for all wavelengths used in the algorithm. Two methods will be implemented to obtain such these data: (1) by using a surface reflectivity climatology, and (2) by using a ocean color model. Over the ocean it will be possible to use either a climatology or the model to determine the spectral surface reflectivity, over land always the climatology will be used.

The first approach is to use a monthly climatology of spectral surface reflectivities. For reprocessing, spectral surface reflectivities based on OMI data itself may be used, however these data are not available at launch. In this case we have to rely on existing surface reflectivity climatologies as derived using TOMS, GOME, MODIS and SeaWIFS data. It is noted that the surface reflectivity depends also on the Sun/satellite geometry. The bi-directional effects of the surface reflectivity may be important, given the large swath of OMI. However, the existing TOMS and GOME climatologies do not include such information. If the bi-directional surface reflectance is determined for OMI, it will be accounted for in the aerosol algorithm during reprocessing.

The TOMS surface reflectivity is based on measured reflectivity over the lifetime of the Nimbus-7 TOMS instrument (1978-1993) [*Herman and Celarier*, 1997]. This climatology derives the minimum Lambert equivalent reflectivity of the Earth's surface for the 340 – 380 nm. A simple atmospheric correction is applied that accounts for Rayleigh scattering, however, some persistent cloud features as well as some background aerosol effects are still present in this database. Recently, a similar analysis has been applied to GOME data for the period 1995-2000, resulting in a monthly climatology of Lambert equivalent reflectivities of the surface at 11 wavelengths [*Koelemeijer et al.*, 2002]. The wavelengths in the OMI range are: 335, 380, 416, 440, 463, 494.5 nm. Clearly, the large wavelength range of GOME is an advantage, but the drawback is the large footprint of the GOME pixels, which increase the chance of residual effects of clouds. Preliminary results at 335 and 380 nm show good agreement between GOME and TOMS surface reflectivities. A third data set that may be used is the surface reflectivity derived from MODIS at 470 nm [*Vermote and Vermeulen*, 1999]. This MODIS product includes a correction for aerosol effects. Also, due to the high spatial resolution of 500 m, the probability of cloud contamination is much smaller than for TOMS and GOME. Comparing this data set with the GOME data and -after launch- with the OMI surface reflectivity data may give a good indication of contamination by clouds and aerosols in these data sets.

The second approach is to use a model for the spectral reflectivity of the ocean. The model that will be implemented is from the 6S model [*Vermote et al.*, 1997]. In this model the ocean surface reflectance is modeled as a function of the chlorophyll concentration, wind speed and wind direction. Fresnel reflection, reflection on whitecaps, and reflection by the ocean are

accounted for in this model. The optical properties of the ocean for the UV will be taken from *Vasilkov et al*. [2001]. The chlorophyll concentrations that are needed as input for the model will be obtained from the MODIS weekly mapped ocean products.

4.5.2. Cloud mask

Aerosol optical thickness and single scattering albedo can only be derived for cloud-free scenes. Although for cloud contaminated pixels it is possible to retrieve some aerosol information via the aerosol indices (see Section 4.2), the retrieval of the aerosol optical thickness and single scattering albedo critically rely on the cloud screening. Therefore, strict cloud screening is an essential step in the algorithm. The cloud screening consist of two independent tests, which have to be passed to mark a pixel as cloud-free.

The first test is a combination of a radiance threshold and the near UV aerosol index. Clouds give an increased radiance that may be detected using a simple threshold. However one has to distinguish between clouds and aerosols, to avoid marking pixels with high aerosol concentration as cloud-contaminated. For this reason, pixels that exceed the radiance threshold and have a near UV aerosol index near zero are rejected. This method was already applied for cloud screening of TOMS data [*Torres et al*., 2002].

A second test is based on the spatial homogeneity of the sub-pixel data. The standard OMI pixel size of 24×13 km^2 is the result of co-adding five consecutive sub-pixels. However, each OMI detector (UV and VIS) has one wavelength in which the data is not co-added. The sub-pixels in these two channels can be used to estimate the degree of standard pixel homogeneity. The sub-pixels are not complementary but have a substantial overlap in the flight direction. They are sized about 24×10 km^2 with a shift of 2.6 km in flight direction. To avoid boundary effects and to decrease the statistical error, two sub-pixels of the preceding and of the following pixel will be included in the spatial homogeneity test. The test is done by looking at the standard deviation of the radiances of the nine small pixels. If this standard deviation exceeds a threshold value, the pixel is rejected, because it probably contains sub-pixel clouds. This procedure might also reject unclouded pixels in cases with inhomogeneous aerosol distribution or surface reflectance. This is an unfortunate side effect of a strict cloud screening but is preferred over cloud-contaminated results.

Another possibility for cloud detection is to perform a post-processing procedure using a cloud mask derived from observations from another sensor such as MODIS on EOS-AQUA or geostationary satellites like METEOSAT and GOES. The success of such a cloud screening approach depends on the overpass time difference between the Aura spacecraft and the second sensor, which should not be larger than about 15 minutes.

4.5.3. Sun-glint mask

Sun-glint effects are excluded by rejecting those observations where the viewing geometry over the oceans is likely to produce sun-glint effects. Observations for cone angles, i.e., the emergent zenith angle relative to the specular reflection angle [*King et al*., 1999], less than a threshold value are rejected. A preliminary threshold value of 40º has been selected.

4.5.4. Aerosol geographical distribution

In general, the tropospheric aerosol load of an atmospheric column at a given location consists of a background aerosol component of local origin residing in the lowest 2 km of the atmosphere. In addition, an elevated layer of carbonaceous or mineral aerosols is often present. These free-troposphere aerosol layers result from the long-range transport of material from distant biomass burning and desert dust sources. The seasonal cycle of agriculture related

biomass burning and dust lifting in the major deserts of the world is generally well known, the long-range transport is determined by prevailing meteorological conditions. The OMI aerosol algorithm takes into account the dynamic nature of the aerosol field in selecting candidate aerosol models for the retrieval of aerosol properties. For each location a background aerosol sub-type will be selected based on geographical location and surface type (i.e., land or ocean) as indicated in Table 4.5

Table 4.5 Geographical distribution of background aerosol sub-types.

Latitude zone	Land	Ocean
30ºN 90ºN	IS	MS,MC,IS
30ºS 30ºN	IA	MA,MC,IA
90ºS 30ºS	IS	MS,MC

In addition to the background aerosol representation, carbonaceous or mineral dust models will be added to the set of candidate aerosol models as indicated by the aerosol indices as discussed in Section 4.4.1.

4.5.5. Aerosol profiles

In addition to aerosol micro-physical properties, satellite-measured radiances in the near UV and blue regions of the spectrum also depend on the height of the aerosol layer. This dependence is largest for absorbing aerosols and negligible for all practical purposes when the aerosols are non-absorbing. For that reason, in the OMI algorithm the aerosol profile must be prescribed. Depending on the aerosol type, three vertical distributions are used. An exponentially shaped profile with a 2 km scale height is used for the IS and IA models. A similar profile but with a smaller scale height (1.5 km) is used for the MS, MA and MC models. For biomass burning aerosols (BH and BL models), a single-layer Gaussian distribution of maximum concentration at 3 km and a half-width of 1 km is used. This choice is based on Lidar observations of smoke plumes in Southern Africa and South America during the TRACE-A experiment [*Anderson et al.*, 1996]. Two single-layer Gaussian distributions with peak concentrations at 3 and 5 km are used for the dust (DL and DS) models to account for the seasonal variability of the altitude of a Saharan dust layer which is minimum in winter and maximum during summer.

4.6. Sensitivity analysis

In this Section the error analysis for the OMI aerosol product is presented. The main error sources for the aerosol product are cloud contamination, errors in the assumed surface reflectivity, instrumental errors, and errors in the aerosol models. The error analysis presented here is intended to be a first-order estimate of the errors, using a limited set of cases. Unless stated otherwise, the discussed error analysis applies to both the multi-wavelength and near UV methods. During the algorithm validation (see Section 4.7), more end-to-end tests of the algorithm are foreseen.

4.6.1. Clouds

Although several cloud-screening tests are used to construct an accurate cloud mask, there may still be ground pixels with remaining sub-pixel clouds. As the optical thickness of clouds is generally much larger than the aerosol optical thickness, even a small amount of cloud contamination can cause large errors in the aerosol optical thickness. If 5% of the pixel contains clouds, the resulting errors in the aerosol optical thickness are estimated to be of the order 0.1 to

0.2 [*Torres et al.*, 1998]. Note that these errors are of the same order as the expected minimum values for the aerosol optical thickness. The errors in the single scattering albedo are 0 to 0.15, where the largest errors occur for the most absorbing aerosol types. The magnitude of the errors caused by cloud contamination again stresses the importance of an accurate cloud mask.

4.6.2. Surface reflectivity

As described in Section 5.1, the surface reflectivity is used from a monthly climatology. The sensitivity of the retrieval procedure was tested by using a surface reflectivity with an offset of 0.01 with respect to the value used in the forward model. Note that given the low surface reflectivities for most surfaces in the wavelength range used in the algorithm, an absolute offset of 0.01 corresponds to a relative change of 20%. The effect of the derived optical thickness is an absolute rms error of 0.07 at 500 nm, which increases to 0.09 at 330 nm, in agreement with the values reported in *Veefkind et al.* [2000]. In 80% of the cases with offset introduced in the surface reflectivity, the retrieval procedure returned the correct aerosol model. In the remaining 20% of the cases a different aerosol type was returned, which results in errors in the single scattering albedo. However, these errors in the single scattering albedo are small (less than 0.01 at all wavelengths).

4.6.3. Instrument errors

The accuracy of the OMI aerosol product is expected to be affected by the following instrument-related factors: radiometric calibration offsets, radiometric calibration scale factors and radiometric noise. Errors in the wavelength registration are neglected, since the algorithm does not rely on spectral features in the spectrum and the data is re-binned in 1 nm wide wavebands.

Two kinds of radiometric errors are considered in this section: additive errors (offsets) and multiplicative errors (scale factor). According to the SRD [*Levelt et al*., 2000], the expected offsets and scale factors are less than 1%. The sensitivity of the retrieval method for these errors was tested by perturbing the input spectra using offsets of 1% or scale factors of 1%, at all wavelengths. This represents a worst case scenario, because the effect will be smaller when for some wavebands a positive and for others a negative offset is applied. The effect on the aerosol optical thickness of an offset of 1% is a rms error of 0.04 at 500 nm, which increases to 0.08 at 330 nm. The effect of a scale factor on the aerosol optical thickness is best expressed in terms of a relative error. For a scale factor of 1.01 a relative rms error of 7% in the aerosol optical thickness was observed, with very little spectral variation.

The effects of radiometric scales and offsets on the single scattering albedo were also tested. For the offset cases, in 75% of the cases the correct aerosol model was returned by the fitting procedure. In the other 25% of the cases a different aerosol type was returned, but the error in the single scattering albedo was less than 0.01 at all wavelengths. For the scale factor, the correct aerosol model was returned in 63% of the cases. The error in the single scattering albedo for the remaining 37% of the cases was less than 0.04 for all wavelengths.

The instrument signal-to-noise ratio of OMI in the wavelength range between 330 and 500 nm is approximately 1000. By adding the individual wavelengths into wavebands, an even higher signal-to-noise is obtained. The effect of a signal-to-noise ratio of 1500 on the retrieved aerosol optical thickness was tested and found to be less than 1%. Hence, the effects of signal-to-noise are very small in comparison with the effects of errors in the radiometric calibration.

4.6.4. Aerosol models

As described in Section 3.3, the retrieval method uses a set of aerosol models, which differ in size distribution, refractive index, and vertical profile. The fitting procedure uses the

information available in the measured reflectance spectrum to choose between the aerosol models. To get an accurate retrieval of the aerosol optical properties, the aerosol models which the algorithm can choose from should cover the variations of the aerosol in the atmosphere. The measured reflectance is then fitted using an aerosol model with a representative size distribution and vertical profile. If there is no representative aerosol model, this will cause errors in the retrieved aerosol optical thickness and single scattering albedo. Here, we will discuss the sensitivity for aerosol size distributions, refractive index, vertical profile and particle shape. For the BL1 aerosol model, a detailed analysis was performed to study the effect of changing the size distribution and refractive index in the forward model. For this study forward model calculations were performed with perturbed BL1 aerosol models, whereas the retrieval procedure was fixed to use the BL1 aerosol model. In the normal retrieval procedure, changes in the size distribution or refractive index are dealt with by different aerosol models, thus by fixing the retrieval type a worst-case scenario is studied.

Size distribution

First, the mode radii were increased by 5%, which resulted in a rms error in the retrieved aerosol optical thickness of 3% at all wavelengths. Increasing the width of the size distributions by 5% has an effect of 12% at all wavelengths. As the refractive index of the particles does not change, changing the mode radii or width of the size distributions by 5% does not have a significant effect on the single scattering albedo.

Refractive index

The sensitivity of the retrieval for the assumed refractive index was tested by perturbing the refractive index of the BL1 model by 0.05 for the real part and by 0.01 for the imaginary part. Changing the real part of the refractive index resulted in errors in the retrieved optical thickness of the order 8 to 15% with larger errors for higher optical thickness. The effect is nearly independent of the wavelength. The error in the single scattering albedo as caused by the perturbation of the real part of the refractive index is of the order 0.01, independent of the wavelength.

The effect of increasing the imaginary part of the refractive index by 0.01 is estimated to be 5 to 10% on the aerosol optical thickness and of the order 0.05 for the single scattering albedo. For both the optical thickness and the single scattering albedo the errors show little spectral variation.

Aerosol height

The effect of absorbing aerosols, such as biomass burning or desert dust aerosols, on the reflectance depends on the aerosol vertical distribution. In the aerosol models, assumptions are made on the aerosol vertical profiles. Sensitivity studies indicate that an error of 1 km in the assumed altitude for the aerosol layer yields a 15-20% error in the retrieved aerosol optical thickness at all wavelengths. In the present setup of the sensitivity analysis, the size distribution and refractive index of the fitted aerosol models are unchanged when changing the vertical profile, therefore the calculated single scattering albedo is insensitive to aerosol layer height.

In the near UV method, the retrieved optical thickness and single scattering albedo depend on the height of the absorbing aerosol layer [*Torres et al.*, 1998]. For non-absorbing aerosols, an uncertainty of ±1 km in the prescribed aerosol layer height produces negligible optical thickness errors (± 2%). However, as aerosol absorption increases, so does the altitude error in optical thickness, which may be as large as 60% for strongly absorbing aerosols. For typical absorbing aerosol conditions, T_0(380 nm)=0.9, optical thickness retrieval errors of about

20% are obtained. For the same aerosol conditions, a ±1 km error on the assumed height produces a single scattering albedo error of ± 0.03. This error increases with increasing aerosol absorption.

Particle shape

It is known that especially for dust aerosols the effects of particle shape are important. For most other aerosol types, the assumption of spherical particles is realistic, firstly because of the processes by which they are formed, and secondly because of the hygroscopic nature of most particles. To assess the non-spherical effect for dust particles both spherical and randomly oriented spheroids particles are used for desert dust models (see Table 4.2). The difference in phase function between spheres and spheroids can be as large as 30 % in the geometries observed by OMI, which will give differences in the same order of magnitude in the retrieved aerosol optical thickness. As it is still subject of scientific debate, no estimate is given for non-spherical effects on the single scattering albedo. Given the large uncertainties for dust due to the shape of the particles, it is important to investigate the difference between using the spherical and using the spheroids dust models during the validation phase.

4.6.5. Error budget

Table 4.6 summarizes the various errors for the aerosol optical thickness and single scattering albedo, as identified in the previous sub-sections. Neglecting the errors associated with cloud contamination and particle shape, the overall accuracy in the aerosol optical thickness is estimated to be of the order 30%. When a pixel is cloud contaminated the error can increase to more than 40%, depending on the amount of contamination and the aerosol optical thickness. The accuracy of the single scattering albedo is estimated to be 0.05 – 0.10. The accuracy of the single scattering albedo is mainly determined by how well the aerosol models can represent the real aerosol.

Validation experiments for the TOMS aerosol optical thickness show that for this product the accuracy is of the order of 30% [*Torres et al.*, 2002]. As the OMI aerosol product is an improvement to the TOMS method, it is expected that the OMI product will be more accurate. The large error estimate can be explained by adding several worst-case scenarios in the error analysis, rather than looking at nominal errors.

Table4.6 Error estimates for aerosol optical thickness and single scattering albedo for various error sources. Errors are rms for 46 Sun/satellite geometries. For further explanation of the errors see text.

Error Source	AOT	SSA	Comments
Cloud Contamination	0.1 - 0.2	0.0 - 0.15	5% cloud contamination
Surface Reflectivity	0.07 - 0.09	<0.01	0.01 error in surface reflectivity
Signal-to-noise<1%	<1%	<1%	S/N 1000
Radiometric offset	0.04 - 0.08	<0.01	Additive error of 1%
Radiometric scale factor	7%	<0.04	Multiplicative error of 1%
Size distribution, mode radius	3%	<0.01	5% increase of mode radius
Size distribution, width	12%	<0.01	5% increase of width
Real part of refractive index	8% - 15%	0.01	increase with 0.05
Imaginary part of refractive index	5 - 10%	0.05	increase with 0.01
Aerosol Height	15 - 20%	0.01 - 0.04	change of 1 km
Particle Shape	?	?	only for desert dust

4.7. Validation

In this section two kinds of validation are considered: algorithm validation and product validation. In algorithm validation synthetic OMI data is used. The results of the algorithm are compared to the 'true' values. These 'true' values are known from the model atmosphere that was used for generating the synthetic data set. The advantage of algorithm validation is that we have full control over the synthetic input data, so that effects of certain errors can be tested separately. The disadvantage is that not all errors can be tested for. In product validation real OMI data is used. The results are compared to other independent measurements of the same quantity, the so-called correlative data set. The advantage of product validation is that it is a true end-to-end validation of the product, involving all possible error sources. The disadvantage is that the correlative data set may have a different coverage, or may not be available at the time of the OMI measurement. Also, product validation depends strongly on the quality of the correlative data set. It is also noted that the main product validation can only be done after the EOS AURA launch.

The scope of this section is to give an overview of the validation plan on a high level. For product validation, all details are given in the AURA Validation Plan [*Froidevaux et al*., 2001].

4.7.1. Algorithm validation

In the Science Requirements Document for OMI-EOS [*Levelt et al.*, 2000] the accuracies for the products are given based on algorithm validation. The algorithm validation is thus important to check whether these requirements are met. Therefore, the synthetic data sets should be as realistic as possible, using a state-of-the-art radiative transfer model and an accurate OMI simulator. For aerosols, it is important that also aerosol size distributions and aerosol vertical profiles not contained in the look-up tables are included in the synthetic data.

The use of two synthetic data sets is foreseen. The first synthetic data set is provided by the algorithm developers of the product. It is a limited data set of which the main purpose is to perform validation of all components of the algorithm. An important part of the error assessment in Section 4.6 was performed using this synthetic data set. The OMI US team leader will provide the second data set. This data set should cover several orbits of synthetic OMI data. With this data set an end-to-end test will be performed. The requirements stated in the Science Requirements Document for OMI-EOS will be checked using this data set. Also, the robustness of the algorithm will be tested.

4.7.2. Product validation

In product validation three phases can be distinguished: the commissioning phase checkout, the core validation and the long-term validation. The commissioning phase checkout will be done for the first months during which the OMI instrument is operational. It will provide a first impression of the quality of the data product. A limited number of correlative data will be used in this phase, covering different parts of the globe.

In the core validation a detailed comparison is done between the data products and correlative data sets. The aerosol retrieval algorithm is based on a large number of assumptions on for example the particle size distribution, refractive indices, surface reflectivity etc.. For this reason it is important to have a campaigns during the core validation in which these assumptions can be verified. These campaigns should include detailed microphysical aerosol measurements, as well as radiative measurements, and should include ground based and airborne platforms. A number of campaigns should be planned in different parts of the world, to be able to check different aerosol source regions. Given the large error that can be caused by particle shape of desert dust, a campaign in a desert dust region is recommended. Besides the campaigns,

extensive use will be made of the AERONET data [*Holben et al.*, 1998]. While lacking the detailed aerosol measurements of campaigns, AERONET stations are well distributed over the globe and they provide data over a long time period. This makes them very suitable for the long term validation of the OMI data product. If possible, AERONET observations should be co-located with LIDAR observations, thus providing observations of both the total column as well as the vertical distribution of the aerosols.

Before launch, the OMI aerosol algorithm may be tested using GOME data. Although the footprint of GOME is very large, which makes it difficult to find cloud-free pixels, there are cases available that can be used for such a pre-launch product validation [e.g., *Veefkind*, 1998; *Veefkind et al.*, 2000].

4.8. Summary and conclusion

This document describes the algorithm developed for aerosol retrieval using the Ozone Monitoring Instrument on EOS-AURA. The algorithm will produce the aerosol optical thickness and single scattering albedo at selected wavelengths in the 330 to 500 nm spectral range, for all OMI pixels free of clouds, ice and snow. For cloud contaminated pixels aerosol indices, which give a qualitative indication of the observed aerosol type, will be produced.

The combined use of visible and UV observations by OMI allows the characterization of different aerosol types in terms of total amount, size and absorptive properties. The derived wavelength-dependent aerosol optical thickness and single scattering albedo are of great scientific value for climate change studies, and a variety of other current research topics.

Two methods are used to determine the aerosol optical thickness and single scattering albedo: multi-wavelength and near UV. The multi-wavelength method uses seventeen wavelengths in the 330 to 500 nm range and relies on spectral surface reflectivity data. This approach is the primary OMI retrieval method over water surfaces, taking advantage of their low albedo in the 330 to 500 nm wavelength range for the spectral characterization of aerosol properties over the oceans. As spectral surface reflectivity of land surfaces in the entire 330-500 nm range may not be available at launch, the near UV method is the primary OMI retrieval technique over land, because of the low value and small variability of ultraviolet surface albedo of all land types. The near UV method uses measurements at 342.5 and 388 nm.

The accuracy of the aerosol optical thickness is estimated to be of the order of 30%, and the accuracy of the single scattering albedo 0.1. Most of the errors are related to uncertainties in the aerosol size distribution, refractive index and layer height, as well as uncertainties in the surface reflectivity and the cloud mask.

Acknowledgements.

The authors specially thank Johan de Haan (KNMI) for his valuable comments and suggestions on the document. They also thank Cristina Robles-Gonzalez and Jolanta Kusmierczyk-Michulec (both TNO-FEL) for their comments. Thanks are also due Brent Holben and the AERONET processing team for the use of the extensive AERONET database in the development of the OMI algorithm and in the validation analysis shown in this document. The DAK radiative transfer code has been made available to us by P. Stammes (KNMI).

4.9. References

Anderson, B.E., W.B. Grant, G.L. Gregory, E.V. Browell, J.E. Collins, G.W. Sachse, D.R. Bagwell, C.H. Hudgins, D.R. Blake, and N.J. Blake, Aerosols from biomass burning over the tropical South Atlantic region: Distribution and impacts, *J. Geophys. Res.*, 101, 24,117-24,137, 1996

Bauman, J., Stratospheric Aerosol Climatology Derived from Satellite Solar Occultation and Infrared Emission Measurements, Phd Thesis, Institute for Terrestrial and Planetary Atmospheres, State University of New York, Stony Brook, 2000

Caudill, T.R., D.E. Flittner, B.M. Herman, O. Torres, and R.D. McPeters, Evaluation of the pseudo-spherical approximation for backscattered ultraviolet radiances and ozone retrieval, *J. Geophys. Res.*, 102, 3881-3890, 1997

Colarco, P.R., O.B. Toon, O. Torres and P. Rash, Determining the UV imaginary part of refractive index of Saharan dust particles from TOMS data and a three dimensional model of dust transport, in press, *J. Geophys. Res.*, 2002

De Haan, J.F., P.B. Bosma, and J.W. Hovenier, The adding method for multiple scattering calculations of polarized light, *Astron. Astrophys*. 183, 371-391, 1987

Deschamps, P.Y,. F.M. Breon, M. Leroy, A. Podaire, A. Brichaud, J.C. Buriez, and G. Seze, The POLDER mission: Instrument characteristics and scientific objectives, IEEE Trans. Geosci. Remt. Sensing, 32, 598-615,1994

Diner, D.J., J.C., Beckert, T.H. Reilly, C.J. Bruegge, J.E. Conel, R. Kahn, J.V., Martonchik, T.P. Ackerman, R. Davies, S.A.W. Gerstl, H.R. Gordon, J-P Muller, R. Myneni, R.J. Sellers, B. Pinty, and M.M. Verstraete, Multiangle Imaging SpectroRadiometer (MISR) description and experiment overview, IEEE Trans. Geosci. Rem. Sensing 36, 1072-1087, 1998

Dubovik O. and M.D. King, A flexible inversion algorithm for retrieval of aerosol optical properties from Sun and Sky radiance measurements, *J. Geophys. Res.*, 105, 20,673-20,696, 1996

Fong, K.W., T.H. Jefferson, T. Suyehiro and L. Walton, Guide to the SLATEC Common Mathematical Library, available at: http://www.netlib.org/slatec/guide, 1993

Froidevaux, L., Douglass, A. (Eds.), Earth Observing System (EOS) Aura Science Validation Plan, Version 0.9, 2001

Gathman, S.G., Davidson, K.L., The Navy Oceanic Vertical Aerosol Model, *NRAD Technical Report 1634,* San Diego, 1993.

Herman, B.M. and S.R. Browning, A numerical solution to the equation of radiative transfer, *J. Atmos. Sci*., 22, 559-566, 1965

Herman, J.R. and E. Celarier, Earth surface reflectivity climatology at 340 and 380 nm from TOMS data, *J. Geophys. Res.*, 102, 12,059-12,076, 1997

Holben B.N., T.F. Eck, I. Slutsker, D. Tanré, J.P. Buis, A. Setzer, E. Vermote, J.A. Reagan, Y. Kaufman, T.Nakajima, F. Lavenu, I. Jankowiak, and A. Smirnov, AERONET - A federated instrument network and data archive for aerosol characterization, *Rem. Sens. Environ.*, 66, 1-16, 1998

Hsu, C.N., J.R. Herman, P.K. Bhartia, C.J. Seftor, O. Torres, A.M. Thompson, J.F. Gleason, T.F. Eck, and B.N. Holben, Detection of biomass burning smoke from TOMS measurements, *Geophys. Res. Letters., 23*, 745-748, 1996.

King, M.D., Y.J. Kaufman, D. Tanre, and T. Nakajima, Remote Sensing of Tropospheric aerosols from Space: Past, present and future, *Bull. Am. Meteorol. Soc*,. 80, 2229-2259, 1999

Levelt, P.F., and co-authors, Science Requirements Document for OMI-EOS, RS-OMIE-KNMI-001, Version 2, ISBN 90-369-2187-2, 2000

Koelemeijer, R.B.A., J.F. de Haan, and P. Stammes, A database of spectral surface reflectivity in the range 335-772 nm derived from 5.5 years of GOME observations, *J. Geophys. Res.*, accepted, 2002

Mishchenko, M.I., I.V. Geogdzhayev, B. Cairns, W.B. Rossow, and A.A. Lacis, Aerosol retrievals over the ocean by use of channels 1 and 2 AVHRR data: sensitivity analysis and preliminary results, *Appl. Opt.*, 38, 7325-7341, 1999

Mishchenko, M.I., and L. D. Travis, Capabilities and limitations of a current FORTRAN implementation of the T-matrix method for randomly oriented, rotationally symmetric scatterers, *J. Quant. Spectrosc. Radiat. Transfer*, vol. 60, 309-324, 1998

Nakajima, T., and A. Higurashi, A use of two-channel radiances for an aerosol characterization from space, *Geophys. Res. Lett.*, 25, 3815-3818, 1998

More, J.J., The Levenberg-Marquardt algorithm: implementation and theory. In Numerical Analysis Proceedings (Dundee, June 28 - July 1, 1977, G. A.Watson, Editor), *Lecture Notes in Mathematics 630*, Springer-Verlag, 1978.

Robles-Gonzalez, C., J.P. Veefkind and G. de Leeuw , Mean aerosol optical depth over Europe in August 1997 derived from ATSR-2 data. Geophys. Res. Lett. 27, 955-959, 2000

Sinyuk A., O. Torres , and O. Dubovik, Imaginary refractive index of desert dust using satellite and surface observations, submitted, *Geophys. Res. Letters.,2002*

Sokolik, I., A. Andronova, and T.C. Johnson, Complex refractive index of atmospheric dust aerosols, *Atmos. Environ*., 27(A), 2495-2502, 1993

Stammes, P., J.F. de Haan, and J.W. Hovenier, The polarized internal radiation field of a planetary atmosphere, *Astron. Astrophys*. 225, 239-259, 1989

Stammes, P., Spectral radiance modelling in the UV-Visible range, in*: IRS 2000: Current problems in Atmospheric Radiation*, pp 385-388, Eds. W.L. Smith and Y.M. Timofeyev, A. Deepak Publ., Hampton (VA), 2001

Stowe L.L., A.M. Ignatov and R.R. Singh, Development, validation and potential enhancements to the second generation operational aerosol product at the National Environmental Satellite, Data and Information Service of the National Oceanic and Atmospheric Administration, *J. Geophys. Res*., 102, 16923-16934, 1997

Tanré, D, Herman, M., Kaufman, Y.J., Information on aerosol size distribution contained in solar reflected radiance, *J. Geophys. Res.*, 101, 19,043-19,060, 1996.

Torres, O., P.K. Bhartia, J.R. Herman, Z. Ahmad and J. Gleason, Derivation of aerosol properties from satellite measurements of backscattered ultraviolet radiation, Theoretical Basis, *J. Geophys. Res*.,103, 17099-17110, 1998

Torres, O., J.R. Herman, P.K. Bhartia and A. Sinyuk, A long term record of aerosol optical thickness from TOMS observations and comparison to AERONET measurements, , *J. Atm. Sci., 59, 398-413,* 2002

Vasilkov, A., N. Krotkov, J. Herman, C. McClain, K. Arrigo and W. Robinson, Global mapping of underwater UV irradiances and DNA weighted exposures using Total Ozone Mapping Spectrometer and Sea-viewing Wide Field-of-view Sensor data product, *JGR,* Vol 16-C11, 27,205-27,219, 2001.

Veefkind, J.P., G. de Leeuw, and P.A. Durkee, Retrieval of Aerosol Optical thickness over Land using two-angle view Satellite Radiometry during TARFOX, *Geophys. Res. Lett.*, 25, 3135-1338, 1998

Veefkind, J.P., G. de Leeuw, P.A. Durkee, P.B. Russell, P.V. Hobbs,, and John M. Livingston, Aerosol Optical thickness Retrieval using ATSR-2 and AVHRR data during TARFOX, *J. of Geophys. Res*., 104, 2253-2260, 1999

Veefkind, J.P., G. de Leeuw, P. Stammes and R.B.A. Koelemeijer. Regional distribution of aerosol over land derived from ATSR-2 and GOME. *Remote sensing of the Environment*, 74 , 377- 386, 2000

Vermote, E.F., D. Tanré, J.L. Deuzé, M. Herman and J-J Morcette, Second Simulation of the Satellite Signal in the Solar Spectrum, 6S: An Overview, *IEEE Trans. Geosc. and Rem. Sens.*, Vol 35-3, 1997

Vermote, E.F. and Vermeulen, A. Atmospheric correction algorithm: Special reflectances (MOD09), ATBD version 4.0, available at: http://modis-land.gsfc.nasa.gov/mod09/, 1999

5. OMI Surface UV Irradiance Algorithm

N.A. Krotkov, Goddard Earth Sciences and Technology Center /UMBC
J. Herman, P.K.Bhartia,NASA/GSFC
Colin Seftor, Raytheon ITSS Co
A. Arola, J. Kaurola, P. Taalas, FMI
A. Vasilkov, SSAI

5.1. Introduction

5.1.1. Importance

Global increases in UV-B fluxes from decreasing stratospheric ozone amounts caused by anthropogenic chlorine releasing gases (mostly chlorofluorocarbons) have been an issue of public concern for the past 20 years. Changes in UV fluxes at the Earth's surface due to changes of atmospheric ozone content [*WMO98,* 1999] may strongly affect human health, as well as terrestrial and aquatic ecosystems [*SCOPE* 1992, 1993*; Smith et al.*, 1992*; UNEP*, 1995*; Weiler and Penhale,* 1994*; Mora et al.,* 2000]. According to the UNEP [1995] report, a 10% stratospheric ozone reduction will induce about one million new cases of blindness due to cataracts. At the latitudes of middle Europe (50^{o}N), the change has been about 4% - 6% since 1979. Increased UV radiation may also cause a reduction in crop productivity, and it has been suggested that increased UV fluxes may lead to an increase in the rate of nonmelanoma skin cancer [*Leffell and Brash,* 1996]. In addition to ozone changes, there appear to have been long-term decreases in cloudiness in some regions that can lead to increases in both UV-A and UV-*B [Herman et al.,* 2001].

5.1.2. Review of concurrent satellite UV flux algorithms

Several satellite-based methods for estimating surface UV irradiance, *E*, have been previously suggested [*Frederick and Lubin,* 1988*; Madronich,* 1992*; Eck et al.,* 1995*; Herman et al.,* 1996*; Meerkoetter et al.,* 1997*; Krotkov et al.,* 1998*; Lubin et al.,* 1998*; Mayer et al.,* 1998*; Herman et al.,* 1999*; Li et al.,* 2000*; Matthijsen et al.,* 2000*; Verdebout* 2000*; Krotkov et al.,* 2001, 2002*; Arola et al.,* 2002a]. The common approach involves estimation of a clear-sky surface irradiance, E_{clear}, which is adjusted to actual surface irradiance by using a satellite-derived cloud/aerosol transmittance factor, C_T :

$$E_{cloud} = E_{clear} C_T \qquad [\,5\text{-}1\,]$$

Several methods have been suggested to correct satellite estimated clear-sky UV irradiance for the effect of cloudiness [*Lubin et al.,* 1994*; Eck et al.,* 1995*; Lubin and Jensen* 1995*; Meerkoetter et al.,* 1997*; Rublev et al.,* 1997*; Lubin et al.,* 1998*; Peeters et al.,* 1998*; Li et al.,* 2000*; Matthijsen et al.,* 2000*; Verdebout,* 2000]. These include multi-instrument approaches or using UV reflectance channels of satellite ozone measuring instruments. High resolution (~1 km) visible reflectance data from the Advanced Very High Resolution Radiometer (AVHRR) instruments aboard NOAA weather polar orbiting satellites were used (in combination with external ozone data) to calculate UV maps for several geographical areas: Germany [*Meerkoetter et al.,* 1997], Antarctic Peninsula [*Lubin et al.,* 1994], and Moscow region, Russia [*Rublev et al.,* 1997]. Matthijsen et al. [2000] have used composite cloud data accumulated by International Satellite Cloud Climatology Project (ISCCP) [*Rossow and Schiffer,* 1991] to

estimate spatially averaged cloud reduction over Europe in 1993-1994. Verdebout [2000] has proposed to use both satellite (GOME, Meteosat) and ancillary data to generate surface UV maps over Europe with a spatial resolution of 0.05^o, and potentially on a half-hour basis. Another approach is to combine the TOMS ozone data with shortwave cloud reflectance measurements from the NASA's Earth Radiation Budget Experiment (ERBE) [*Lubin et al.,* 1998]. Since the cloud transmittance is spectrally dependent and can be modified by aerosols [*Erlick et al.,* 1998], estimation of UV transmittance based on visible (i.e. AVHRR, geostationary satellites) or shortwave reflectance (i.e. ERBE) data is not straightforward. In addition, such methods are susceptible to other uncertainties (i.e. water vapor absorption).

5.1.3. OMI UV Algorithm heritage

A more direct approach is to use the UV reflectivity derived from the 360 nm or 380 nm channels of ozone-measuring instruments. The method has been successfully applied for TOMS data [*Eck et al.,* 1995*; Herman et al.,* 1996*; Mayer et al.,* 1998*; Herman et al.,* 1999*; Li et al.,* 2000*; Krotkov et al.,* 2001], Global Ozone Monitoring Experiment (GOME) data [*Peeters et al.,* 1998] and demonstrated for SBUV data [*Frederick and Lubin,* 1988]. Frederick and Lubin [1988] suggested the use of reflectivity from the Solar Backscatter Ultraviolet (SBUV) instrument to derive average transmittance through clouds (SBUV FOV ~170 km by 170 km). Eck et al. [1995] used the higher spatial resolution TOMS data and obtained good comparisons with ground-based UV observations for snow-free conditions using a simple cloud correction method based on TOMS-derived reflectivity at 360 nm.

Because of long time record (since 1978) and global contiguous spatial coverage, the TOMS data are vital for estimating global trends in surface UV irradiance [*Madronich,* 1992*; Lubin and Jensen,* 1995*; Herman et al.,* 1996]. Using total ozone and 360 nm reflectivity measurements from the TOMS instrument aboard the Nimbus-7 satellite, Herman et al. [1996] have estimated the zonal average trends in surface UV irradiance between January 1979 and December 1992, without regard to possible effects of aerosols. Statistically significant increases in annual UV exposure were found at latitudes above 40^o in both hemispheres. For example, at 55^oN (UK, Scandinavia, Canada, Russia) the annual average exposure has increased by 6.8%, 8.1%, and 4.3% per decade for DNA, plant and erythemal action spectra, respectively. Follow-on TOMS missions (Meteor-3, ADEOS, Earth Probe) have extended the TOMS UV record to 21 years (with an 18 month gap in 1995-1996). However, no attempt has been made so far to update global UV trends using combined TOMS data records. The record will continue with QuikTOMS and OMI, as the successors to TOMS. The OMI surface UV irradiance algorithm will be shared with future TOMS and GOME UV products. The previous TOMS data record (since 1978) will be re-processed to ensure homogeneity of UV combined data record for the future trend re-analysis. Although using the same UV algorithm, the OMI UV product will benefit from the higher spatial resolution of the OMI instrument compare to TOMS and GOME instruments.

5.2. OMI UV product description

The OMI UV product includes spectral irradiances at 305 nm, 310 nm, 324 nm, 380 nm [$W/m^2/nm$] and erythemally weighted irradiance [mW/m^2] at solar zenith angle corresponding to the center of OMI FOV (Table 5.1). The simulated OMI products derived from TOMS data are shown in Figure 5.1.

Table 5.1 OMI Surface UV Irradiance products

Wavelength	OMI UV product	Units	Biological effect
305 nm	Spectral irradiance	[W/m^2/nm]	DNA damage
310 nm	Spectral irradiance	[W/m^2/nm]	Skin damage
324 nm	Spectral irradiance	[W/m^2/nm]	Photoinhibition
380 nm	Spectral irradiance	[W/m^2/nm]	Effects of aerosols and clouds on UV
290-400 nm Erythemally weighted	Erythemally weighted UV Irradiance	[W/m^2]	Skin damage; × 40 = UV Index (a standardized scale for reporting UV irradiance to the public)

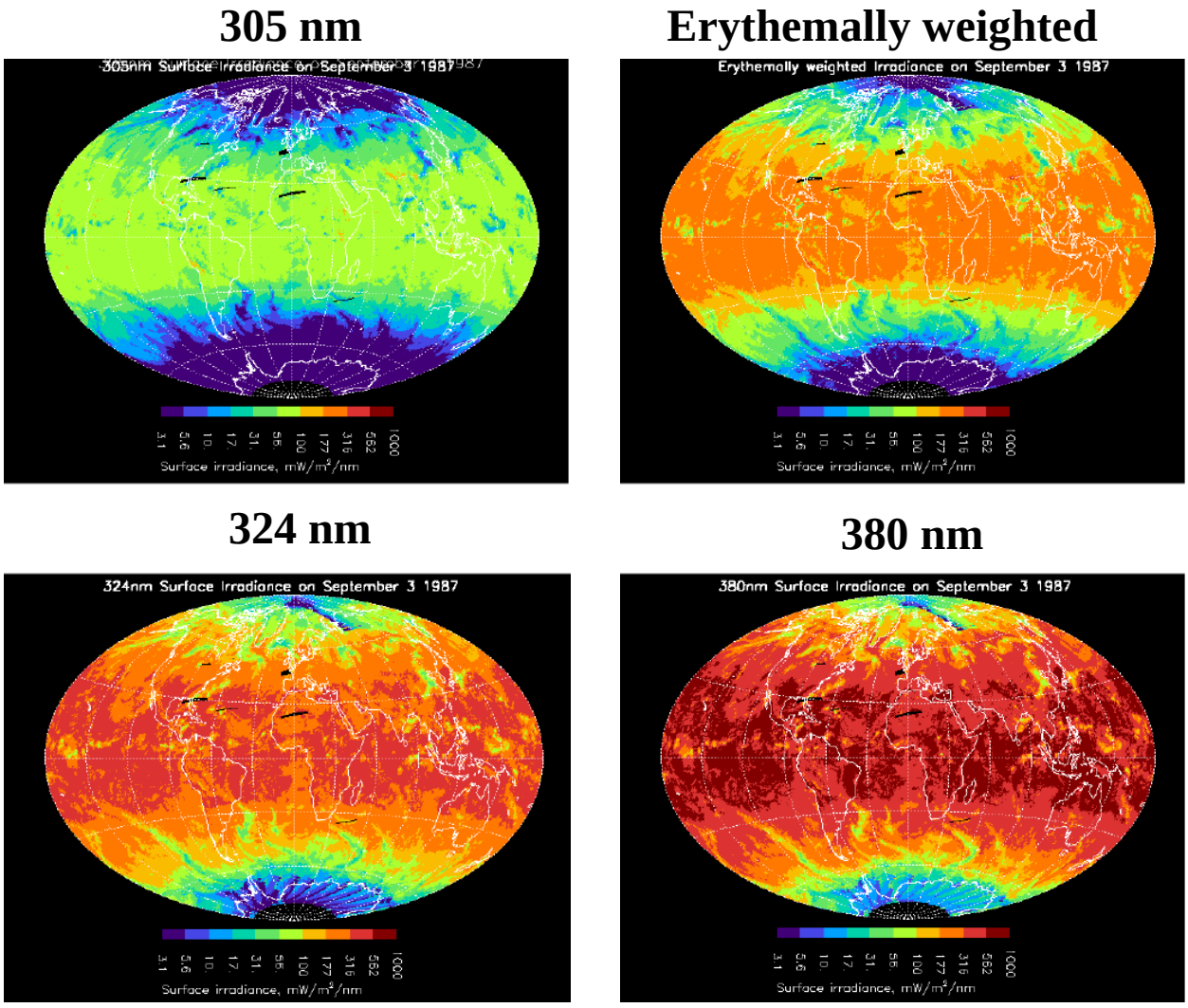

Figure 5.1 Simulated OMI UV products: spectral surface irradiance at 305, 324 nm, 380 nm and erythemally weighted UV irradiance (UV Index). The products were simulated using actual TOMS Level 2 radiances measured on September 3, 1987.

5.3. UV algorithm overview

The amount of ultraviolet radiation in the UVA (320 nm – 400 nm) and UVB (290 nm - 320 nm) spectral ranges that reach the surface of the Earth is determined by Rayleigh scattering from the molecular atmosphere, the absorption of ozone, scattering by clouds, both scattering and absorption by aerosols and reflection from the surface. The algorithm is based on corrections to calculated clear-sky UV irradiance, E_{Clear} The calculation procedure is based on table lookup and either cloud/non-absorbing aerosol correction or absorbing aerosol correction (Figure 5.2). The type of correction is selected based on the two threshold values of the aerosol index (AI) (calculated from 331 nm and 360 nm radiances) and Lambertian Equivalent Reflectivity (LER) (360 nm) as described below. The surface albedo and snow effects are estimated using the TOMS monthly minimum Lambertian Effective surface Reflectivity (MLER) global database [*Herman and Celarier*, 1997].

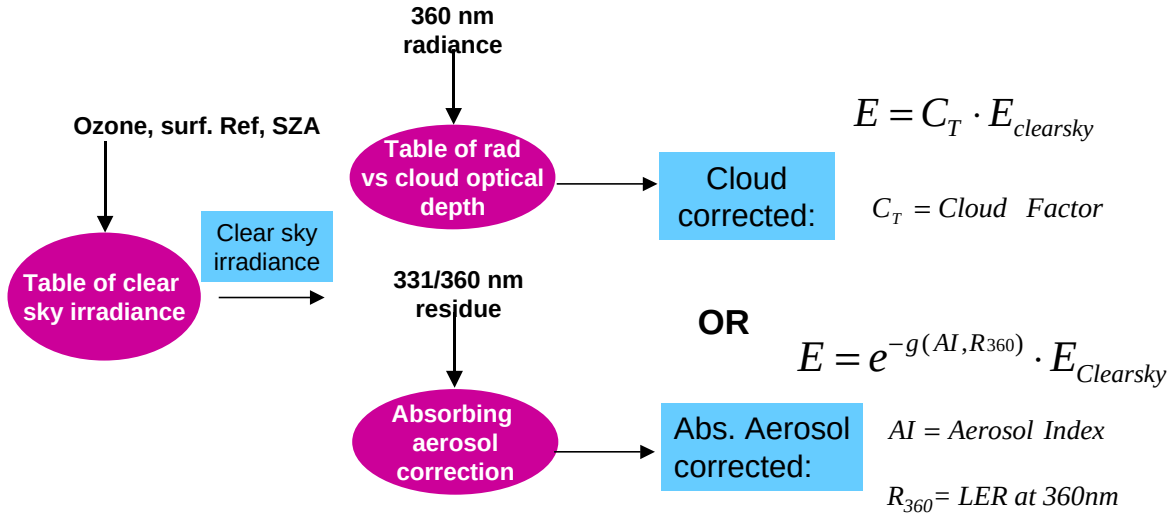

Figure 5.2 OMI UV algorithm overview

5.4. Forward model description

Calculation of E_{clear} in the UV range from satellite-derived spectral extraterrestrial solar irradiance and NASA's Total Ozone Mapping Spectrometer (TOMS) measurements of total column ozone, aerosols and surface reflectivity is described in detail in [*Krotkov et al.*, 1998; *Herman et al.*, 1999], including estimates of the various error sources. In the absence of snow, clouds, and aerosols, the effects of ozone, solar zenith angle, and altitude are essentially well-understood problems. Reduction of UV radiation by absorbing tropospheric aerosols or non-absorbing aerosols and clouds requires an additional correction and is described separately.

5.4.1. Rayleigh plus ozone forward model, $E_{Clear\ sky}$

Under a cloud- and aerosol-free atmosphere with a Lambertian reflecting surface, the surface irradiance, E_{clear} , can be formally expressed as:

$$E_{Clear} = \frac{E_0}{d^2} \frac{E_{dir} + E_{diff}}{1 - A_S S_b} \qquad [5\text{-}2]$$

where E_{dir} and E_{diff} are direct and diffuse irradiances at the ground for unit solar flux and zero surface reflectivity; d is the Sun-Earth distance, and E_o is the extraterrestrial solar flux at 1AU. The factor $(1-A_s S_b)^{-1}$ accounts for the effect of surface reflection, where A_s is the surface albedo and S_b is the fraction of reflected radiation that is, in turn backscattered to the surface by the Rayleigh atmosphere. To calculate the various terms in Equation [5.2], numerical solutions of the radiative transfer equation were obtained in the UV spectral region (290-400 nm) by the auxiliary equations method [*Dave,* 1964], which accounts for all orders of scattering and polarization effects (TOMRAD code). A spherical geometry correction is applied to the direct component and primary scattered radiation (pseudo-spherical correction), which allows accurate calculation of surface flux at solar zenith angles up to 85^o [*Anderson and Lloyd,* 1990]. Tables of solution for E_{dir}, E_{diff} , and S_b were calculated for a climatological set of ozone and temperature profiles, and for selected values of solar zenith angle (θ_o) and 2 terrain pressures (P_t) at full spectral resolution of the measured ozone cross-sections (Master table). The high spectral resolution (~0.05 nm) ozone absorption coefficients are based on the laboratory measurements of *Bass and Paur* [1984] and the Rayleigh scattering coefficients are based on the work by *Bates* [1984].

The climatological temperature and ozone profiles are based on the Nimbus-7 Solar Backscatter Ultraviolet (SBUV) instrument measurements above 15 km and on balloon ozonesonde measurements for lower altitudes [*McPeters et al.,* 1996]. Each standard profile represents a multi-year average for a given total ozone bin for all profiles within a latitude band. These profiles cover a range of 225-475 DU for low latitudes and 125-575 DU for middle and high latitudes, in steps of 50 DU (1 DU = 1 matm-cm or 2.7×10^{16} O_3 molecules/cm^2 under standard temperature and pressure conditions).

5.4.2. Cloudy sky modeling

Bottom of the atmosphere cloud irradiance tables

The cloud correction is based on radiative transfer calculations for a homogeneous, plane-parallel water-cloud model embedded in a scattering molecular atmosphere with ozone absorption [*Krotkov et al.,* 2001]. The optical thickness τ_C is assumed spectrally independent and that cloud phase function corresponds to the C1-cloud model [*Deirmendjian,* 1969]. This cloud model is currently used in the TOMS operational UV algorithm. C_T table is pre-calculated according to Equation [5-1] at 24 wavelengths corresponding to E_{Clear} tables for a wide range of cloud optical depths (0-100), surface albedo (0-1) and solar zenith angles (0-88^o). The cloud height and geometrical thickness is fixed (3 – 5.5 km).

TOA Cloud radiance tables

The same cloud model was used to pre-calculate the angular distribution of the 360 nm radiances at the top of the atmosphere (TOA). We use both DISORT [*Stamnes et al.,* 1988] (for large τ_C, where polarization can be neglected) and Gauss-Seidel code [*Ahmad and Fraser,* 1982] (for $\tau_C < 10$, where polarization can have an effect on TOA backscattered radiances). The algorithm for calculating the effective cloud optical thickness interpolates the TOA radiance cloud lookup tables to fit the measured radiance at 360 nm (after a small Ring and O_2-O_2 corrections). The inferred effective τ_C together with solar zenith angle, surface pressure and surface albedo are used as input parameters to derive the spectral C_T factor from the cloud irradiance tables. The effective cloud optical thickness corresponds to the actual cloud optical thickness only in an idealized case of a homogeneous plane-parallel cloud layer with complete

coverage over OMI FOV. For real inhomogeneous cloud fields, the effective cloud optical thickness becomes a function of the sub-pixel cloud structure and observational geometry (see discussion in section 5.6.2)

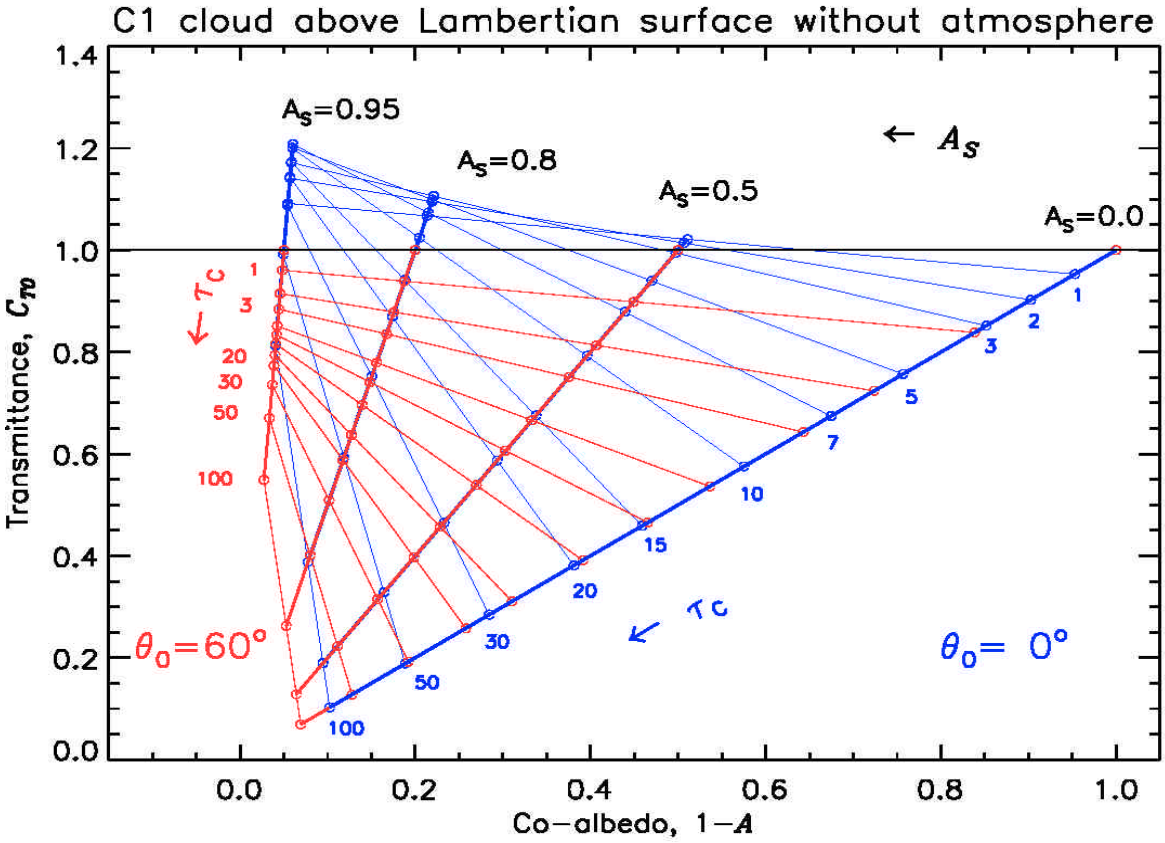

Figure 5.3 *Plane parallel conservative C1 cloud above Lambertian surface: relationship between surface transmittance, C_{T0} and TOA albedo for different combinations of surface albedo, A_S, aloud optical thickness, t_C, and solar zenith angles q_0=0° (blue color) and q_0=60°(red color). Here the abscissa shows the 1-A value and the C_{T0} is plotted on the ordinate. Thick solid lines represent the dependence of C_{T0} and A values on t_C (A_S=const) and thin solid lines represent the dependence on A_S (t_C=const). The solar zenith angle is 60^0, which is a typical value for winter months, when surface albedo substantially increases due to snow. C_T increases with increase in surface reflectivity, but decreases with increase in cloud optical thickness (see [Krotkov et al 2001] for discussion of enhanced cloud transmittance over snow for q_0=0°: C_{T0}>1).*

Properties of C_T

The key features for estimating C_T from satellite reflectance measurements can be understood while neglecting atmospheric effects and angular anisotropy of the radiation (Figure 5.3). Considering a simple model of a homogeneous conservative cloud layer above a Lambertian reflecting surface and neglecting scattering and absorption by atmospheric gases, $C_T = C_{T0}$, can be related to the system (cloud + surface) albedo using energy balance:

$$C_{T0} = \frac{1-A}{1-A_S} \qquad [5\text{-}3]$$

where As is surface albedo and A is top of the cloud albedo.

Over low reflecting surfaces C_{T0} ~(1-A). However, in the presence of snow the relationship between C_{T0} and A becomes more complex (figure 5-3). Generally, increasing surface albedo causes both C_{T0} and A to increase. On the other hand, increasing cloud optical thickness causes C_T to decrease, while A increases (except for enhanced cloud transmittance regime: C_T>1 [Krotkov et al 2001]). Since the slope of C_T dependence on A also increases with increasing surface albedo (Figure 5-3), the C_T becomes increasingly sensitive to small errors in estimating A from satellite radiance measurements. Thus, satellite C_T retrievals become increasingly noisy over bright surfaces. This error is quantified in section 5.6.4.

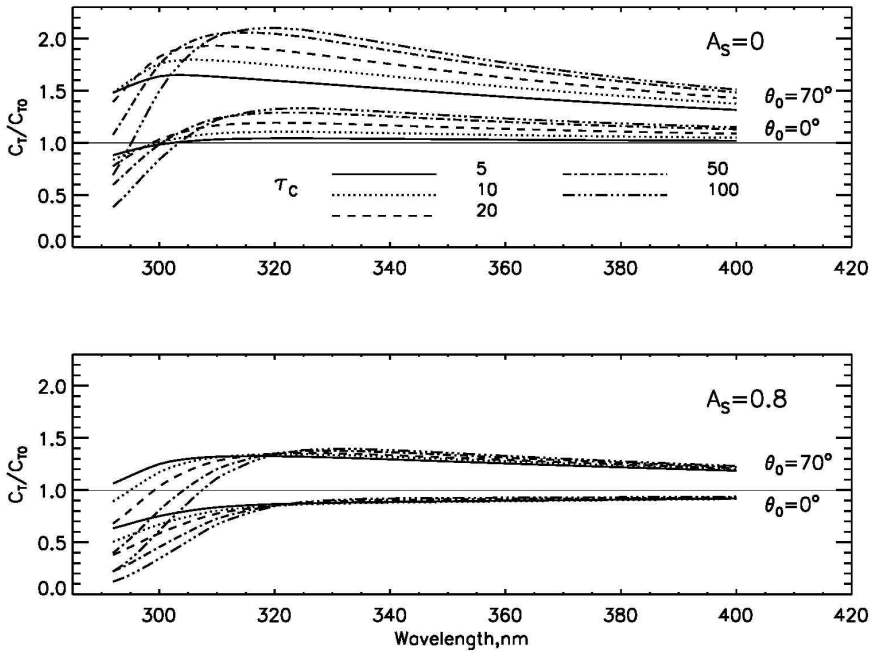

Figure 5-4. Spectral dependence of atmospheric effects on cloud transmittance, C_T/C_{T0}, for solar zenith angles 0^o and 70^o and different cloud optical depths. Zero surface albedo (upper panel) and Lambertian surface with albedo 0.8 (bottom panel). The C1 cloud model embedded into molecular atmosphere (between 3 and 5.5km) assuming 325 DU mid-latitude ozone profile. The atmospheric scattering tends to increase C_T at UVA wavelengths. At short UVB wavelengths absorption by tropospheric ozone has the opposite effect (see Figure 5-5).

The optical thickness of molecular atmosphere is larger in the UV spectral region than in the visible region (τ_R~0.1 at 500nm and τ_R~1 at 300nm) so that the effects of molecular scattering cannot be neglected even for thick clouds. An additional complication arises from the strong spectral dependence of ozone absorption at short UV wavelengths (λ<320nm). Figure 5-4 shows the calculated spectral dependence of the ratio C_T/C_{T0}, where C_{T0} is the cloud transmittance without an atmosphere (see figure 5-3) for a standard 325DU ozone profile. Since our cloud model assumes spectrally independent cloud optical properties, C_{T0} does not depend on wavelength. However, the strong spectral dependence of Rayleigh scattering (~λ^{-4}) and ozone absorption in the UVB spectral region (290nm to 320nm) causes C_T to be spectrally dependent.

The upper panel in Figure 5-4 quantifies the effect for summer conditions, when surface reflection is small and can be neglected. In the UVA spectral region (320nm-400nm), where ozone absorption can be neglected, multiple reflections between the cloud layer and Rayleigh atmosphere above and below the cloud make C_T larger than C_{T0}, similar to reflection from the ground. Unlike the ground reflection, atmospheric backscattering increases at shorter wavelengths. The C_T enhancement is almost independent of the cloud altitude, but increases with solar zenith angle and cloud optical thickness, because of the increase in cloud albedo (Figure 5-3).

At the UVB wavelengths (λ<320nm), tropospheric ozone absorption becomes so strong that it overcomes the effect of Rayleigh scattering and reduces C_T compared to C_{T0}. This reduction gets larger at shorter UVB wavelength due to increase in ozone absorption.

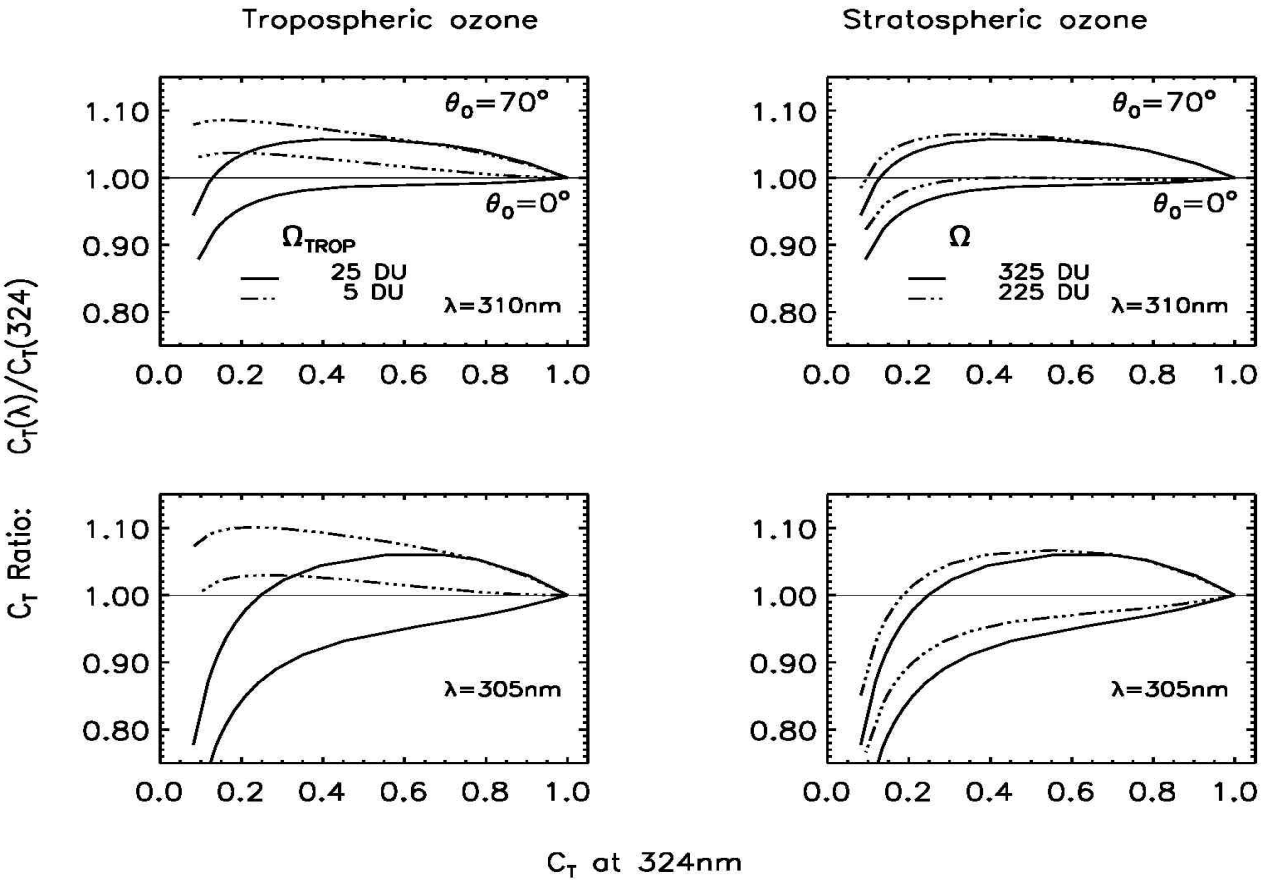

Figure 5.5 CT(l)/CT(324) spectral ratio as a function of CT(324) at the wavelengths 310nm (upper panels) and 305nm (bottom panels). Thick solid lines represent the same atmospheric and cloud models as in figure 5-4. Standard 325DU ozone profile, zero surface albedo, solar zenith angles 0^o and 70^o and different cloud optical depths (0-150, from right to left). On the left panels the dash-dotted lines show the effect of reducing tropospheric ozone from 25DU to just 5DU. On the right panels the dash-dotted lines show effect of reducing stratospheric ozone by 100DU from 325DU to 225DU (tropospheric ozone is the same). Left to right panel comparisons emphasizes much stronger effect of tropospheric ozone on C_T.

Figure 5-5 quantifies the effect of both tropospheric (left) and stratospheric (right) ozone on C_T spectral dependence at UVB wavelengths. The panels on the left show effect of reducing tropospheric ozone in the bottom Umkehr layer (0 to 0.5 atm) from standard amount 25 DU to 5 DU. When tropospheric ozone is drastically depleted the C_T continues to increase due to Rayleigh scattering even at 305nm until the cloud gets optically thick (CT~0.2 corresponds to τ_C~30-50, see Figure 5-3). On the other had, depleting stratospheric ozone by large amount (100DU) has very little effect on C_T.

From the practical point of view, once the C_T is estimated at 360nm it can be calculated at shorter UVB wavelengths using a homogeneous cloud model and an average ozone profile. Therefore, the problem of estimating C_T at all UV wavelengths is reduced to the estimation of TOA albedo at one UVA wavelength, provided the tropospheric ozone and surface albedo are known from independent measurements or climatology. The advantage of this method is that the spectral variation in C_T resulted from Rayleigh scattering above and below the cloud, surface albedo and ozone absorption are explicitly taken into account (Figures 5-3 and 5-4).

The stratospheric ozone correction is easy to apply, while tropospheric ozone correction presents a larger problem (see Volume 2).

5.4.3. Aerosol modeling

For the purposes of estimating UV irradiance at the Earth's surface, there are two major classes of aerosols that must be considered: 1) aerosols that only scatter UV radiation and 2) aerosols that both scatter and absorb UV radiation. The first category is included in the measured scene reflectivity (cloud optical thickness), and attenuates UV radiation in a manner that approximates clouds of equivalent reflectivity. However, since these aerosols decrease the direct solar radiation but increase the diffuse radiation they have relatively small effect on the total surface UV irradiance [Krotkov et al., 1998]. Moreover, satellite UV instruments can see the increase in the reflected radiation and correct for it. Typical attenuation by such aerosols ranges between 1% and 10%. Therefore, we shall describe the aerosol effect on global (direct plus diffuse) UV irradiance by the cloud transmission factor, C_T (see Equation [5.1] and 5.4.2). Although the current UV algorithm does not distinguish between water clouds, haze, ice clouds and non-absorbing aerosols, for a nominal aerosol optical thickness of 0.5 at 360 nm, the error in estimating the C_T by these various sources is ~1% (see section 5.6.2).

By contrast, aerosols that absorb the UV radiation (*dust, smoke and urban aerosols*) attenuate both the direct and diffuse radiation, so the surface UV radiation is more strongly attenuated by such aerosols than by non-absorbing aerosols of the same optical depth. In a study by *Kerr* [1997], variations in UV flux measured on clear days at Toronto with a Brewer instrument were compared with aerosol optical depth (τ_a) measurements made with the same instrument. The analysis found that the dependence of the aerosol C_T on τ_a can be fitted to the exponential expression:

$$C_T = exp(-kt_a) \qquad [5\text{-}4]$$

where k falls in the range 0.2 to 0.3. We use radiative transfer calculations to obtain k factor and correlate with OMI measured radiances for different aerosol models embedded in a Rayleigh atmosphere with ozone. Calculations using the properties of non-absorbing aerosols (*anthropogenic sulfate, maritime aerosols*) confirm that they have small effects on global UV-flux (k<0.15). For UV absorbing aerosols the k factor becomes larger and mainly controlled by the aerosol absorption to extinction ratio determined by the single scattering co-albedo (1-ω). For tropospheric models studied in [*Krotkov et al.,* 1998] the dependence of k on (1-ω) at $\theta_o=30^o$, λ=325 nm and surface pressure 1 atmosphere can be fitted to the expression: $k = 0.1 + 2(1-\omega) - 2(1-\omega)^2 \pm 0.04$. Therefore, absorbing aerosols if detected by OMI should be treated differently than clouds in the C_T calculation (see section 5.5.2)

5.5. Inverse algorithm description

The simplified flow-chart of the OMI UV algorithm is presented in Figure 5.2. Below we describe separate steps in more details.

5.5.1. LER calculation at 360 nm

The first step of the UV algorithm is to calculate the Lambert Equivalent Reflectivity (LER), A_{LER}. The LER is derived from the OMI-measured radiance (I_{360}) near 360 nm. I_{360} can be expressed as a sum of the atmospheric backscatter above a specified Lambertian surface, I_O , and the radiance reflected from this surface [*Dave,* 1978*; Eck et al.,* 1995*; Herman and Celarier* 1997*; Herman et al.,* 2001]:

$$I_{360} = I_0(q, q_0, P_C) + \frac{R_{360} T_{360}(q, q_0, P_S)}{1 - R_{360} S_b(P_S)} \qquad [5\text{-}5]$$

where I_{360} and I_0 are the radiance to solar irradiance ratios, R_{360} is the Lambert Equivalent Reflectivity (LER) at 360 nm, S_b is the diffuse reflection of Rayleigh atmosphere illuminated from below by an isotropic source, θ is the viewing angle, θ_o is solar zenith angle , T_{360} is the total amount of direct plus diffuse radiation reaching the surface, multiplied by the atmospheric transmission of the diffuse reflected radiation in the direction of the satellite, and P_S is the surface pressure. For the wavelengths of interest, *Io*, S_b, and T_{360} are calculated assuming a pure Rayleigh atmosphere with no gaseous absorption and no Mie scattering. A small correction is made for Rotational-Raman scattering, using the procedure described by *Joiner et al.* [1995] and absorption by O_2-O_2 collision complex. We approximate P_S in Equation [5-4] by terrain pressure. This is a reasonable approximation for clear sky scenes, and scenes with broken cloud or thin semi-transparent clouds. For thick clouds, the I_{360} becomes insensitive to the cloud top pressure.

5.5.2. Aerosol Index calculation

OMI measured radiances at 331 nm and 360 nm can be used to correct for absorbing aerosols at a known altitude by forming the aerosol index (AI) [*Krotkov et al.,* 1998*; Herman et al.,* 1999]:

$$AI = -100\ [\ log_{10}(I_{11}/I_{12})_{meas} - log_{10}(I_{11}/I_{12})_{calc}\ ] \qquad [5\text{-}6]$$

where *I* represents the upwelling radiance at the top of the atmosphere and λ1 and λ2 are the shortest and longest available wavelengths in the 0.33-0.40 μm range (where gaseous absorption is negligible). The AI is a dimensionless quantity (one AI unit is equivalent to 2.3 % radiance change and the Nimbus 7 TOMS noise is about 0.2 AI units). Radiative transfer studies indicate that meteorological (water) clouds yield nearly zero AI. For absorbing aerosols they indicate that the AI is positive and increases with increasing aerosol absorption optical depth and aerosol layer height (exception is smoke in the boundary layer that can produce negative AI [Torres et al 1998]). An advantageous AI property is the ability to detect UV-absorbing aerosols in the presence of sub-pixel clouds or over underlying clouds. The OMI UV algorithm uses the AI threshold to select the type of correction applied to the E_{Clear}. We assume that AI is calculated from the 331 nm/360nm wavelength pair (with LER at 360nm).

5.5.3. Surface albedo estimation

Assuming Lambertian surface, the factor $(1\text{-}A_s S_b)^{-1}$ accounts for the surface albedo effect on E_{Clear} (see Equation [5-2]), where S_b is the fraction of reflected radiation backscattered to the surface by the atmosphere and is known from the clear sky irradiance table. The spectral dependence of $S_b(l)$ has a maximum of about 0.4 around 320 nm, with a decrease longward of the maximum (due to decreasing of Rayleigh optical thickness of the atmosphere), and a sharp decrease shortward (due to the spectral enhancement of absorption by tropospheric ozone). For the Earth's surface not covered by ice or snow, A_s typically varies between 0.01 - 0.04 (over land) and 0.05 - 0.08 (over water) [*Herman and Celarier,* 1997]. Direct measurement of A_s by OMI is possible only for cloud and aerosol-free conditions. To estimate A_s in the presence of aerosols and clouds we use monthly minimal Lambertian equivalent 380 nm surface reflectivity (MLER) global database derived from the Nimbus-7/TOMS measurements (1978-1993). We also assume that the surface albedo does not change with wavelength in the UVA and UVB spectral regions. Both assumptions are in reasonable agreement with direct ground-based measurements of UV albedo [*McKenzie et al.,* 1996*;* see also a survey in *Madronich,* 1993]. We

use linear interpolation in space and time between monthly MLER values to estimate MLER on a given day for each OMI FOV.

5.5.4. Snow correction

MLER is a reasonable estimate of the surface albedo for either snow-free conditions or regions with permanent snow cover (Antarctica, Greenland). However, MLER is not a good estimator of actual snow albedo at mid-latitudes in winter season when surface albedo varies daily depending on the presence and thickness of snow cover. In absence of snow information the algorithm uses a climatological snow/ice flag (probability of the presence of snow on a given day at a given location) as does the TOMS algorithm. If snow is detected (or likely), the OMI algorithm first determines a snow albedo threshold (SAT). The SAT is the largest of MLER for a given day and the constant value of 0.4. The value 0.4 was selected as appropriate for snow covered urban/suburban-populated areas containing at least moderate densities of roads, houses, and trees (e.g., Toronto) [*Krotkov et al.,* 2001]. If MLER data for one of the bracketed months are not available we use the other monthly value. If both bracketed MLER values are not available, the algorithm assumes a constant MLER value of 0.7 for high latitudes (more than 65^o) and zero otherwise. The final estimation of A_S is based on a comparison of SAT with the OMI measured LER value at 360 nm (see Equation [5-4]). If LER is less than SAT, cloud free conditions are assumed and A_S is set equal to LER. If LER is larger than SAT, A_S is set equal to SAT and all additional measured reflectivity is assigned to a cloud. The algorithm proceeds to cloud correction calculation as described below.

It was shown that the TOMS method of snow correction could lead to both underestimation and overestimation of UV radiation in winter-spring conditions [*Kalliskota et al., 2000; Kalliskota, 2001; Arola et al., 2002b*].

To obtain a more realistic treatment of the albedo of snow-covered terrain, a new method was developed [*Arola et al., 2002b*]. This method is based on an empirical relation between UV reflectivity and snow depth. To establish such a relation, cloudless days with snow cover were selected based on the total cloud cover and snow depth (SD) parameters from the ECMWF ERA-15 re-analysis dataset (covering time period 1979-1994). These data, together with the coincident and co-located Nimbus-7 TOMS reflectivity measurements, were used to develop a regression models for each ground pixel according to equation:

$$R_{380} = u \times SD^{1/3} \qquad [5\text{-}7]$$

where R_{380} is the measured TOMS reflectivity for a given site on a cloud-free days with snow, SD is the snow water equivalent, and u is a fit parameter, specific to each global grid point. The snow depth information is expected to be available on the same day of the OMI radiance acquisition from the models or other satellites. Then the daily snow albedo, A_S, can be calculated from equation [5-6] using *SD(lat,lon)* and *u(lat,lon)* for each OMI FOV and used (instead of MLER) in satellite-retrieved UV calculation of E_{Clear} (5-2) and C_T.

Figure 5.6 shows comparison of the proposed method with the current MLER algorithm for Sodankyla, Finland and Churchill, Canada. As expected, this method improved the correspondence between the satellite-retrieved results and ground-based measurements, particularly during the melting period in those locations where the regional snow albedo is high

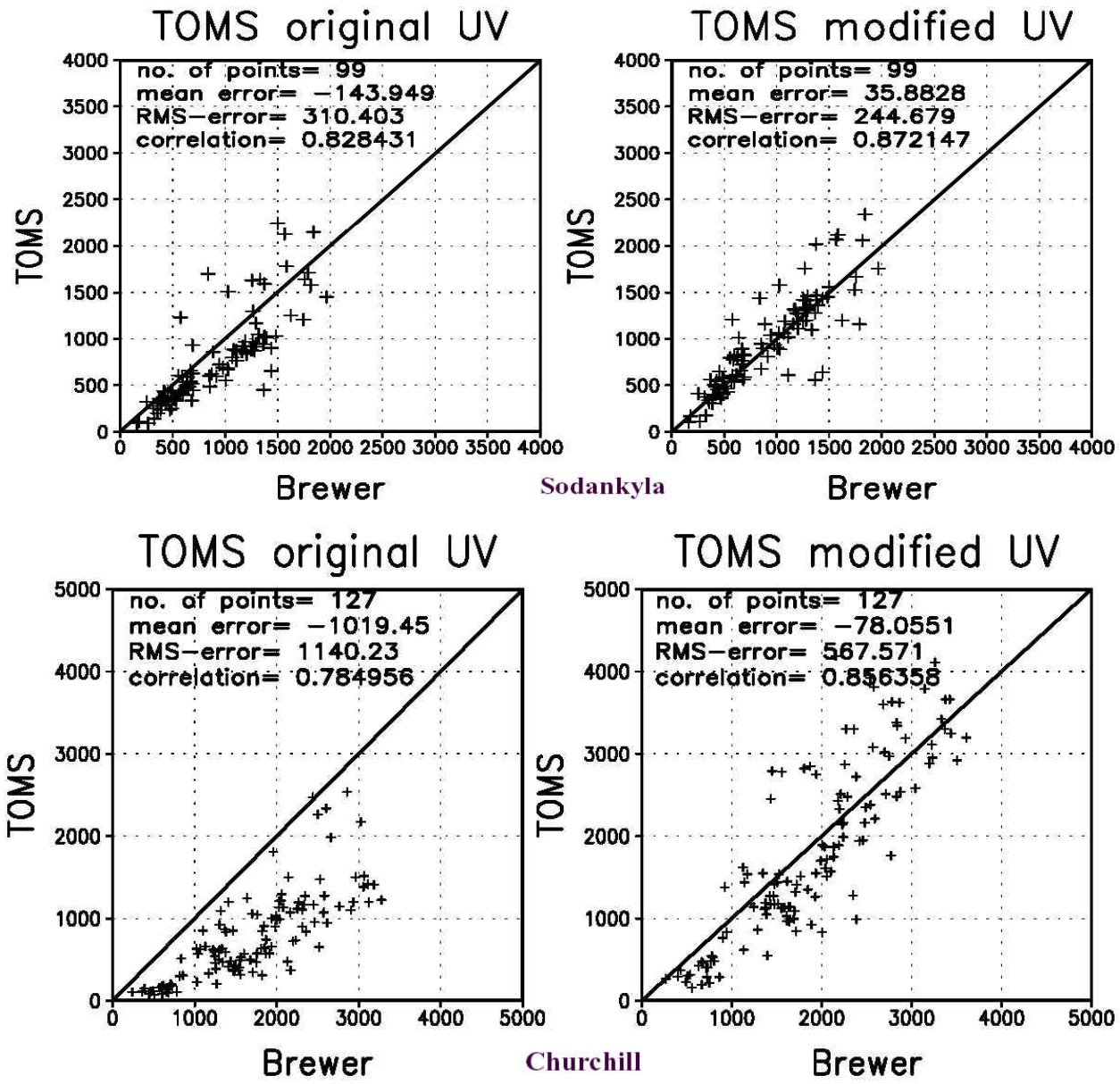

Figure 5.6 *The effect of the new snow albedo treatment on the computed surface UV. "TOMS original UV" is based on MLER [Herman and Celarier, 1997] whereas "TOMS modified UV" is based on the snow albedo regression with ERA-15 snow depth data, and coincident and co-located Nimbus-7 TOMS reflectivity measurements [Arola et al., 2002b]. Top: Comparison at Sodankylä, Finland; bottom: Churchill, Canada*

5.5.5. $E_{Clear\ sky}$ table lookup procedure

Irradiance look-up tables' interpolations (for specific wavelength or for erythemal product) are performed in the following sequence: solar zenith angle interpolations use Lagrange procedure; terrain pressure interpolation is linear with the log of the flux; two fluxes are calculated using two different ozone profile shapes. Since the sensitivity of the surface UV irradiance to the exact ozone and temperature profile shape is small [*Krotkov et al.*, 1998] the simplified profile mixing scheme was implemented for table lookup, which is based only on the latitude of the OMI FOV. The irradiance values were convoluted with a triangular slit function (FWHM=0.55 nm) centered at 305, 310, 324, 380 nm and 22 additional wavelengths to create a

working set of tables. These were then used as lookup tables for calculations of E_{clear} (see Equation [5.2]). Finally the surface albedo correction and sun distance correction are applied according to Equation [5-2]. The flow chart of the table interpolation is presented in Figure 5.7.

5.5.6. Cloud/non-absorbing aerosol correction

In OMI UV algorithm non-absorbing aerosols and clouds are treated similarly. Cloud fraction and cloud optical thickness cannot be simultaneously derived on the basis of one OMI radiance measurement (the OMI instantaneous FOV is 13 × 24 km^2). To estimate the cloud transmittance at the overpass time, $C_T(t_0)$, we use the homogeneous cloud model embedded into Rayleigh scattering atmosphere with known surface albedo, A_S. The "effective" cloud optical thickness, $t_C(t_0)$, is derived by matching the measured 360 nm radiance at the overpass time, t_0, with the calculated radiance for each OMI FOV. The same cloud model is used to calculate the C_T as a function of t, A_S, and solar zenith angle,θ_0, at all UV wavelengths:

$$C_T(l,t_0) = C_T(l,t_C(t_0),A_S,q_0(t_0)) \qquad [5\text{-}8]$$

The spectral independence of t_C for pure cloud scattering is an accepted approximation in the near UV spectral region (300-400 nm), and was confirmed by Mie calculations. The OMI UV algorithm also neglects the spectral dependence of A_S, which is less than 0.05 over both land and ocean in the UVA and UVB spectral regions (300-400 nm). Even with spectrally independent t_C and A_S, the method accounts for the spectral dependence of C_T that results from reflection between the cloud and the Rayleigh atmosphere and ozone absorption, as well as multiple reflections between the cloud and the surface. The second effect is especially important for snow-covered surface. To calculate daily exposure the diurnal variation of $C_T(l,t)$ is estimated from changes in solar zenith angle, assuming a fixed value of cloud optical thickness : $t(t) = t(t_0)$.

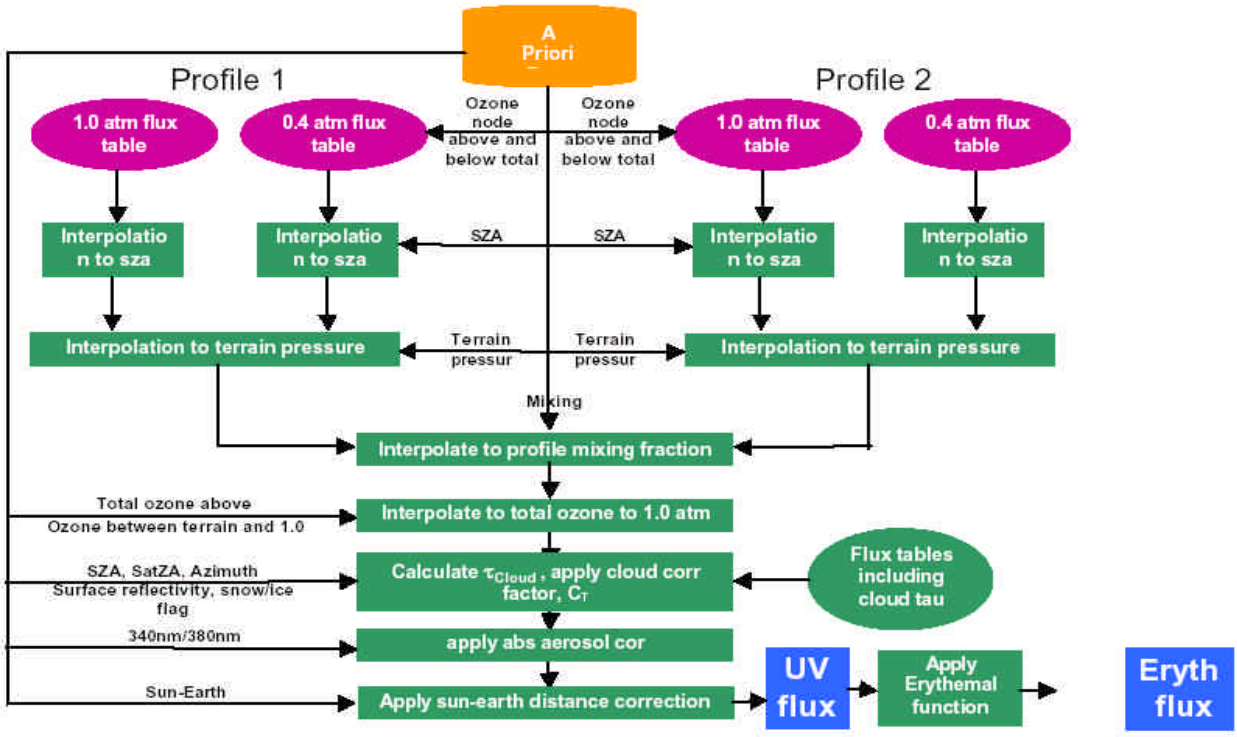

Figure 5.7 OMI UV table interpolation flow-chart

5.5.7. Correction for absorbing aerosols

Aerosols that absorb the UV radiation attenuate both the direct and diffuse radiation, so the surface UV radiation is more strongly attenuated by such aerosols than by non-absorbing aerosols of the same optical depth. Moreover, since these aerosols also attenuate the outgoing radiation, the satellite algorithms that treat these aerosols as non-absorbing underestimate their optical depth, amplifying the error further, causing overestimation of UV irradiance. Though satellite UV instruments can detect such aerosols when the conditions are right (absence of clouds, large elevated plumes at known altitude, see section 4 for more details), they typically miss them when the aerosols are located mostly in the planetary boundary layer. A correction scheme for the former aerosol types is described below.

When the absorbing aerosol plumes are transported into the free troposphere, they absorb the diffuse radiation emanating from lower altitudes and reaching the satellite. Since the diffuse radiation, produced largely by molecular scattering, is a strong function of wavelength, the effect of such aerosols also varies with wavelength. In its simplest form they cause the satellite-derived LER to decrease with decrease in wavelength, which can be used to detect the presence of such aerosols. (By contrast non-absorbing aerosols typically cause the LER to increase with decrease in wavelength, though this effect is usually quite small). This is the basis for deriving the TOMS Aerosol Index (AI) [5-5]. Using this AI one can construct a simple absorbing aerosol correction (AAC) algorithm [*Krotkov et al., 1998; Herman et al., 1999*], as follows:

$$\frac{E_{aerosol}}{E_{Clear}} = e^{-g(H_A)AI} \qquad [5\text{-}9]$$

where conversion factor g is a function of aerosol height, H_A, observational geometry and aerosol type. Radiative transfer calculations show that for the same altitude g factor is smaller for dust aerosol than for biomass burning smoke. Without discrimination between dust and smoke aerosol types a compromise value of g=0.25 was recommended as a first order correction for tropical regions [*Krotkov et al., 1998*]. This value will be refined based on dust versus smoke discrimination techniques (see section 5.6.4). Currently TOMS aerosol algorithm employs geographical approach for such discrimination, because the TOMS aerosol channels in the 330nm-380nm range are not sufficiently separated to allow enough spectral contrast between these two aerosol types *[Torres et al., 2002*]. Combining UV and visible wavelengths (see Chapter 4 for details) will increase the information content of aerosol measurements from OMI.

An example of the monthly mean UV irradiance attenuation due to absorbing aerosols is shown in Figure 5.8. The strongly absorbing aerosols are confined mostly to the tropical regions. In the regions (Africa, South America, and Middle East) where large amounts of absorbing aerosols are present (dust and smoke) the reduction in UV irradiance frequently exceeds 50 ± 15% (see error analysis in Section 5.6.4) of the clear-sky value. In some instances, such as the Indonesian fires during September 1997, the reduction is greater than 90% [*Herman et al.*, 1999].

5.5.8. Switching between cloud/non-absorbing and absorbing aerosol corrections

Either cloud or absorbing aerosol correction is applied for each OMU FOV. The choice between these two alternative techniques is based on the threshold values of LER (Equation [5.4]) and AI (Equation [5.5]). Currently the AI technique (Equation [5.8]) is applied only if AI>0.5 and LER<0.15 (Figure 5.5). In the future a more complicated discrimination technique could be developed based on the OMI aerosol and cloud products (see this Volume).

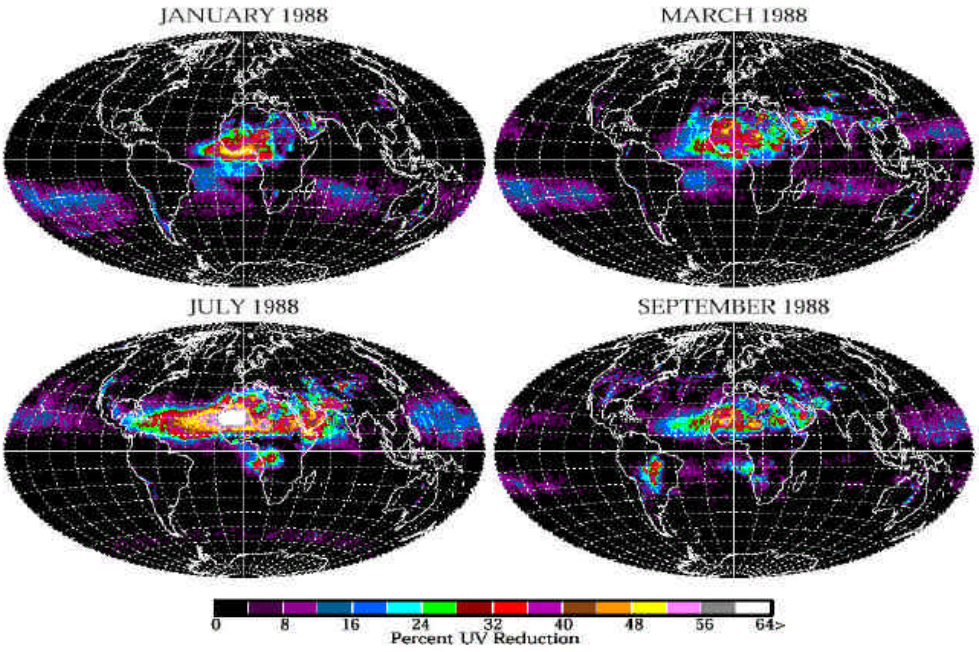

Figure 5.8 Absorbing aerosol correction applied instead of cloud correction for strongly absorbing aerosols (AI>0.5) in the free troposphere for quasi-clear conditions (LER<0.15)

5.6. Error analysis and budget

The error budget is estimated for a single OMI pixel assuming horizontally homogeneous scene. The effects of sub-pixel inhomogeneity are not considered and should be a subject of a separate study (see UV validation requirements later). The noise in OMI radiance measurement is considered to be much smaller than retrieval errors due to uncertainties in atmospheric model. We assume that these atmospheric uncertainties vary randomly in space and time, so their combined effect is greatly reduced in Level-3 UV product (zonal and/or monthly means). Since the variability of the extraterrestrial solar irradiance with time (over solar cycle) is much smaller than its absolute uncertainty, the accuracy of derived UV trend can be much higher than the accuracy of the absolute irradiance. However, predicting trend uncertainty is beyond the scope of this ATBD, which describes Level 2 UV products.

The OMI surface irradiance, E, is estimated as a product of extraterrestrial solar irradiance,E_0, clear sky surface irradiance, E_{Clear}, and cloud/aerosol transmission factor C_T (equations (5-1) and (5-2)). Assuming that fractional errors in these three quantities are uncorrelated, the fractional error on E is simply related to the fractional errors on E_0, E_{Clear} and C_T :

$$\left(\frac{s_E}{E}\right)^2 = \left(\frac{s_{E0}}{E_0}\right)^2 + \left(\frac{s_{E_{Clear}}}{E_{Clear}}\right)^2 + \left(\frac{s_{CT}}{C_T}\right)^2 \qquad [\,5\text{-}10\,]$$

5.6.1. Error budget for E_0

The two UV solar spectrometers on NASA's Upper Atmospheric Research Satellite (UARS) (Solar Stellar Irradiance Comparison Experiment (SOLSTICE) [Rottman et al., 1993]

and the Solar Ultraviolet Spectral Irradiance Monitor (SUSIM), [Brueckner et al., 1993]) have made daily irradiance measurements since October 1991, a period of time including most of the decrease from the maximum of solar cycle 22 to solar minimum. Daily UV solar spectral irradiances measurements were also made by the Solar Backscatter Ultraviolet /model 2 (SBUV/2) instrument onboard the NOAA-11 satellite between February 1989 and October 1994 [DeLand and Cebula 1997]. These three independent instruments have shown that the variability of the solar flux (11-year and 27-day) is less than 1% in the near UV region (290 nm - 400 nm). The variation of solar flux with Sun-Earth distance d (about ±3.5% during an annual cycle) is accounted for in equation (5-2).

The absolute accuracy of E_0 measurements is maintained through internal calibrations and data set intercomparisons (between SOLSTICE, SUSIM, and SBUV/2 instruments). The measurements by the two UARS instruments were compared with the same-day measurements by three other solar instruments (the Solar Spectrum (SOLSPEC), the Shuttle Solar Backscatter Ultraviolet (SSBUV) and the Shuttle SUSIM instruments) during the ATLAS-1 ATLAS-2 and ATLAS-3 Space Shuttle missions in March 1992, April 1993 and 1994, respectively (Cebula et al., 1996; Woods et al., 1996). In the 290-400 nm region, at 5 nm spectral resolution, the difference between the various data sets is less than ±3% and is wavelength dependent. Cebula et al. (1996) noted that at 1 nm resolution, small errors in wavelength registration could lead to larger differences between instruments near the vicinity of strong solar absorption features. This problem is exacerbated at higher spectral resolutions. We assume ±3% as a conservative estimate of the absolute solar irradiance uncertainty and include it in the final error budget.

5.6.2. Error budget for E_{Clear}

The accuracy for estimating E_{clear} is dominated by the uncertainty of the input geophysical parameters**:** total column ozone amount **Ω**, the surface pressure and reflectivity. Other less sensitive but important parameters include: ozone vertical distribution, boundary layer ozone and SO_2 [*Krotkov et al.*, 1998]. Table 5.2 summarizes rms errors for estimating UV irradiance at cloud and aerosol-free conditions, E_{Clear} with and without E_0 uncertainty.

5.6.3. Error analysis for cloud/aerosol correction factor, CT

This section quantifies uncertainties in estimating average cloud/aerosol transmittance within OMI footprint due to variations in cloud or aerosol parameters. The strategy of the C_T error analysis is as follows: we model the TOA reflectance and cloud transmittance (true C_T) for different cloud/aerosol scenarios. Next, we use this TOA reflectance as input to the OMI UV code to infer the effective cloud optical thickness and estimate C_T error at different geometries and wavelengths. Finally, we treat various uncertainties in cloud/aerosol models as random uncorrelated errors. As to specific atmospheric scenarios we first consider variations in cloud model (cloud shapes error, changing drop size distribution, cloud height and cloud fraction), following by errors due to the presence of non-absorbing aerosols. The error analysis of episodic events of UV absorbing aerosols due to urban pollutions, biomass burning and desert dust is considered in section 5.6.4. The error analysis for clouds over snow is given in section 5.6.5. Table 5.5 summarizes OMI UV product uncertainties for different atmospheric scenarios.

Table 5.2 Estimated errors in clear sky surface irradiance E_{Clear} at solar zenith angle 50^O. The table concerns only cloud- and aerosol-free cases and gives lower limits of the uncertainties for horizontally homogeneous scenes over an OMI footprint (13 km ´ 24 km at nadir). The effects of subpixel variability within OMI footprint are not considered.

Error source	**305nm**	**310nm**	**324nm**	**380nm**
Forward RT model [2)]	1%	0.5%	0.3%	0.1%
Total Ozone (2% rms)	4%	2%	0.1%	0
Surface albedo snow/ice-free,1% rms (*snow/ice, 5% rms)	0.2% (1.5%)	0.4% (2.0%)	0.4% (3.0%)	0.2% (1.5%)
Strat. profile ($1/4^{th}$ of high-low difference)	1.5%	0.7%	0%	0%
Trop. profile (5 DU rms)	1%	0.5%	0%	0%
Surface pressure (±10mb)	0.8%	0.7%	0.5%	0.2%
Total rms in E_{Clear}	4.6% (4.8%)	2.3 (3%)	0.7% (3%)	0.2% (1.5%)
Total rms (including solar flux ±3% error)	5.5% (5.7%)	3.8% (4.3%)	3.1% (4.3%)	3% (3.4%)

1) *Error in erythemally weighted irradiance is approximately the same as 310nm error;*
2) *Intercomparisons of radiative transfer codes (TOMRAD [Dave 1961, OMI ATBD volume 2], DISORT code and University of Arizona code) for identical input conditions. The differences result mainly from the way different codes divide atmospheric column into computational layers and approximate scattering and absorption properties of each layer.*
3) *We assume there is no other UV absorbing gases (SO_2, NO_2) present;*
4) *We use the same ozone cross-sections as OMI ozone algorithm. The cross-section uncertainty is implicitly included in 2%. total ozone uncertainty (see volume 2).*
5) *Numbers in parenthesis apply to snow/ice conditions for horizontally homogeneous snow surfaces with A_s >0.9 (Antarctica, Greenland) assuming 5% uncertainty in snow albedo due to Lambertian assumption (see section 5.6.4); Figure 5.15 quantifies irradiance sensitivity to the surface albedo (see dashed line for clear sky conditions);*
6) *E_{Clear} sensitivity to total ozone, ozone profile, tropospheric ozone and surface pressure is quantified in [Krotkov et al., 1998];*
7) *Errors are similar at smaller solar zenith angles $q_o < 50^o$. However, at lager $q_o > 70^o$ and wavelengths shorter than 310nm strong dependence of the surface UV irradiance on ozone profile shape increases E_{Clear} uncertainty to more than 30% [Krotkov et al., 1998].*

Cloud shape error

The homogeneous cloud model described in 5.4.2 ignores the real 3-dimensional (3D) cloud structure and some related cloud-radiation effects (cloud shadows, reflection from non-horizontal surfaces). These effects are difficult to estimate because of large subpixel variability in cloud amount, shapes and layering. One attempt has been previously made to model fair-weather cumulus cloud fields using a Monte-Carlo radiative transfer code [*Geogdzhaev et al.,*

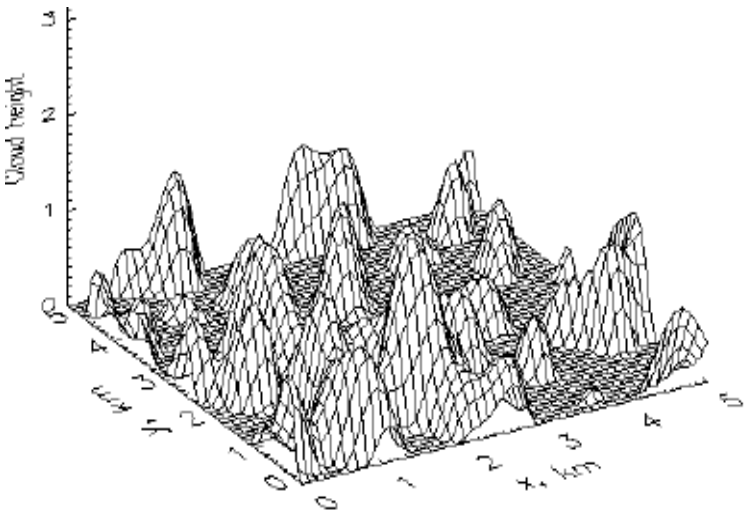

Figure 5.9 Fragment of the broken cloud field as model input. The model is based on the normal random (Gaussian) field with a fixed lower boundary [Geogdzhaev et al., 1997]. Cloud structure is described by 3D array of cells each with prescribed cloud properties. The dimensions of each cell should be sufficiently small compare to the photons free path. In most cases 50 to 100 meters cells were found to be sufficient in modeling OMI FOVs. The dimensions of the calculated field are similar to a single OMI FOV (10 km by 20 km). Cloud cover 0.5, aspect ratio 1, scattering coefficient 50 km^{-1}, and cloud average diameter 1 km.

Figure 5.10 Anisotropic factor $f_R(q_0,q,j)$ *of the broken cloud scene (Figure 5.9) for* $q_0=54^o$ *as a function of the satellite vertical angle,* q *(giving by distance from the center of the figure – nadir direction) and solar azimuthal angle,* j *(given by polar angle: forward reflecting in on the right and backward reflecting – on the left). The* f_g *is defined as the ratio of the equivalent Lambertian flux to the TOA reflected flux:* $f_g = pL(q_0,q,j)/M(q_0)$ *[Suttles et al. 1989].* f_g *<1 (shown by green color) means that the measured radiance is less than Lambertian and* f_g*>1 (red colors) means that the radiance for broken cloud scene is greater than Lambertian radiance.*

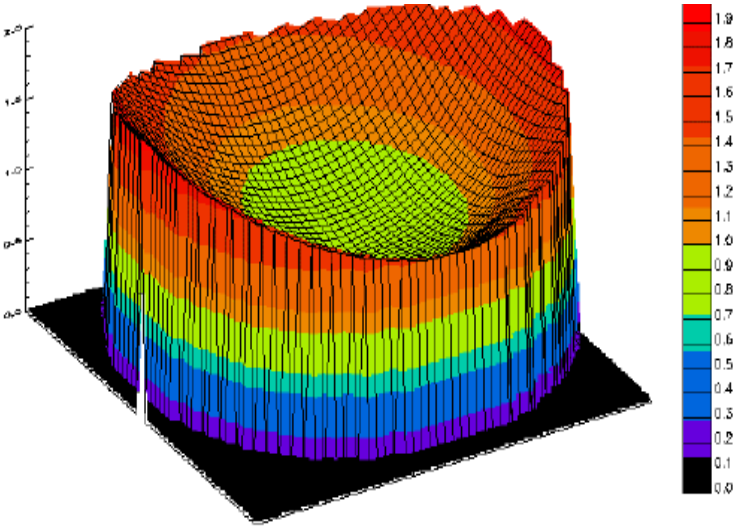

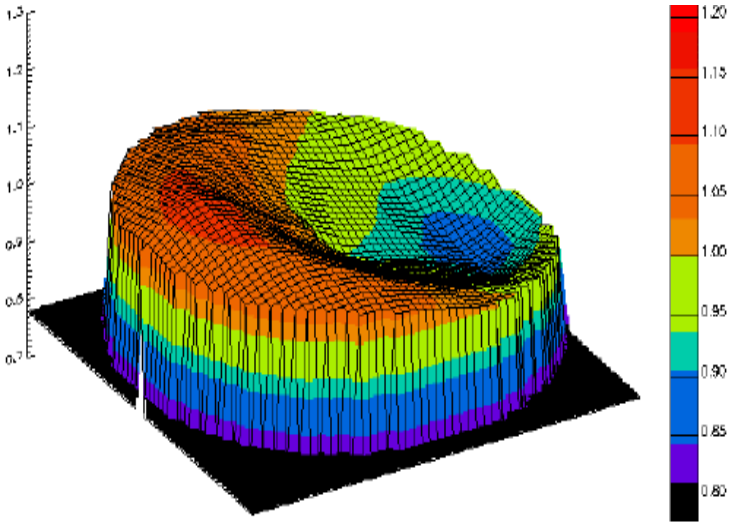

Figure 5.11 Example of a correction factor for broken cloud scene (Figure 5.9), which should be applied to the satellite UV data calculated with TOMS or OMI method (i.e. using homogeneous plane-parallel cloud model). Depending on the satellite viewing direction (explained in Figure 5.9) the correction factor ranges from 0.85 to 1.2. Cloud anisotropy is much less in the plane perpendicular to the solar principal plane than in the solar principal plane. Surface albedo 5%. Solar zenith angle 54^o. The equivalent optical thickness of the homogeneous cloud layer producing the same hemispherical albedo at the top of the atmosphere is close to 5.

1997]. Figure 5.9 shows one possible cloud model, which describes the fair weather cumulus cloud field. The model relates stochastic field characteristics with cloud amount, mean cloud diameter and aspect ratio. Based on these input parameters a representation of cloud field is calculated as convolution of two-dimensional Fourier series with random coefficients. Calculations of the radiance at the top of the atmosphere and irradiance at the surface are performed using 3-D Monte-Carlo (MC) code [*Geogdzhaev et al.*, 1997]. Figure 5.10 shows the simulated normalized angular distribution of the 360 nm radiance (Anisotropic function, f_g [*Suttles et al., 1988*]) backscattered from the cloud scene shown in Figure 5.9.

The "cloud shapes" error in estimated surface irradiance is proportional to the f_g ratio for broken (Figure 5.10) and homogeneous cloud scenes averaged over OMI FOV. The error is a function of assumed cloud parameters, OMI observational geometry, and surface albedo. Figure 5.11 shows the correction factor for cloud scene shown in Figure 5.9. The factor should be applied to the standard C_T value calculated using the optically equivalent (i.e. providing the same 360 nm radiance at the satellite) homogeneous cloud model. As expected, the factor is maximal in the solar principal plane. For this particular cloud scene and q_o=54^o the factor ranges from 0.85 (φ=0^o- forward reflection) to 1.2 (φ=180^o – backward reflection, i.e. "hot spot").

Because the equatorial overpass of EOS-Aura satellite occurs close to solar noontime (1:45PM ascending node), the OMI instrument scans in a direction, which is approximately perpendicular to the principal plane of the sun. Figure 5.11 shows that for these directions the correction factor is much less than in the solar principal plane. However, the errors may be still significant for specific observational conditions (we found that the error increases with solar zenith angle, i.e. at high latitudes and at high scan angles). We also found that "cloud shape" error does not depend on wavelength and data obtained at 360 nm can be extrapolated to the shorted UVB wavelengths. Based on this analysis we assume cloud shape error 5%.

Non-absorbing aerosols

For the purposes of estimating UV irradiance at the Earth's surface, there are two major classes of aerosols that must be considered: 1) aerosols that only scatter UV radiation and 2) aerosols that both scatter and absorb UV radiation. The first category is included in the measured scene reflectivity (cloud optical thickness), and attenuates UV radiation in a manner that approximates clouds of equivalent reflectivity (section 5.5.6). However, since these aerosols decrease the direct solar radiation but increase the diffuse radiation they have relatively small effect on the total surface UV irradiance [*Krotkov et al.*, 1998]. Moreover, satellite UV instruments can see the increase in the reflected radiation and correct for it. The OMI UV algorithm does not distinguish between water clouds, haze and non-absorbing aerosols. To estimate the resulted error we have modeled two most common types of non-absorbing aerosols (oceanic and sulfate) for low (τ_{550}=0.1), moderate (τ_{550}=0.2) and large (τ_{550}=0.4) aerosol loading (Figure 5-10). Typical attenuation by such aerosol ranges between 1% and 5% and increase reflectivity (LER) by about the same amount (upper left panel). For a nominal aerosol optical thickness of 0.2 at 550 nm, the typical error in estimating C_T by these various sources is ~+/-2% (figure 5.12, upper right panel). These aerosols tend to produce negative values of aerosol index (bottom left panel), in contrast to absorbing aerosols typically producing positive aerosol indices.

Table 5.3 summarized rms C_T errors for the mixtures of clouds and/or non-absorbing aerosols. These errors are probably representative of the conditions over most of the globe (oceans, rural land areas).

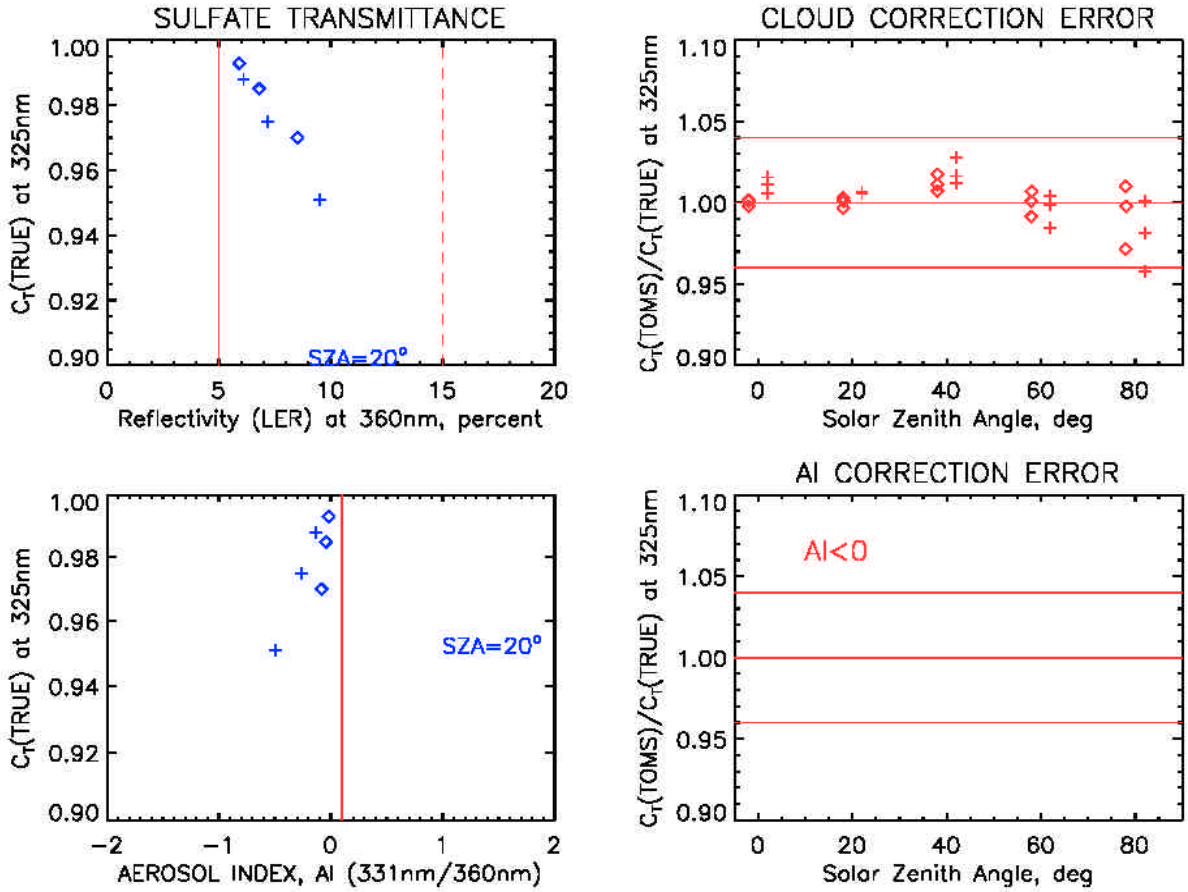

Figure 5.12 Upper left: C_T at 325nm as a function of R_{360}. Algorithm for non-absorbing tropospheric sulfate (diamonds) and oceanic (crosses) aerosol models. Aerosol extinction optical thickness at 550nm varies from 0.1 to 0.4, surface albedo 0.05 and solar zenith angle 20°. Upper right: cloud C_T error for the same aerosols and sza between 0 and 80°. Lower left: CT(325) vs AI; Lower right: AAC is not applied because AI<0

Table 5.3 Estimated errors in cloud C_T at for snow-free conditions and solar zenith angle less than 60^o The effects of cloud subpixel variability within OMI footprint are not considered.

Error source	**305nm**	**310nm**	**324nm**	**380nm**
Forward RT model [1)]	2%	1%	1%	1%
Cloud model [2)]	1%	1%	1%	1%
Cloud fraction [3)]	1%	1%	1%	1%
Cloud altitude [4)]	3%	2%	1.5%	0.5%
Trop. ozone (10 DU rms) [5)]	4%	2%	0%	0%
Strat. ozone [6)]	1%	0.5%	0%	0%
Non-absorbing aerosols [7)]	2%	2%	2%	2%
Cloud shape error [8)]	5%	5%	5%	5%
Total rms	8%	6.3%	6%	5.7%

1) *Estimated as differences between DISORT and Univ.Arizona codes for the same atmospheric model.*
2) *C_T change due to doubling modal radius of the modified gamma cloud drop size distribution.(~5mm for C1 cloud model [Deirmendjian 1969]) to ~10mm assumed by the International Satellite Climatology Project (ISCCP), [Rossow and Schiffer 1991;1999]);*
3) *Linearly mixing surface irradiances for different cloud fractions to calculate true CT and linearly mixing TOA reflectances to calculate estimated CT. (As= 0.05, tc=10 and 20, $q_o = 20^o$)*
4) *Moving cloud layer up and down (from 0.5 to 10km) assuming constant geometrical and optical thickness.20;*
5) *Assuming 10DU tropospheric ozone uncertainty in the presence of clouds (figure 5.5).*
6) *Assuming column ozone correction to CT (figure 5.5);*
7) *Inverting non-absorbing aerosols (sulfate, oceanic) using standard C1 cloud model (figure 5.12);*
8) *Modeled cloud shape error for fair weather cumulus cloud field at SZA=54^o (see figure 5.11)*

5.6.4. Error analysis for episodic events

This section provides error analysis for episodic events of absorbing aerosols (urban pollutions, biomass burning and desert dust).

Urban pollution

Aerosols that absorb the UV radiation attenuate both the direct and diffuse radiation, so the surface UV radiation is more strongly attenuated by such aerosols than by non-absorbing aerosols of the same optical depth (figure 5.13, upper left panel). The UV reduction can be as large as 20% under heavy pollutions (Mexico city, upper left panel).

Moreover, since these aerosols also attenuate the outgoing radiation, the OMI cloud C_T algorithm that treat these aerosols as non-absorbing clouds underestimates their optical depth, amplifying the error further, causing overestimation of UV irradiance. For example, the cloud C_T

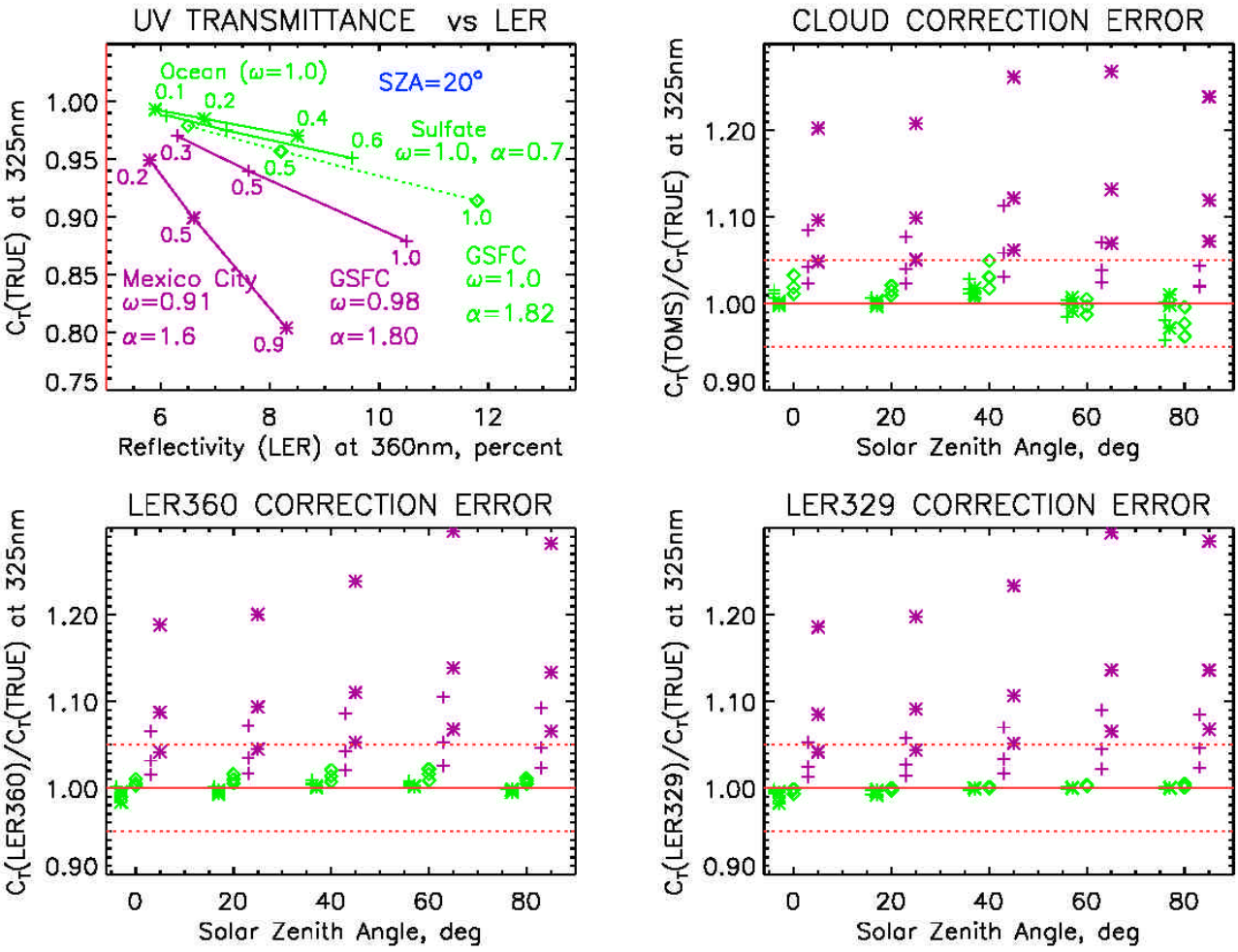

Figure 5.13 Relationship between C_T(325) and LER(360) for boundary layer aerosols. Non absorbing aerosols (Oceanic, sulfate, w=1) are shown in green color while absorbing aerosols (Goddard model, w=0.98 and Mexico city model, w=0.91, according to [Dubovik et al., 2002] are shown in purple color. In addition, the non-absorbing Goddard model is shown as green dashed line. For each aerosol model low, typical and high loading are shown that correspond to optical thickness at 550 nm 0.1, 0.2 and 0.4, respectively. The optical depth at 360nm is shown next to each line in upper left panel. Also the CIMEL measured climatological yearly average value of single scattering albedo at 440 nm (w) and angstrom parameter (a) is shown for each aerosol model. Bottom panels show simplified cloud correction CT~(1-LER(l)), at wavelengths l=360nm and l=329nm (see ozone algorithm, Vol 2).

algorithm will systematically overestimate UV irradiance by +5% at places like NASA/Goddard in Greenbelt, Maryland under typical summer aerosol loading and by +10% under heavy loading (Figure 5.13 upper right and bottom panels). The systematic overestimation could be larger in major industrial cities. For example, our simulations for industrial aerosol in Mexico city [*Dubovik et al.*, 2002] estimate UV overestimate by +10%-15% for typical aerosol loading and +25% for heavy aerosol loading. Because pollution aerosols are typically located in the boundary layer, they tend to produce negative aerosol index that makes it impossible to distinguish from non-absorbing aerosols (figure 5-9) and thin clouds using just OMI data itself. The positive C_T bias can be quantified using ground-based measurements of aerosol single scattering albedo and optical thickness.

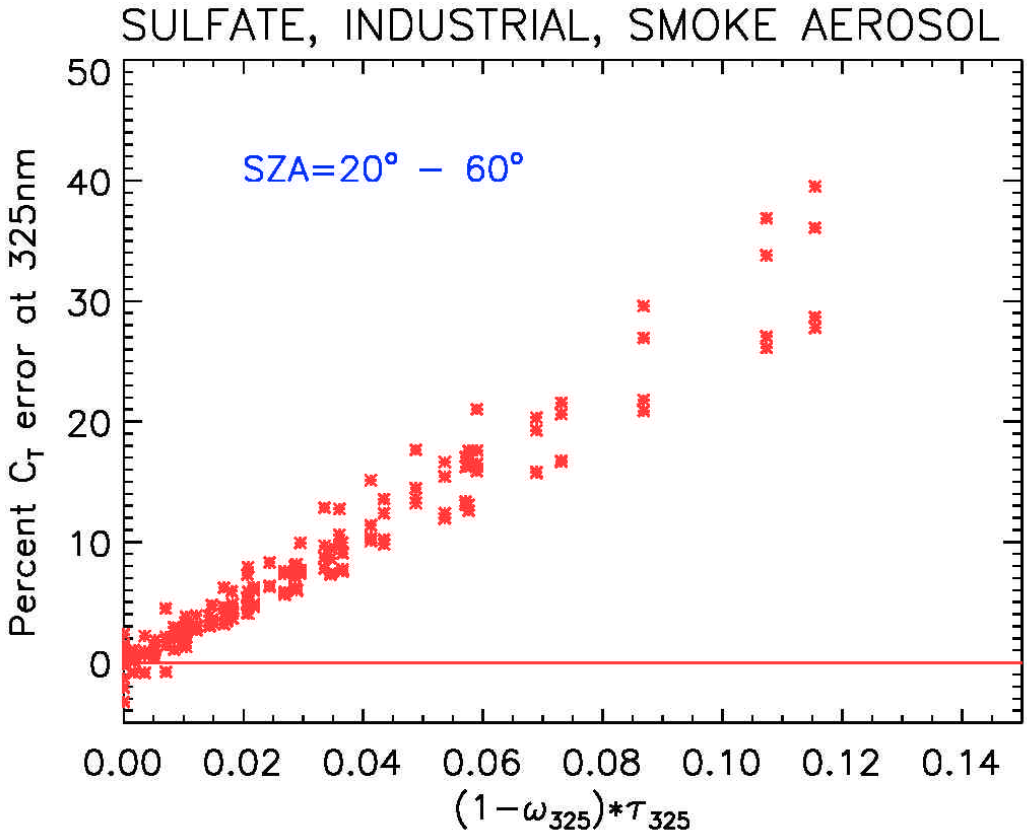

Figuire 5.14 Cloud C_T (325nm) correction error as function of aerosol absorption optical thickness at 325nm. Solar zenith angles 20-60^0, all aerosol models (except dust) and optical thickness at 550nm 0.1-0.4.

The cloud C_T overestimation is proportional to the aerosol absorption optical thickness, which is a product of extinction optical thickness, τ_A and single scattering co-albedo $\varpi=(1-\omega)$ (Figure 5.14). Therefore, correction to the OMI UV values can be applied for sites with established climatology of τ_A and ϖ at UV wavelengths. Although it is well known that soot produced by fossil fuel burning and urban transportation strongly absorb the UV radiation, properties of other potential UV absorbers, e.g., nitrated and aromatic aerosols [*Jacobson 1999*], are poorly known. To make matters worse, the distribution of UV-absorbing constituents of aerosols (iron-oxide, soot, nitrated inorganics etc.) is highly variable, both in space and time, even within a large urban area. Though satellite UV instruments can detect such aerosols when the conditions are right (absence of clouds, large elevated plumes), they typically miss them when the aerosols are located mostly in the planetary boundary layer.

Dust and Smoke in free troposphere

OMI 331 and 360nm radiance data can be used to correct for absorbing aerosols at a known altitude (AAC technique) by forming the aerosol index (AI) as discussed in Section 5.5.7. Because of the strong spectral dependence of refractive index in UV and typically high loading dust aerosol is expected to produce an unambiguous positive aerosol index allowing for its detection and tracking with UV technique (see section 4). In such cases the cloud C_T algorithm is not applied and AAC technique (equation [5-8]) is used instead, where conversion factor g is pre-calculated assuming nominal aerosol height, H_A=3km. Figure 5.15 shows estimated C_T errors for both cloud (and AAC techniques for dust and smoke aerosols [*Dubovik et al.*, 2002].

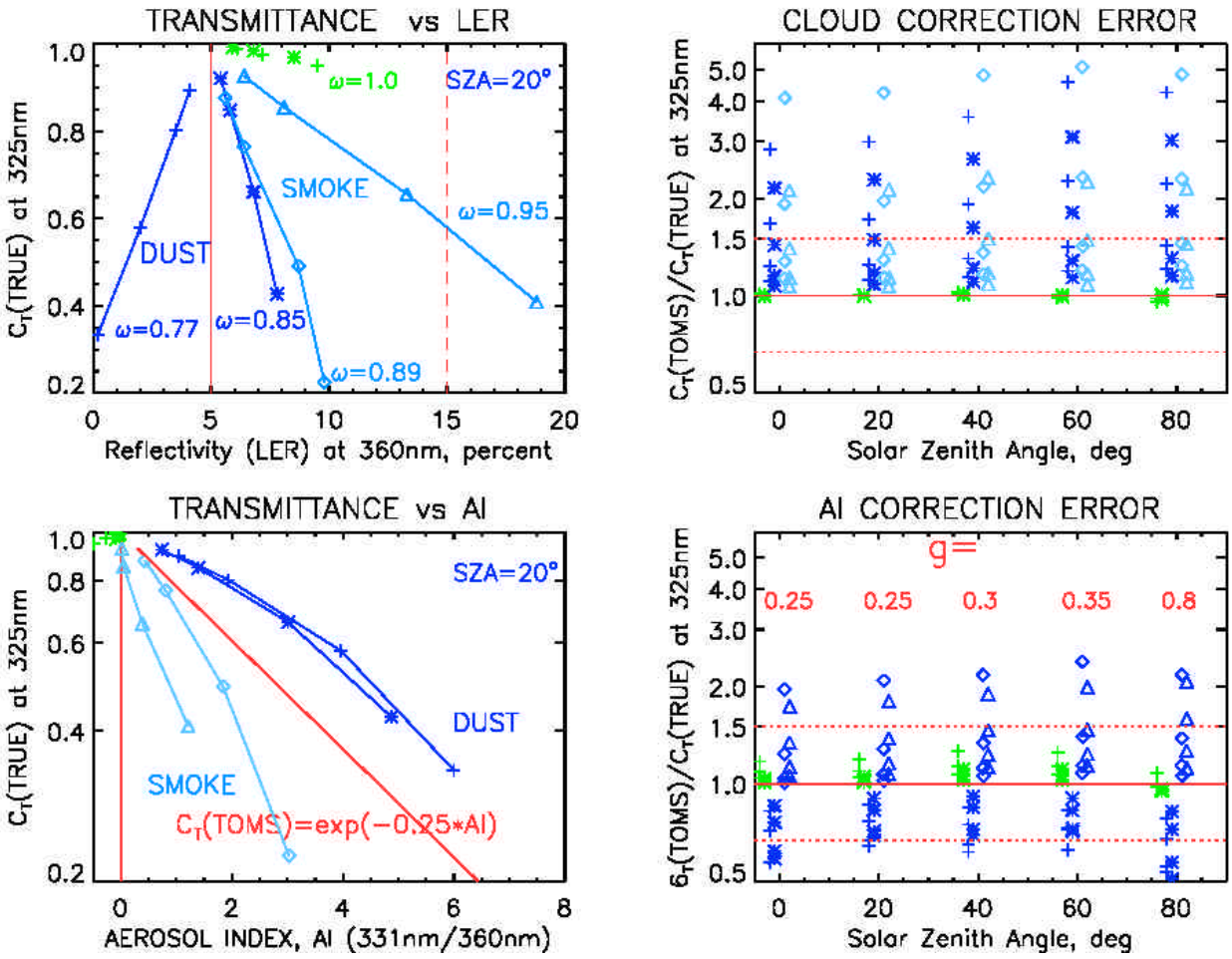

Figure 5.15 Errors in both C_T estimation tecniques: cloud (upper right) and AAC (bottom right) without aerosol type discrimination. Non-absorbing types (sulfate and oceanic) are shown in green color, dust aerosols are shown in dark blue color and smoke is shown in light blue color.Surface albedo As=0.05.

For dust aerosol the cloud technique fails (overestimation >100%), while the AAC technique provides reasonable C_T estimates within required uncertainty (~5%). The bottom left panel of Figure 5.15 shows a unique almost linear dependence of ln(C_T) on AI(331/360) for two different dust models (ω=0.77 and ω=0.85), which breaks only under heaviest dust loading (AI>4). At the same time, the 360nm reflectance could either increase or decrease with aerosol loading depending on dust absorption (upper left panel). Smoke typically produces larger reflectance and smaller AI values than dust (top and bottom left panels in figure 5-12) and C_T variability for different models is larger.

Figure 5.15 compares the errors of both cloud and AAC techniques without aerosol type discrimination (no a-priori aerosol information available). The cloud correction (default technique) is clearly a choice for non-absorbing aerosol types (sulfate and oceanic) and provides uncertainties within 2-3% at solar zenith angles less than 60°. The bottom right panel shows that non-absorbing aerosol types typically manifest themselves with a small negative aerosol index (AI > -1). On the other hand dust and smoke in free troposphere (H_A~3km) typically manifest themselves with a positive AI, so the AAC technique is applied instead of cloud technique. Without discrimination between dust and smoke aerosol types a compromise value of g=0.25 was recommended as a first order correction for tropical regions [*Krotkov et al., 1998*]. The errors of this simplified approach could be quite large in each specific case (20-50% either underestimation or overestimation). Therefore for AAC method to work within specified

uncertainty (~10%) one needs to discriminate not only between dust and smoke and also between different biomass burning regions and possibly seasons. The TOMS aerosol algorithm employs geographical approach for such discrimination, because the TOMS aerosol channels in the 330nm-380nm range are not sufficiently separated to allow enough spectral contrast between these two aerosol types [*Torres et al., 1998; Torres et al., 2002*]. For OMI (spectral range 330-500 nm) dust and smoke in the free atmosphere could possibly be separated (see Chapter 4) and C_T estimation could be improved in the future for these aerosol types.

The above error analysis assumed that the aerosol height is known accurately. This is not typically the case. The TOMS UV algorithm assumes the nominal aerosol height at 3km. *Herman et al.* [*1999*] has quantified the error due to unknown vertical profile of absorbing aerosol (Table 5.4). The sensitivity of UV transmission to the error in the assumed aerosol height E_F depends on the aerosol type (refractive index, particle size distribution, and single scattering albedo ω). We note that the error in surface UV irradiance is proportional to the error in satellite estimated aerosol height (*DH*). The error increases with increasing aerosol absorption (decrease in single scattering albedo, ω). Therefore, the largest error corresponds to the D3 model. The D3 model represents the large-particle dust, which is only infrequently encountered for long-range transport in the atmosphere (see [*Torres et al., 1998*] for a detailed description of the aerosol models D1, D2, D3, C1, and C2).

Table 5.4 Aerosol Parameters Used to Estimate Expected Errors E_F in UV-Irradiance Attenuation For the 5 types of absorbing aerosols considered in Torres et al. [1998]. $S = k/g = dt_A/dz$ is the altitude sensitivity of the inferred aerosol optical thickness (see Equation [5-8]) for a given value of AI at an assumed nominal altitude of approximately 3 km and altitude uncertainty 0.5km. The k values at 325 nm were previously estimated from a fit to the radiative transfer solutions (see Section 5.4.3): $k = 0.1 + 2(1-w) - 2(1-w)^2$ [Krotkov et al., 1998]. Substituting the values of k and S into Equation [5-8] one can estimate the errors in surface UV irradiance: Ef

Model/Parameter	w	**k**	**S (km^{-1})**	**E_F (%)**
Smoke C1	0.92	0.25	12	1.5
Smoke C2	0.84	0.37	40	7.5
Dust D1	0.90	0.28	12	1.7
Dust D2	0.72	0.50	43	11
Dust D3	0.63	0.57	55	16

The absorbing aerosol correction and error estimate in Table 5.4 were estimated specifically at 325 nm. The spectral transmittance of absorbing aerosols usually decreases at shorter UVB wavelengths (Figure 5.16). Therefore, the proposed spectrally independent AI correction will overcorrect UV irradiance at wavelengths longer than 325 nm and under correct at shorter UVB wavelengths. To account for the aerosol wavelength dependence one needs to know the specific aerosol model, including spectral dependence of aerosol optical thickness and single scattering albedo.

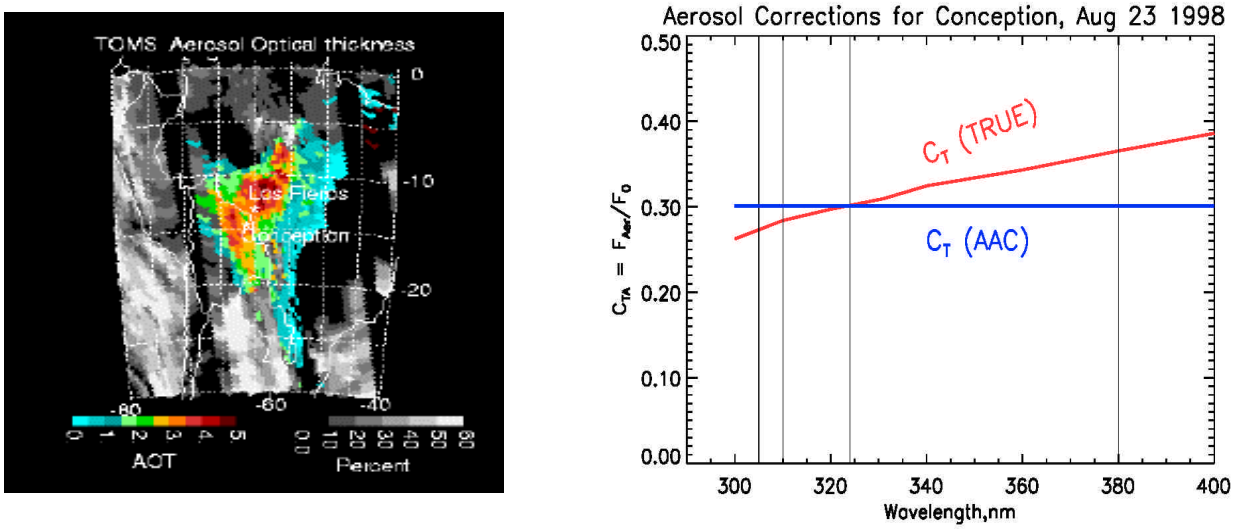

Figure 5.16 Estimated C_T spectral dependence (right panel) for a heavy biomass burning event in South America (Conception).TOMS smoke optical thickness and reflectivity is on the right figure. The C_T for smoke aerosol usually decreases at shorter UV wavelengths, while it increases for C1 cloud model (operational) and is constant for AAC method.

5.6.5. Error analysis for clouds over snow conditions

The presence of clouds and snow causes the most difficult conditions for the accurate estimation of UV irradiance. The main source of error in OMI estimates of surface UV irradiance, E, under such conditions is the daily variability of the regional snow albedo, A_S. We can estimate the error from the following equation [*Krotkov et al., 2001*]:

$$\frac{DE}{E} = \left(\frac{S_b}{1 - A_S S_b} + \frac{1}{1 - A_S} \right) DA_S \qquad [\,5\text{-}11\,]$$

where, $DA_S = A_S(assumed) - A_S(true)$, is the error in OMI snow albedo climatology. The first term accounts for error in E_{Clear} (Equation [5-2]) and the second one approximates the error in C_T [Krotkov et al 2001]. Figure 5.17 shows both the total error and separately errors in E_{Clear} and C_T as a function of A_S.

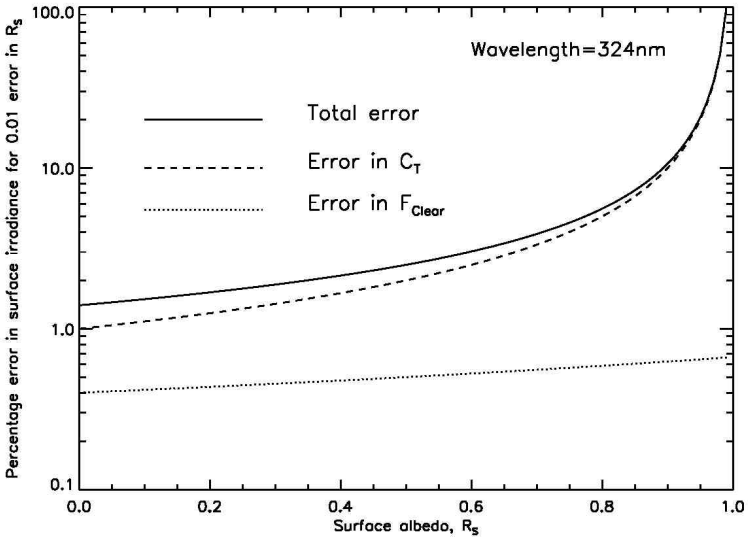

Figure 5.17 Percentage error in surface irradiance at 324 nm for 0.01 error in surface albedo, A_S, as a function of A_S. The error is a sum of the E_{Clear} error (dotted line) and C_T error (dashed line). We assume Lambertian reflection, so the error is not a function of solar angle. The error in surface irradiance is dominated by C_T error for all, but snow-free conditions.

We note that the total error is dominated by the C_T error, which increases by an order of magnitude with A_S increase from 0 to >0.9. We also note that errors in C_T and A_S are of the same sign: underestimation of A_S (fresh snowfall) causes underestimation of C_T and vice versa. Therefore, for regions at high latitudes with high surface albedo the OMI UV algorithm could possibly only estimate the weekly to monthly UV exposures with almost no correlation with ground observations on the daily basis.

5.6.6. Error summary

Table 5.5 summarized rms E errors for different scenarios. Although the errors are large for episodic events (urban pollution, dust and smoke plumes) and under snow conditions, these events are not expected to be frequent. Therefore, background error estimates are believed to be representative of the conditions over most of the globe (oceans, rural land areas). The table assumes horizontally homogeneous scenes over an OMI footprint (13 km × 24 km at nadir).

Table 5.5 Estimated errors in OMI surface spectral UV irradiance E including uncertainty in extraterrestrial solar irradiance. The effects of subpixel variability within OMI footprint are not considered.[1)]

Atmospheric scenario	**305nm**	**310nm**	**324nm**	**380nm**
Background, snow free	10%	8%	7%	6.5%
Seasonal snow (10% rms) [2)]	27%	26%	25%	25%
Permanent snow (3% rms) [3)]	30%	30%	30%	30%
Episodic events				
Smoke plume [6)]	22%	21%	21%	22%
Dust plume [5)]	15%	13%	11%	15%
Urban pollution [4)]	20% (30%)	15% (25%)	10% (20%)	10% (15%)

1) *Effects of sub-pixel inhomogeneity are considered in section 5.7*
2) *Assuming 10% uncertainty in snow albedo rms [Krotkov et al 2001] and 2.5 amplification factor for average snow albedo A=0.5 (figure 5-17);*
3) *Assuming 3% uncertainty in permanent snow albedo rms [Krotkov et al 2001] and 10 amplification factor for snow albedo A=0.9 (figure 5-17);*
4) *Mexico city aerosol scenario [Dubovik et al 2002] for typical aerosol loading; Numbers in parenthesis apply to extreme aerosol loadings (Figure 5.13);*
5) *AAC correction method applied assuming 5% dust model uncertainty, 10% for 0.5km height uncertainty (Table 5.4) and 10% spectral uncertainty at 305nm, 5% at 310nm and 10% at 380nm;*
6) *AAC correction method applied assuming 20% smoke model uncertainty, 5% for 0.5km height uncertainty (Table 5.4) and 5% spectral uncertainty at 305nm, 2% at 310nm and 6% at 380nm (Figure 5.16).*

5.7. Validation of UV algorithm and data product

Comparison of measured UV irradiance with estimates from satellite observation is potentially effective for the validation of the data from the two sources. The Total Ozone Mapping Spectrometer (TOMS) is an important source of UV data because it has provided both total ozone and cloud reflectivity measurements since the late 1970s. Since OMI UV algorithm is essentially the same as OMI UV algorithm, we can use long TOMS UV record to statistically validate the algorithm using long-term ground-based UV measurements available at many sites. However, validation of satellite-estimated UV irradiance is a complicated task because of the variety of possible sources of discrepancies with ground-based measurements. They range from errors in absolute instrument calibrations to a largely different spatial and temporal resolution for ground-based and satellite measurements [*Fioletov et al.*, 2002; *Chubarova et al.,* 2002].

We consider first validation results under clear sky conditions and compare with OMI estimated uncertainties for aerosol –free and cloud-free conditions (Table 5.2). Next, we consider validation of noon spectral irradiances for all-sky conditions and available comparisons of daily erythemal exposures. Finally we discuss briefly validation requirements for OMI UV product.

5.7.1. Validation of E_{Clear}

Systematic differences between UV irradiance measured at 10 Canadian Brewer sites and UV estimates from TOMS measurements have been analyzed by *Fioletov et al.* [2002]. The comparison between UV irradiance measured by the Brewer and derived from TOMS data at wavelengths with strong (305 nm) and weak (324 nm) ozone absorption was performed to determine possible ozone-related effects on the difference between the measured and TOMS-derived UV irradiance. Meteorological cloud amounts measured at or close to Brewer sites were also used to study effects of the cloud conditions on the difference. The aerosol effects were not considered.

Validation of E_{Clear} can be estimated by considering only the measurements when both TOMS and Brewer does not see any aerosols/clouds (Table 5-6). Such conditions correspond to the clearest possible days with TOMS reflectivity equal or less than the climatologically minimum Lambertian reflectivity (MLER).

Table 5.6 Summer (June-August for Churchill and May-August for all other) Mean TOMS-Brewer Difference in Noon Irradiation in % of TOMS UV irradiance. Tau=0, cloud amount=0 [Fioletov et al., 2002].

Station	Number of days	324 nm	305 nm	Erythemal
Churchill	9	6.5	8.2	5.8
Edmonton	19	5.3	7.2	5.2
Goose Bay	1			
Saskatoon	13	6.1	8.4	7.5
Regina	19	5.0	5.9	4.6
Winnipeg	11	6.3	7.7	6.6
Saturna	50	1.3	1.2	0.5
Montreal	2			
Halifax	14	5.6	9.0	7.1
Toronto	19	3.9	8.5	6.1
Average*		5.5	7.8	6.1
Standard Deviation*		0.9	1.0	1.0

About 4% to 6% bias for 324 nm wavelength can be seen under clear sky conditions at all stations except one. This bias is likely caused by aerosol absorption because ozone and SO_2

absorption is negligible at 324 nm and cloud effects have been excluded. When absorbing aerosols occur in the absence of cloud, the TOMS algorithm treats them as cloud, overestimate their transmittance at 324 nm, and overestimate it even more at 305 nm (see figure 5-13 and 5-14). The Saturna Island station measurements show much lower difference with the TOMS-derived UV. The relatively clean air with low aerosol and urban pollution loading at this island site on the West Coast of British Columbia is most probably the cause of relatively higher levels of UV irradiance there.

5.7.2. C_T validation

Figure 5.18 [*Fioletov et al.,* 2002] shows the histogram of different cloud transmittance values (C_T) at 324 nm for Brewer and TOMS values. The number of Brewer measurements is higher for almost every bin if $C_T<1$.

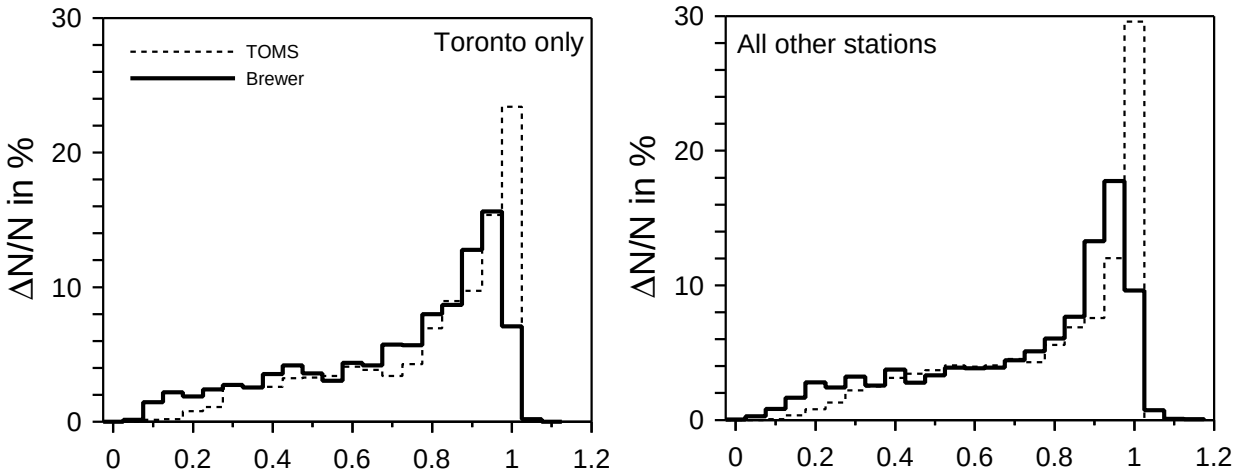

Figure 5.18 TOMS or Brewer C_T
[Fioletov et al 2002] Relative frequency of different C_T values in Brewer and TOMS observations estimated using Brewer measurements ±1 hour around noon and TOMS overpasses for Canadian stations. Relative numbers of TOMS observations for different TOMS C_T values and relative number of Brewer measurements for different Brewer C_T values are plotted using the same horizontal axes. Data are binned with 0.05 step by C_T. The histograms were produced using 2,200 pairs of Brewer measurements and TOMS overpass estimates for Toronto (top) and 11,941 pairs for 9 other Canadian stations (bottom).

TOMS estimates heavy clouds ($C_T<0.25$) less than half as frequently as the Brewer. Figure 5.18 (bottom) is based on data from 9 Canadian stations. Histograms for individual stations show similar distributions, as shown by the histogram for Toronto (Figure 5.18, top). Heavy clouds that cause very low C_T values at the ground do not cover the entire TOMS field of view and TOMS C_T is therefore higher. For rare cases when Brewer $C_T>1$ due to reflection from broken clouds, TOMS-derived UV is lower than the ground measurements.

5.7.3. Validation of spectral noon irradiance

The TOMS-Brewer difference expressed in percent of the TOMS-derived irradiance (or the Brewer to TOMS ratio) does not have a strong dependence on the TOMS C_T, which suggests examining the TOMS-Brewer bias in two classes of C_T or reflectivity values rather than analyzing it as a function of C_T [*Fioletov et al.*, 2002]. The whole dataset was therefore divided into two nearly equal subsets: clear sky or thin cloud conditions with the TOMS reflectivity less

than 0.2 and cloudy conditions with reflectivity greater than 0.2. The results are shown in Table 5.7 for noon UV irradiance at 305 and 324 nm and erythemally weighted UV.

Table 5.7 Summer (June-August for Churchill and May-August for all other) Mean TOMS-Brewer Difference in Noon irradiance in % of TOMS UV irradiation (June-August for Churchill and May-August for all other) [Fioletov et al., 2002].

Station	Number of days	324 nm	305 nm	Erythemal	Number of days	324 nm	305 nm	Eryth.
	Data with TOMS reflectivity <0.2				Data with TOMS reflectivity ≥0.2			
Churchill	190	9.2	12.1	9.3	250	2.0	4.7	1.3
Edmonton	345	9.7	11.8	9.6	299	4.8	7.1	4.3
Goose Bay	111	9.4	11.5	9.4	273	13.9	16.7	13.8
Saskatoon	306	10.5	13.6	11.9	246	7.1	10.7	8.5
Regina	310	9.5	10.6	9.2	214	5.8	8.3	5.8
Winnipeg	308	9.9	12.4	10.7	253	6.9	8.8	6.9
Saturna	384	1.9	1.8	0.9	379	-2.4	-3.0	-4.1
Montreal	251	8.5	8.1	6.1	244	5.4	7.1	4.0
Halifax	252	8.6	12.5	10.1	271	4.8	10.0	6.8
Toronto	502	10.1	14.5	12.2	460	11.2	17.1	14.0
Average*		9.5	11.9	9.8		6.9	10.1	7.3
Standard Deviation*		0.7	1.8	1.8		3.6	4.3	4.3

Summer time mean noon (11 am-1 pm) erythemal (CIE) spectrally weighted irradiance data for Canadian stations.
*The average and the standard deviations were calculated using all stations except Saturna.

For clear skies (TOMS reflectivity <0.2) the Brewer-TOMS bias at 324 nm is about 9.5% for the subset with for all stations except Saturna. The spread of the bias values in this subset for UV at 324 nm is very small, from 8.5% to 10.5%. This 2% spread can be easily attributed to the instrument calibration uncertainties or to the difference in angular response for individual Brewer instruments. No significant difference was found when Nimbus 7 and Earth probe TOMS data were examined separately

The bias is slightly (insignificantly) smaller for cloudy conditions (TOMS reflectivity >0.2) and the spread between the Brewer sites is higher than in clear sky conditions. The difference in the angular response between Brewers could be one of the factors responsible for higher spread because effects of angular response error are higher for diffuse radiation than for direct solar radiation at low zenith angles seen in summer at noon. Local cloud conditions such as, for example, the lake effect at Toronto could also contribute to the differences [Fioletov et al 2002].

It is unlikely that the negative bias at the Saturna Island station is caused by the Brewer instrument problems (e.g., calibration error, different angular response error) because three different Brewer instruments have been used at that site between 1990 and 2000 and they all show similar differences with TOMS. All annual mean TOMS-Brewer bias values for noon UV irradiance at 324 nm are between 5% and –1%. For comparison, the same numbers for Toronto are 14% and 8%. The relatively clean air with low aerosol and urban pollution loading at this island site on the West Coast of British Columbia is most probably the cause of relatively higher levels of UV irradiance there.

The bias is greater at 305 nm than at 324 nm indicating some wavelength dependence in the reduction of clear sky UV irradiance caused by pollution or aerosol absorption. The difference is the smallest at Saturna Island and the largest at Toronto and Halifax. The last two

sites are located in polluted urban areas. The difference between UV irradiance 305 and 324 nm can be explained by, for example, small (1-2 DU) amount of SO_2 in the lower troposphere that cannot be detected from TOMS. This explanation is viable because relatively high amounts of SO_2 were commonly seen at Toronto as well as at the Halifax site that is located 3 km from a power plant. In addition to SO_2 the absorbing aerosols have spectral dependence of their transmittance

It is possible that some of the low values of the measured UV irradiance at the ground are caused by clouds being present between the cloud amount measurements. However, in most cases the difference is likely due to very thin clouds, haze, aerosols, or gaseous pollution. Some of these factors affecting the UV can be detected from OMI, while others, such as boundary layer aerosols, cannot. The last could cause a bias when OMI derived UV is compared with the ground measurements (Figure 5.14). To account for this bias, simultaneous spectral measurements of aerosol optical thickness and single scattering albedo are needed at the same wavelength (i.e. 324 nm or 305 nm).

5.7.4. Validation of daily erythemal exposure

Estimating daily exposure from once a day OMI measurement provides additional uncertainty due to diurnal changes in cloud patterns. However, for some locations these "sampling" errors average out with time averaging. We consider therefore TOMS summer mean daily exposure estimates with ground-based time resolved measurements, allowing accurate calculation of daily doses.

Summer (May-August) mean values of daily erythemal irradiation measured by the Brewer instrument and estimated from TOMS for Toronto are shown in Figure 5.19. The measured summer values in different years are from 5% to 12% lower than TOMS-derived UV irradiation and the average bias is about 9%. The standard deviation of the difference between the two data sets is about 4%. Good agreement over a longer time interval is seen between TOMS-derived UV and UV irradiance estimated from ground-based total ozone and global solar radiation (pyranometer) measurements [*McArthur et al.*,1999; *Fioletov et al.*, 2001].

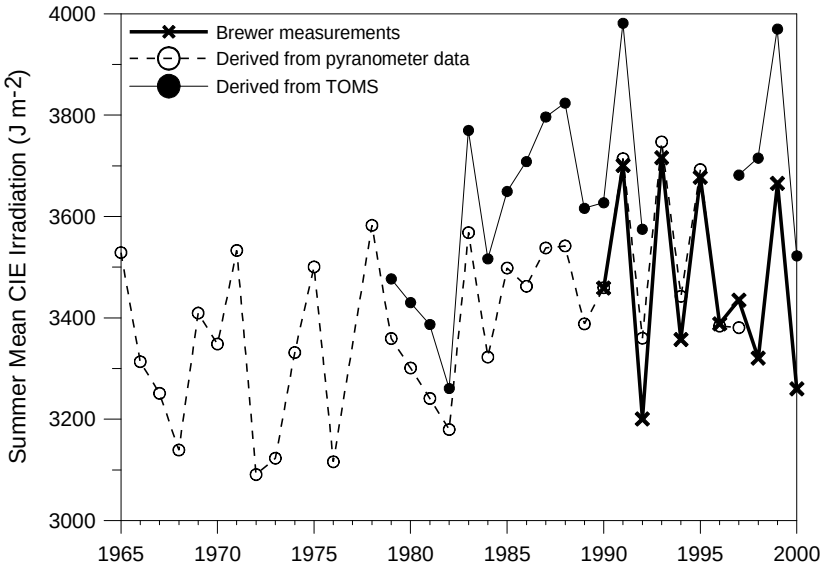

Figure 5-19. Summer (May-August) mean daily erythemal (CIE) irradiation at Toronto measured by the Brewer (corrected for angular response data), estimated from TOMS observations and derived from total ozone and pyranometer data [McArthur et al., 1999; Fioletov et al., 2001].

5.7.5. OMI UV validation requirements

Although, Figure 5.19 demonstrates that the satellite data successfully reproduces year-to-year fluctuation and long-term changes of UV irradiation, a separate study found that TOMS produces systematically higher UV irradiance values than are measured at the ground at northern midlatitude [*McKenzie et al.*, 2001]. Better agreement has been found at one site in the Southern Hemisphere. It was suggested that the UV absorption by tropospheric gases (ozone, SO_2, NO_2) or by absorbing aerosols has not been adequately taken into account in the satellite retrievals and the better agreement in the southern hemisphere is related to much lower level of pollutants there. To study geographical distribution of the bias, future OMI validation study should continue long-term comparisons at many locations around a globe with both polluted and clear atmospheres. The following UV validation requirements should be met:

1) Use long-term UV stations with high-level instrument QA/QC practices;
2) Ground station locations should be carefully investigated for potential sources of horizontal inhomogeneity on the OMI footprint scale (10 to 100km). The sources of inhomogeneity include relief (mountains) and/or changes in local climate (pollutants, clouds, lake);
3) UV measurements should be accompanied with spectrally resolved ground-based aerosol optical thickness and single scattering albedo measurements;
4) Spectral dependence of both aerosol optical thickness and single scattered albedo should be measured at UV and visible wavelengths.
5) To be able to use ground-based UV data for OMI UV product validation several measuring sites are needed within a satellite pixel. In this way the validation may be carried out in a physically reasonable way.
6) It is proposed that different validation areas will be established for the OMI UV validation. Typically 6 additional simple radiometers/validation areas would be needed. Following areas are proposed:

   A. SW Finland, 60 N
      - Existing spectral and broadband UV measuring programme since 1990
      - Advanced calibration facilities
      - Snow cover 2-5 months a year
      - Low aerosol content
      - High solar zenith angle conditions

   B. Greece 30-40 N
      - Existing spectral and broadband UV measuring programme since 1990
      - Advanced calibration facilities
      - High aerosol content, occasionally influence of Saharan dust
      - High tropospheric ozone content

   C. USA, site to be defined

5.8. Conclusions

The OMI surface UV irradiance algorithm will produce the downward spectral irradiance at the surface at 4 UV wavelengths: 305, 310, 324, and 380 nm, and the erythemally weighted irradiance. The algorithm is the same as that used for operational TOMS UV product: radiative transfer calculations, with input OMI ozone column, extraterrestrial solar flux from ATLAS-3/SUSIM, database on terrain elevation and albedo produce the spectral UV irradiance at the surface for a clear sky conditions. For aerosol- and cloud-free scenes and non-snow/ice surfaces the accuracy of the OMI surface UV irradiance data at 305 nm, 310 nm and erythemally weighted irradiance depends mainly on the accuracy of the ozone column. The total rms error is estimated ~3% at 310 nm and for the erythemally weighted irradiance at solar zenith angle (SZA) of 50^o (~6% at 305 nm) These errors do not include the uncertainty in the ATLAS-SUSIM solar extraterrestrial irradiance, which is currently the order of 3-5% in the middle UV spectral region. The error increases at larger SZA and at shorter UVB wavelengths

In real atmosphere under cloud-free and snow-free conditions the accuracy of the OMI UV data is limited mainly by an imperfect knowledge of the aerosol properties. The aerosols are highly variable in space and time so the external aerosol climatology is not available on a global basis. Using the scene reflectance at 331 and 360 nm, concurrent corrections for the presence of either non-absorbing aerosols/clouds or absorbing aerosols are applied. The choice between these two alternative techniques is based on the threshold values of the scene reflectance at 360 nm (see Equation [5.4]) and spectral contrast between 331 and 360 nm (Aerosol index, AI, see Equation [5.5]). The effect of absorbing aerosols on OMI UV estimates over large areas is expected to be small except in tropical regions where there are major dust plumes (e.g., the Saharan plume) and smoke plumes (e.g., southern Africa and South America) [*Herman et al.*, 1999]. At mid and high latitudes of Northern Hemisphere anthropogenic pollutions are expected to be the main sources of absorbing aerosols. If aerosol absorption is not detected in the OMI data the non-absorbing aerosol correction will still be applied, which will result in overestimation of the surface UV irradiance. Simultaneous measurements of aerosol optical properties and surface UV irradiance are required to quantify OMI clear-sky bias for polluted areas. When the aerosol effects are estimated using measured optical depths and reasonable single scattering albedo for urban areas (0.9 to 0.98), the clear-sky differences are usually reduced to within the instrumental error [*Krotkov et al.*, 1998]. This will be verified during OMI surface UV validation activities.

Since AI is not sensitive to UV absorbers in the boundary layer, the AAC technique cannot correct for such aerosols. This may be the reason why the TOMS seem to overestimate surface UV in industrial/urban regions (Figure 5.10). The C_T bias depends on the combined statistics of the aerosol optical thickness and single scattering albedo for a given site (Figure 5.11). The bias is always positive could be anywhere from 0% (for clean sites) to +10-15% (for polluted sites, Mexico City). Since there is very little understanding of the type and amount of UV absorbers that may be present in these areas, this problem currently remains unsolved.

Accurate knowledge of cloud transmittance, $C_{T,}$ is also critical for OMI surface UV estimates. Described method of cloud correction is expected to provide accurate (within 10%) estimate of the FOV average C_T for homogeneous cloud fields [*Krotkov et al.*, 2001]. Most of the errors are random and tend to average out in weekly to monthly mean values. It should be emphasized that the OMI-derived C_T value intrinsically represents an area average (over FOV) and not the irradiance over the local area observed by a ground-based instrument. The associated

effects are enhanced in case of spatially and/or temporally variable cloud fields but tend to average out on weekly (monthly) averages. Using ground UV measurements, *Martin et al.* [2000] have shown that, excluding all other errors, the uncertainty in daily doses reconstructed from a single near-noon satellite measurement is about 20% while it reduces to ~5% on monthly doses. Three-dimensional effects due to the non-homogeneity of clouds (cloud shapes and shadows) were shown to be less important due to the averaging over OMI FOV (13 by 24 km at nadir) and OMI observational geometry (scan perpendicular to the solar principal plane).

The uncertainty in snow albedo results in additional error in the OMI estimated surface UV irradiance. The UV error has the same sign as error in snow albedo and increases at high latitudes because of highly reflecting surfaces with permanent snow cover [*Krotkov et al.,* 2001]. The OMI surface UV algorithm has an improved snow correction procedure, using operational snow analyses from the ECMWF model. This will correct the present underestimation of surface UV irradiance by TOMS in winter conditions.

In addition to their complete spatial coverage of the earth's surface, satellite-derived surface UV maps gain value with the length of the covered time period. The OMI surface UV data will continue the TOMS surface UV data record (since 1978) with possible overlap with the EP/ TOMS instrument. This will enable to generate the homogeneous global UV dataset suitable for the future UV trend analysis.

Acknowledgements.

We thank the members of the TOMS team at Goddard Space Flight Center for producing the data sets upon which algorithm development was based. In addition, we wish to thank Tom Eck, Omar Torres, Christina Hsu, Alexander Vasilkov and Gordon Labow for useful discussions. The NASA TOMS program supported the algorithm development. We would like to thank Johan de Haan for thorough review of the manuscript.

5.9. References

Ahmad, Z. and Fraser, An iterative radiative transfer code for ocean-atmosphere systems, *J. Atm. Sci.*, 39, 656-665, 1982.

Anderson, D.E., and S.A. Lloyd, Polar twilight UV-Visible radiation field: perturbations due to multiple scattering, ozone depletion, stratospheric clouds, and surface albedo, *J. Geophys. Res.*, 95, 7429-7434, 1990

Arola A., S. Kalliskota, P.N. den Outer, K. Edvardsen, G. Hansen, T. Koskela, T. J. Martin, J. Matthijsen, R. Meerkoetter, P. Peeters, G. Seckmeyer, P. Simon, H. Slaper, P. Taalas and J. Verdebout, Assessment of four methods to estimate surface UV radiation using satellite data, by comparison with ground measurements from four stations in Europe, in press, *J. Geophys. Res.*, 2002a

Arola, A., J. Kaurola, L. Koskinen, A. Tanskanen, T. Tikkanen, P. Taalas, J. R. Herman, N. Krotkov, V. Fioletov, A new approach to estimate the albedo for snow-covered surface in space-borne UV retrieval method, to be submitted to *J. Geophys Res*, 2002b.

Bass, A.M., and R.J. Paur, The ultraviolet cross-sections of ozone, I, Measurements, in Atmospheric Ozone, in Ozone Symposium (1984:Halkidiki, Greece): Atmospheric Ozone, edited by C.Z. Zeferos, and A. Ghaz, p.606-616, D. Reidel, Hingham, Mass., 1985.

Bates, D.R., Rayleigh Scattering by Air, *Planet. Space Sci*., 32, 785-790, 1984

Brueckner, G.E., et al., The Solar Ultraviolet Spectral Irradiance Monitor (SUSIM) on board the Upper Atmospheric Research Sattelite (UARS), *J. Geophys. Res.,**98, 10695-10711*, 1993

Chubarova, N., A. Yu. Yurova, N.A. Krotkov, J. R. Herman, P. K. Bhartia, Comparisons between ground measurements of broadband UV irradiance (300-380nm) and TOMS UV estimates at Moscow for 1979-2000, in print, *Optical Engineering, SPIE*, 2002.

Cebula R.P., et al., Observations of the solar irradiance in the 200-350 nm interval during the ATLAS-1 mission: a comparison among three sets of measurements - SSBUV, SOLSPEC, and SUSIM, *Geophys. Res. Lett*., 23, 289-2292, 1996

Dave, J.V., Meaning of successive iteration of the auxiliary equation of radiative transfer, *Astrophys. J.*, 140, 1292-1,303, 1964

Dave, J.V., Effect of aerosols on the estimation of total ozone in an atmospheric column from the measurements of its ultraviolet radiance, *J. Atmos. Sci.*, 35, 899-911, 1978.

DeLand, M. T., and R.P. Cebula, NOAA-11 SBUV/2 solar spectral irradiance measurements 1989-1994: II. Results, Validation, and Comparisons, *J. Geophys. Res*, 1997

Deirmendjian, D., Electromagnetic scattering on spherical polydispersions, N.Y., American Elsevier Pub. Co., 290p., 1969

Dubovik O., B.Holben, T.F. Eck, A. Smirnov, Y. J. Kaufman, M. D. King, D. Tanre, I. Slutsker, Variability of absorption and optical properties of key aerosol types observed in worldwide locations, *J.Atm. Sci.*, 59, 590-608 2002.

Eck, T.F., P.K. Bhartia, and J.B. Kerr, Satellite Estimation of spectral UVB irradiance using TOMS derived ozone and reflectivity, *Geophys. Res. Lett*., 22, 611-614, 1995.

Erlick, C., J.E. Frederick, V.K. Saxena and B.N. Wenny, Atmospheric transmission in the ultraviolet and visible: aerosols in cloudy atmospheres, *J. Geophys. Res*., 103, 31541-31556, 1998

Fioletov, V. E., McArthur L. J. B., J. B. Kerr, and D. I. Wardle, Long-term variations of UV-B irradiance over Canada estimated from Brewer observations and derived from ozone and pyranometer measurements, *J. Geophys. Res., 106*, 23,009-23,027, 2001.

Fioletov, V., J.B. Kerr, D. I. Wardle, N.A.Krotkov, J. R. Herman, Comparisons of Brewer UV irradiance measurements with TOMS satellite retrievals, in print, Optical Engineering, SPIE, 2002

Frederick, J.E., and D. Lubin, The budget of biologically active ultraviolet radiation in the Earth-Atmosphere system, *J. Geophys. Res*.,93(D4), 3825-3832, 1988.

Geogdzhaev, I.V., T.V. Kondranin, A.N. Rublev, N.Ye. Chubarova , "UV Radiation Transfer Through Broken Cloud Fields Modeling and Comparison with Measurements", *Izvestiya, Atmospheric and Oceanic Physics*, 33, No 5, pp. 630-635, 1997

Herman, J.R., P.K. Bhartia, J. Ziemke, Z. Ahmad, and D. Larko, UV-B increases (1979-1992) from decreases on total ozone, *Geophys. Res. Lett*., 23, 2117-2120,1996.

Herman, J.R., P.K. Bhartia, O. Torres, C. Hsu, C. Seftor, E. Celarier, Global Distribution of UV-Absorbing Aerosols From Nimbus-7/TOMS Data, *J. Geophys. Res*., 102, 16,911-16,922, 1997.

Herman, J.R. and E.A. Celarier, Earth Surface Reflectivity Climatology at 340 nm to 380 nm from TOMS Data, *J. Geophys. Res*.102, 28003-28011, 1997.

Herman J.R., N. Krotkov, E. Celarier, D. Larko, and G. Labow, Distribution of UV radiation at the Earth's surface from TOMS-measured UV-backscattered radiances, *J. Geophys. Res.*, 104, 12059-12076, 1999

Herman, J.R., E. Celarier, and D. Larko, UV 380 nm reflectivity of the Earth's surface, clouds and aerosols, *J. Geophys. Res*., 106, 5335-5351, 2001.

Joiner, J., P.K. Bhartia, R.C. Cebula, E. Hilsenrath, R.D. McPeters, and H. Park, Rotational Raman scattering (Ring effect) in satellite backscatter ultraviolet measurements, *Appl. Optics*, 34,4513-4525, 1995.

Jacobson, M.Z., Isolating nitrated and aromatic aerosols and nitrated aromatic gases as sources of ultraviolet light absorption, *J.Geophys.Res.*, 104, 3527-3542, 1999.

Kalliskota S, J. Kaurola, P. Taalas, J. Herman, E. Celarier, and N. Krotkov: Comparison of daily UV doses estimated from Nimbus-7/TOMS measurements and ground-based spectroradiometric data, Journal of Geophysical Research, vol. 105, no D4, pages 5059-5067, 2000.

Kalliskota S: Some approaches to estimate UV radiation reaching the Earth's surface by using satellite data and their validation. Licentiate dissertation, Univ. of Helsinki, 2001.

Kerr, J.B., Observed dependencies of atmospheric UV radiation and trends, NATO ASI Series, Vol.I 52, Ed. By C.S. Zerefos and A.F. Bais, Springer-Verlag, Berlin, 1997.

Krotkov, N.A., P.K. Bhartia, J.R. Herman, V. Fioletov and J. Kerr, Satellite estimation of spectral surface UV irradiance in the presence of tropospheric aerosols 1: Cloud-free case, *J. Geophys. Res*., *103*, 8779-8793, 1998

Krotkov, N.A., P.K. Bhartia, J. Herman, Z. Ahmad, V. Fioletov, Satellite estimation of spectral surface UV irradiance 2: Effect of horizontally homogeneous clouds and snow, *J. Geophys. Res*., 106, 2001

Krotkov, N.A., J. Herman, P.K. Bhartia, C.Seftor, A.Arola, J.Kaurola, S.Kalliskota, Petteri Taalas, I. Geogdzhaev, Version 2 TOMS UV algorithm: problems and enhancements, in print, Optical Engineering, 2002

Leffell, D. J., and D.E. Brash, Sunlight and Skin Cancer, *Scientific American*,.52-59, 1996

Li, Z., P. Wang, and J. Cihlar, A simple and efficient method for retrieving surface UV radiation dose rate from satellite, *J. Geophys. Res.*, 105, 5027-5036, 2000.

Lubin D., P. Ricchiazzi, C. Gautier, and R.H. Whritner, A Method for Mapping Antarctic surface ultraviolet radiation using multispectral satellite imagery, *In: Ultraviolet Radiation in Antarctica: measurements and biological effects*, Weiler, C.S., and P.A. Penhale, Eds., AGU, *Antarctic Research series*, **62**, 53-82, 1994

Lubin, D. and E.H. Jensen, Effects of clouds and stratospheric ozone depletion on ultraviolet radiation trends, *Nature*, **377**, 710-713, 1995

Lubin, D., E.H. Jensen, and H.P. Gies, Global surface ultraviolet radiation climatology from TOMS and ERBE data, *J. Geophys. Res.*, 103, 26061-26091, 1998.

Madronich, S., Implications of recent total ozone measurements for biologically active ultraviolet radiation on reaching the Earth's surface, *Geophys.Res.Lett*., 19, 37-40,1992.

Madronich, S., The atmosphere and UV-B Radiation at ground level, In Environmental UV Photobiology, edited by A.R. Young et al., Plenum Press, New York, pp.1-39, 1993.

Martin, T.J., B.G. Gardiner and G. Seckmeyer, Uncertainties in satellite-derived estimates of surface UV doses , *J. Geophys. Res*., *105*, 27005-27011, 2000

Matthijsen, J., H. Slaper, H. A.G.M. Reinen, and G. J.M. Velders, Reduction of solar UV by clouds: A remote sensing approach compared with ground based measurements, *J. Geophys. Res*., *105*,5069-5080, 2000

Mayer B., C.A. Fischer, and S. Madronich, Estimation of surface actinic flux from satellite (TOMS) ozone and cloud reflectivity measurements, *Geophys. Res. Lett*., 25, 4321-4324, 1998

McArthur L. J. B., V. E. Fioletov, J. B. Kerr, C. T. McElroy, and D. I. Wardle, Derivation of UV-A irradiance from pyranometer measurements, *J. Geophys. Res., 104, 30,139-30,151*, 1999.

McKenzie, R.L., M. Kotkamp, and W. Ireland, Upwelling UV spectral irradiances and surface albedo measurements at Lauder, New Zealand, *Geophys. Res. Lett*., 23, 1757-1760, 1996.

McKenzie R., G. Seckmeyer, A. Bias, J. Kerr, and S. Madronich, Satellite-retrievals of erythemal UV dose compared with ground-based measurements at Northern and Southern mid-altitudes, *J. Geophys. Res., 106*, 24,051-24,062, 2001.

McPeters, R.D., P.K. Bhartia, A.J. Krueger, J.R. Herman, B.M. Schlesinger, C.G. Wellemeyer, C.J. Seftor, G. Jaross, S.L. Taylor, T. Swissler, O. Torres, G. Labow, W. Byerly, and R.P. Cebula, Total ozone Mapping Spectrometer (TOMS) Data Products User's Guide, NASA Ref.Publ. No 1384, 1996

Meerkoetter, R.B., Wissinger, and G. Seckmeyer, Surface UV from ERS-2/GOME and NOAA/AVHRR data: A case study, *Goephys. Res.Lett*., 24, 1939-1942, 1997.

Mora, de, S.J., S. Demers, and M. Vernet (Eds), The Effects of UV Radiation on Marine Ecosystems. *Cambridge Univ. Press*, 2000.

Peeters, P., J.F. Muller, P.C. Simon, E. Celarier, and J.R. Herman, Estimation of UV flux at the Earth's surface from GOME data, *ESA, Earth Observation*, 58, 39-40, 1998

Rossow, W.B. and R.A. Schiffer, ISCCP cloud data products, *Bull. Am. Met. Soc*. 72, 2-20, 1991.

Rossow, W.B. and R.A. Schiffer, Advances in understanding clouds from ISCCP, *Bull. Am. Met. Soc*. 80, 2261-2287, 1999.

Rottman, G.J., et al., Solar Stellar Irradiance Comparison Experiment 1: instrument design and operation, *J. Geophys. Res.*, **98**, 10667-10678, 1993

Rublev, A.N., A.N. Trotsenko, N.E. Chubarova, O.M. Isakova, I.V. Geogdzhaev, T.V. Kondranin, P.Yu. Romanov, The use of satellite data for determination of downward solar radiation fluxes at cloudy conditions and their comparison with ground-based measurements, *IRS'96: Current Problems in Atmospheric Radiation*, W. Smith and K. Stamnes (Eds), 488-491, 1997.

SCOPE, Scientific Commitee on Problems of the Environment, Effects of increased ultraviolet radiation on biological systems, SCOPE, 51 bd de Montmorency, 75016 Paris, France, 1992

SCOPE, Scientific Commitee on Problems of the Environment, Effects of increased ultraviolet radiation on global ecosystems, 51 bd de Montmorency, 75016 Paris, France, 1993

Smith, R.C., B.B. Prezelin, K.S. Baker, R.R. Biligare, N.P. Boucher, T. Coley, D. Karentz, S. MacIntyre, H.A. Matlic, D. Menzies, M. Ondrusek, Z. Wan, K.J. Waters, Ozone depletion: ultraviolet radiation and phytoplankton biology in Antarctic waters, *Science*, 255, 952-959, 1992.

Stamnes K., S.-C. Tsay, and K. Jayaweera, Numerically stable algorithm for discrete-ordinate-method radiative transfer in multiple scattering and emitting layered media, *Appl. Opt.*, ***27,*** 2502-2509, 1988

Suttles, J.T., R.N. Green, G.L. Smith, B.A. Wielicki, I.J. Walker, V.R. Taylor, and L.L. Stowe, Angular Radiation models for the Earth-atmosphere system. Vol. 1 Shortwave Radiation, NASA reference Publication RP-1184, 159pp, 1989

Torres, O., P.K. Bhartia, J.R. Herman, Z. Ahmad, Derivation of aerosol properties from satellite measurements of backscattered ultraviolet radiation. Theoretical basis, *J. Geophys. Res*, 103, 17099–17110, 1998.

Torres, O., P.K. Bhartia, J.R. Herman, A. Sinyuk, P. Ginoux, B. Holben, A long-term record of aerosol optical depth from TOMS observations and comparison to AERONET measurements", *J. Atm. Sci.*, 59, 398-413, 2002.

United Nations Environment Programme (UNEP). *Environmental Effects of Stratospheric Ozone Depletion - 1994 Assessment, edited by J.C.* van der Leun, A.H. Teramura, and M. Tevini, Nairobi, Kenya, 1995

Verdebout, J., A method to generate surface UV radiation maps over Europe using GOME, Meteosat, and ancillary geophysical data, *J. Geophys. Res.*,105, 5049-5058, 2000

Weiler, C.S., and P.A. Penhale, Eds. Ultraviolet Radiation in Antarctica: Measurements and biological Effects, AGU, Antarctic *Research series*, **62**, 257pp., 1994.

WMO98, Herman, J.R., R.L. McKenzie, S.B. Diaz, J.B. Kerr, S. Madronich, and G. Seckmeyer, Ultraviolet radiation at the Earth's surface, Chapter 9 In: Scientific Assessment of Ozone Depletion: 1998, *World Meteorological Organization, Global Ozone Research and Monitoring Project - Report N0.44*, Geneva, Switzerland, 1999

Woods, T.N. et al., Validation of the UARS solar ultraviolet irradiances: Comaparison with the ATLAS 1 and 2 measurementss, *J.Geophys. Res.*, 101, 9541-9569, 1996

6. Summary and Conclusions

P. Stammes
Royal Netherlands Meteorological Institute (KNMI), De Bilt, The Netherlands

In this chapter we will summarize the findings and conclusions from the OMI level 2 retrieval algorithms described in Chapters 2-5. In particular we will compare the expected errors on the OMI cloud, aerosol and surface UV irradiance products with the scientific requirements as mentioned in Chapter 1.

6.1. Clouds

An effective cloud fraction will be retrieved by comparing the measured reflectance in the continuum to the calculated reflectance of a cloud-free pixel and of a fully cloudy pixel with a Lambertian albedo of 0.8.

Two methods are proposed to retrieve cloud pressure: (1) use of the O_2-O_2 absorption band around 477 nm; (2) use of the filling-in of solar Fraunhofer lines in the range 355-400 nm due to rotational Raman scattering in the Earth's atmosphere. The latter method will also use the weaker O_2-O_2 lines at 360 and 380 nm.

In both methods the cloud is represented by a Lambertian surface (thick cloud approximation). In the Raman method results are also given for a transmitting scattering cloud (thin cloud approximation).

The O_2-O_2 method is based on spectral fitting of trace gas absorption lines (DOAS technique), which is relatively insensitive to noise. A look-up-table is used to interpret the slant column density of O_2-O_2 in terms of a Lambertian cloud pressure level. The retrieved Lambertian level is on average near the middle of the real cloud. It appears that the O_2-O_2 method is mainly sensitive to low clouds, due to the quadratic pressure dependence of the O_2-O_2 concentration. The random error (or precision) in the retrieved cloud pressure is < 50 hPa for a surface albedo of 0.05, cloud fraction > 0.2 and cloud pressure > 300 hPa. The random error increases for decreasing cloud fraction and decreasing cloud pressure. For increasing surface albedo the random error decreases (due to improved S/N), but the retrieved cloud pressure level tends to be more located towards the surface. The O_2-O_2 method yields the cloud pressure value together with its random error. The method has been applied successfully to global GOME data and compares well with results obtained by other algorithms (O_2 A-band and thermal-IR).

The Raman method will use iterative least-squares fitting of the filling-in of Fraunhofer lines in the range 355-400 nm. Filling-in due to Raman scattering in the ocean is included in the forward model, and can be included in the fitting procedure, with the ocean chlorophyll content as free parameter. The chlorophyll content will be an experimental product, but its inclusion mainly improves the cloud pressure retrieval over ocean. The Raman method appears to have a good sensitivity to low and high clouds. The Lambertian cloud pressure level appears to be in the middle to lower portion of the cloud. This is important to realize when validating the OMI cloud products with other cloud data. The method has been tested successfully on SBUV and GOME data, and compares well with results from O_2 A-band and thermal-IR methods.

The O_2-O_2 and Raman cloud techniques are largely complementary. The Raman method is expected to be more sensitive to high clouds, whereas the O_2-O_2 method is expected to be more sensitive to low clouds. The two methods taken together cover a large part of the spectral range of OMI, so that a possible wavelength dependence of cloud pressure is taken into account.

The O_2-O_2 and Raman cloud retrieval methods are both new and need extensive in-flight validation. Therefore, in the OMI validation phase both cloud algorithms will be applied and intercompared with correlative data from specific cloud sensors on e.g. CLOUDSAT, CALIPSO, and Aqua. After the validation phase a decision will be made about a possible combined cloud product, which uses the best performance of both algorithms for different scenes: high and low clouds, ocean and land, dark and bright surfaces, different solar zenith angles, etc.

6.2. Aerosols

The aerosol algorithm will produce for all pixels a UV aerosol index (342.5/388 nm reflectance pair) and a visible aerosol index (388/494.5 nm reflectance pair), as an indicator of the basic aerosol type (mineral dust, smoke, or sulfate).

For cloud-free pixels only the aerosol algorithm will yield the aerosol optical thickness and the aerosol single scattering albedo at multiple wavelengths. The algorithm consists of two methods, both using continuum reflectances: (1) the near-UV method, using reflectances at 342.5 and 388 nm, and (2) the multi-wavelength method, using reflectances at 17 wavelengths between 330 and 500 nm. The near-UV method works for all surface types, but the multi-wavelength method will mainly work over the ocean which is dark in the UV and the visible. As soon as good land surface albedo databases become available, the multi-wavelength method can also be used over land.

The retrieval accuracy of aerosol optical thickness and single-scattering albedo depends on the cloud mask, which identifies cloud-free pixels. In this respect, the OMI pixel size of 13 x 24 km and daily global coverage is an important advantage as compared to GOME for aerosol retrievals. The small pixel data of OMI may be helpful in identifying subpixel variability.

The total error budget of the aerosol optical thickness algorithm is estimated to be 30 %, excluding errors due to insufficient cloud masking, or due to particle non-sphericity effects (which is especially relevant for mineral dust aerosols). This theoretical error is probably a worst case estimate. The error in the single scattering albedo is estimated to be 0.05-0.1.

The near-UV method (applied to TOMS data) has been validated with AERONET ground-based measurements, and showed an error of 30 % in optical thickness. Because cloud contamination is expected to be less for OMI, the OMI accuracy is expected to be better.

6.3. Surface UV irradiance

The surface UV irradiance algorithm will produce the downward spectral irradiance at the surface at 4 UV wavelengths: 305, 310, 324, and 380 nm, and the erythemally weighted irradiance. The algorithm is basically the same as that used for TOMS: radiative transfer calculations, with as input the extraterrestrial solar irradiance spectrum, the measured ozone column and the surface albedo, produce the spectral UV irradiance at the surface for a clear sky. Using the scene reflectance at 331 and 360 nm, corrections for the presence of clouds and aerosols are applied. The algorithm has an improved snow correction procedure, using operational snow analyses from the ECMWF model. This will correct the present underestimation of surface UV irradiance in winter conditions.

For aerosol- and cloud-free scenes and non-snow/ice surfaces the accuracy of the surface UV irradiance at 310 nm and of the erythemally weighted irradiance depends mainly on the accuracy of the ozone column. The total rms error is 3 % for a solar zenith angle (SZA) of 50^o. This does not include the uncertainty in the used extraterrestrial solar spectrum, which is currently of the order of 3-5 % in the middle UV. The rms error increases for increasing SZA for shorter UV-B wavelengths.

Validation of the surface UV product with ground-based measurements is given much attention in Chapter 5. It appears that the current TOMS UV irradiance product systematically overestimates the UV irradiance as measured at the ground by about 9 %. This is thought to be due to absorbing aerosols and/or pollutants in the lower troposphere, which cannot accurately be detected from space. Therefore, collocated measurements of aerosols and pollutants in the troposphere are very important for validation of the OMI UV product.

It is proposed to have for OMI three validation sites (in Finland, Greece, and USA), with for each site several measuring stations within a satellite pixel of about 20 x 20 km^2, in order to measure the spatial variability of UV irradiance due to clouds, albedo, polluting gases, and aerosols. In this way a representative average can be determined. Other validation approaches include ground-based time series, and TOMS satellite data.

6.4. Conclusions

The estimated retrieval errors for clouds, aerosols, and surface UV irradiance are summarized in Table 6.1.

Table 6.1. Accuracy estimates for cloud, aerosol, and surface UV products from OMI, as follows from Chapters 2-5. OT: optical thickness at 400 nm. SSA: single scattering albedo.

Product	**Algorithm**	**Accuracy**	**Pixel size (km^2)**	**Remarks**
Cloud fraction	Continuum reflectance	0.03	13×24	Effective cloud fraction (thick cloud model)
Cloud pressure	O_2-O_2	< 50 hPa	13×24	Cloud fraction > 0.2 and cloud pressure > 300 hPa
	Raman	< 40 hPa	13×24	Cloud fraction > 0.1
Aerosol OT	Near-UV + Multi-wavelength	< 30 %	13×24	Cloud mask needed. Particle shape effects excluded.
Aerosol SSA	Near-UV + Multi-wavelength	0.05 - 0.1	13×24	Cloud mask needed
Aerosol index	UV + visible index		13×24	Used for absorbing aerosol detection in cloudy pixels
Surface UV irradiance	TOMS + improved snow correction	≈ 3 % (at 310 nm)	13×24	Random error for scenes without pollution, aerosols, clouds, and/or snow. Uncertainty in sun spectrum is excluded.

By comparing the above table to the scientific requirements in Table 1.1, we conclude that:

- The requirements for clouds are fulfilled. This means that cloud correction for the OMI trace gas products can be performed, at least for surfaces free of snow and ice.
- The requirements for the aerosol optical thickness and single scattering albedo are fulfilled, but only for clear sky pixels and excluding particle shape effects.
- The requirement for the surface UV irradiance is fulfilled regarding only the *random error* of the irradiance at 310 nm and the erythemal average, under clear sky, unpolluted and snowfree conditions and for solar zenith angles < 50^o. The current uncertainty in the solar spectrum (3-5%) is not included in the table value.

For the described algorithms several data sets are needed (auxiliary data). The following data sets are required for the algorithms to perform well:

- Spectral surface albedo database for the range 330-500 nm (for clouds, aerosols, and surface UV) at 10 x 10 km^2 spatial resolution
- Improved temperature-dependent O_2-O_2 cross-sections at 360, 380, and 477 nm (for clouds)
- Actual surface pressure field (for clouds and aerosols)
- High-resolution extraterrestrial solar spectrum in the UV (for UV irradiance)
- Actual snow/ice cover field (for clouds and surface UV).